LINEAR AND SPECTRALLY AGILE INTEGRATED MICROWAVE PHOTONIC DEVICES AND SUBSYSTEMS

A Dissertation
Presented to
The Academic Faculty

by

Christian G. Bottenfield

In Partial Fulfillment
of the Requirements for the Degree
Doctor of Philosophy in the
School of Electrical & Computer Engineering

Georgia Institute of Technology
December 2021

LINEAR AND SPECTRALLY AGILE INTEGRATED MICROWAVE PHOTONIC DEVICES AND SUBSYSTEMS

Approved by:

Dr. Stephen E. Ralph, Advisor
School of Electrical & Computer Engineering
Georgia Institute of Technology

Dr. Madhavan Swaminathan
School of Electrical & Computer Engineering
Georgia Institute of Technology

Dr. John D. Cressler
School of Electrical & Computer Engineering
Georgia Institute of Technology

Dr. Peter J. Delfyett
College of Optics & Photonics
University of Central Florida

Dr. Sorin Tibuleac
School of Electrical & Computer Engineering
Georgia Institute of Technology

Date Approved: September 1, 2021

ACKNOWLEDGMENTS

I thank my parents, my first teachers, who by their exemplary work ethic, cultivation of curiosity, and sacrifices deserve the highest praise, for as the great Michel Eyquem de Montaigne wrote some 500 years ago, “the greatest and most important difficulty of human science is the education of children.” All successes I have been so blessed with during my doctoral work are hence shared by my parents.

Then, there are those who endured the weight of this undertaking alongside me, namely my wife, Stephanie, and now three children Hazel, Landon, and Paul. Without the sacrifices of my wife to forego her own career and take on that greatest of sciences according to Montaigne, I would have abandoned this work long ago. Without belittling the difficulty of the Ph.D., her burden and sacrifice has been infinitely greater. I thank my two brothers, Brent and Adam, who throughout childhood and adulthood have shaped my imagination, resilience, and motivation necessary for success in this work.

I thank my advisor Dr. Stephen Ralph for his guidance, constructive criticisms, refreshing honesty, and an infectious motivation that has inspired me to do my best work.

Next, I would like to thank Dr. Sorin Tibuleac, Dr. John Cressler, Dr. Madhavan Swaminathan, and Dr. Peter Delfyett for serving generously on the defense committee.

I also thank all my colleagues that have provided endless help, ideas, and inspiration. These include Dr. Varghese A. Thomas, Dr. Jerrod Langston, Dr. Siddharth Varughese, Dr. Justin Lavrencik, Dr. Alirio Melgar Evangelista, Dr. HyungJoon Park, Dr. Andrew Stark, Dr. Ben Yang, Dr. Patrick Goley, Gareeyasee Saha, Daniel Lippiatt, Daniel

Garon, Alec Hammond, Michael Hoff, Stephen Hurst, George Tzintzarov, Milad Frounchi, and Glen Vinson.

Additionally, I thank all the industrial collaborators who supported this work throughout my Ph.D., including Richard DeSalvo from L3Harris, Rick Stevens from Lockheed Martin, the Georgia Tech Research Institute, AIM Photonics, and Globalfoundries.

Lastly, I thank all those innumerable individuals, who by sacrificing their lives to defend our country, by dedicating their lives to their craft, and by standing up for what is true and good have produced the opportunities that allowed me to work on the tiny, interesting corner of God's universe that I present here.

TABLE OF CONTENTS

LIST OF TABLES

LIST OF FIGURES

NOMENCLATURE

BW	Bandwidth (RF)	$SFDR$	Spur-Free Dynamic Range
CW	Continuous Wave	SOI	Silicon On Insulator
EDFA	Erbium-Doped Fiber Array	SWaP	Size, Weight, & Power
FCA	Free carrier absorption	TIA	Transimpedance Amplifier
IF	Intermediate Frequency	TPA	Two Photon Absorption
$IIP3$	3rd Order Intercept Point	V_π	Phase shifter half-wave voltage
IMD	Intermodulation Distortion Product	VOA	Variable optical attenuator
IMD2	2nd Order Intermodulation Distortion Product	β_{TPA}	Two photon coefficient
IMD3	3rd Order Intermodulation Distortion Product	$\Delta\alpha$	Change in absorption
IMDD	Intensity Modulated Direct Detect	Δn	Change in refractive index
IMWP	Integrated Microwave Photonics	$\chi^{(3)}$	3rd Order nonlinear susceptibility
LO	Local Oscillator	λ	Wavelength
MZI	Mach-Zehnder Interferometer		
MZM	Mach-Zehnder Modulator		
MWP	Microwave Photonics		
NF	Noise Figure		
N_{out}	Noise Power Spectral Density		
$OIP3$	Output-referred 3rd Order Intercept Point		
PD	Plasma-Dispersion		
PDK	Process Design Kit		
PIC	Photonic Integrated Circuit		
RF	Radio Frequency		

SUMMARY OF WORK

The goal of this research is to advance analog photonic communication systems through three major efforts: 1) to develop high performance microwave photonic filters, 2) to intrinsically linearize the integrated photonic component that contributes most to nonlinearities, i.e. the photonic modulator, and 3) to demonstrate microwave frequency tunable functions using integrated photonic platforms, e.g. frequency conversion. The first effort addresses a major need for microwave photonics, namely few-GHz or less optical filters. The second effort enhances the performance of current integrated modulators to achieve metrics suitable for demanding applications in defense, cellular fronthaul networks, and traditional telecom. The third effort provides necessary groundwork to enable the commercialization or implementation of next generation communication systems while advancing the understanding of such complex microwave photonic systems. The demonstration of microwave frequency tunable ("spectrally agile") architectures includes the design, simulation, characterization, and intuitive understanding of such systems.

Overall, this work addresses current and future needs in microwave photonics related industries by investigating both device-level and system-level solutions to achieve greater performance using integrated photonic technologies.

CHAPTER 1. THE MERGING OF TWO FIELDS

A pattern in the emergence of new fields is the merging of two previous areas of research; this is the mode by which the field of integrated microwave photonics developed. When the microwave photonics community recognized the utility of miniaturization offered by integration, integrated microwave photonics was born. Following is a summary of the parent fields and how they intersected to create integrated microwave photonics.

1.1 Integrated Photonics

Integrated photonics has successfully risen, in a manner often compared to analog ICs, from a mere research topic to a full-fledged commercial technology. *Integrated photonics* is the miniaturization of discrete optical components onto a chip, just as bulky electronic components were miniaturized by the first ICs; thus, integrated photonics is the fusion of discrete optics with integration, or integrated circuits (ICs). This integration yields the primary benefits of low size, weight and power (SWaP), low cost and high-volume manufacturing, better phase matching between optical paths, the ability to fabricate more complex optical systems on-chip, and the ability to shorten the physical distance between optical and electrical components for increased bandwidths. In the last decade, the rise of silicon photonic (SiP) foundries has contributed to a design, fabrication, and test ecosystem resembling the CMOS electronics environment. Foundries enable convenient and relatively affordable access to reliable SiP processes with mature process design kits (PDKs) for user-friendly photonic circuit design. Indium phosphide (InP) technologies also enjoy these benefits, though for lower volumes due to relatively small InP wafer sizes.

Integrated photonics, particularly silicon photonics, emerged in late 1980s and early 1990s from fundamental work on waveguiding structures and modulation methods. More broadly, integrated photonics began as early as the 1970s, through work with other optically interesting materials, including lithium niobate ($LiNbO_3$) and III-V materials. Motivation to merge electronics and photonics, however, led to the intense research of micro-optics in silicon-based material platforms, such as silicon-on-insulator (SOI) [1]. Other silicon-based material platforms include Si_3N_4, SiON, SiO_2, SiGe, and SiC. In fact, some of these materials have been successfully integrated many years later into modern silicon photonic foundry processes, particularly Si_3N_4 as a second optical layer and SiGe in the realization of monolithic BiCMOS circuitry [2-4].

Today, most discrete devices have been successfully integrated and offered by various foundry PDKs: high-speed modulators, photodetectors, optical phase tuners (e.g. thermo-optic heaters), combiners, splitters, spot-size converters, grating couplers, ring resonator filters, Bragg waveguide filters, multiplexers and demultiplexers, couplers between Si and SiN optical waveguides, polarization control elements, and arrayed-waveguide gratings. Devices that have eluded successful integration by silicon photonic foundries include on-chip lasers and circulators due to the silicon's indirect bandgap and weak magnetic properties, respectively. Currently, foundries are exploring workarounds to laser integration on silicon through heterogeneous attachment of lasers to interposers or to the die itself.

1.2 Microwave Photonics

Microwave photonics (MWP) is a field that uses photonics to augment the control, transmission, and processing of RF or microwave signals. Again, MWP is another example of the convergence of two fields: microwave engineering and optics. Microwave photonics encompasses methods and situations where both digital and analog signals need to be processed at some level. One of the primary benefits of photonics for RF transport is its efficiency, as the photonic loss through fiber is far lower than by the free-space transmission of RF/microwave signals suffering Friis path loss and atmospheric absorption. Photonics also offers large bandwidths, immunity to electromagnetic interference, good isolation between electrical signals, and a reduction in need for bulky RF cables [5]. Additionally, microwave photonic systems often leverage higher broadband linearity than purely analog electronic microwave systems.

The motivating roots of the field, particularly in communications, reach back to the era of the telegraph and grew quickly as modern electronic warfare techniques emerged from the technological innovations made during WWII. A specific motivation for RF engineers to consider optics was the need for a low-loss delay line. The development of practical lasers, wide (GHz) bandwidth modulators, fast detectors, and low loss optical fiber [6], which conceptually is an extension of previous metal RF waveguides, fit this need. RF engineers began merging RF and optical engineering to meet system requirements. Thus, microwave photonics was born as a formal discipline in the late 1980s and early 1990s [7].

Since its inception, the primary technological advantages offered by MWP are low-loss and wide bandwidth operation of opto-electronic systems. This has enabled MWP to

impact applications including fiber-based links for antenna remoting, radar, cellular, wireless, and satellite communications links. It has also expanded to radio-astronomy, cable TV delivery, signal processing, switched networks, beamforming, and defense-related applications [6,8,9].

1.3 Integrated Microwave Photonics

The merging of the decades-long integrated photonics and MWP fields has born a new, 21st century field called *integrated microwave photonics* (IMWP). It may be regarded as the intersection of microwave engineering, photonics, and integration technologies, as suggested in Figure 1. Integrated microwave photonics is the use of integrated photonic components to accomplish microwave photonic functions, such as modulation and detection, frequency translation or conversion, filtering, and other signal processing functions. The nascent field of IMWP has already demonstrated several functions important to RF engineering needs: frequency conversion [10,11], reconfigurable MWP processing [12], arbitrary waveform generation [13], high quality signal source generation [14-16], tunable true time delays [17], and optical beamforming [18,19]. These IMWP technologies make possible the dramatically expanded deployment of otherwise discrete (non-integrated) MWP systems. For example, IMWP can leverage size, weight, power (SWaP), and cost advantages over non-integrated technologies to benefit airborne and spaceborne platforms, as well as applications of scale such as for processing data from large phased arrays. With the integration of MWP functions also comes distinct challenges. Power limitations of on-chip waveguides and relatively lossy fiber-chip coupling make high power systems and hence high performance difficult to achieve. Furthermore, integrated photonic filters lag behind their discrete counterparts in performance.

Commercially fabricated integrated modulators do not yet achieve the efficiency, loss, and bandwidth metrics of discrete $LiNbO_3$ modulators. Nonetheless, the advantages presented by novel integrated architectures and devices, programmable analog chips, new applications and deployment opportunities, broad support from related technologies and applications, and high throughput fabrication capabilities make the pursuit of integration well worthwhile.

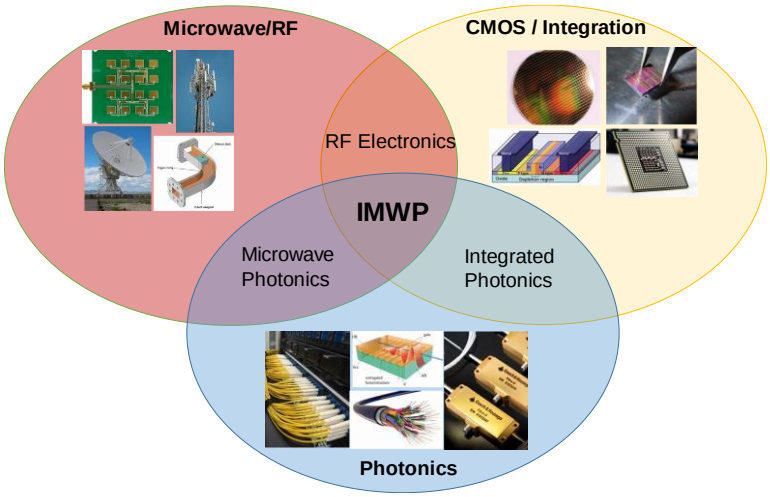

Figure 1 – Illustration showing the relationship and cross-over points between microwave engineering, photonics, and integration/electronics. Integrated microwave photonics lies at the center of these three regions.

CHAPTER 2. MICROWAVE PHOTONIC METRICS

There are several metrics common to RF/microwave electronics and photonics that are foreign to the digital world. These metrics tend to be agnostic to particular data formats and hence are useful for characterizing devices and systems for a broad range of applications. The primary metrics for characterizing a microwave photonic link include gain, noise, and dynamic range, each of which can be assessed in multiple ways. Following are the metrics and their definitions used throughout this work.

2.1 Gain

The first metric is the RF power gain, the ratio of the output RF (electrical) power to the input (electrical) power. In the case of frequency converters and other frequency-tunable systems, whereby the output is not at the same frequency as the input, the definition is altered, such that the ratio of the output intermediate frequency (IF) power is compared to the input RF power. Through this work the gain G is primarily evaluated in dB, but the linear form of the gain, denoted by lower case g, is employed as well. The gain is easily measured through a vector network analyzer as a function of frequency, or by using an electrical spectrum analyzer and swept signal generator.

2.2 Noise Metrics

The next metric is the noise, which is quantified in several useful forms. The first is the noise power spectral density, N_{out} measured commonly in dBm/Hz and colloquially called the “noise floor”. This noise floor is readily measured by most electrical spectrum analyzers and is measured close to the output signal frequency. The noise power spectral

density is necessary to quantify other metrics, such as the dynamic range. Other noise metrics include the noise factor (unitless) and its decibel form, the noise figure. The noise factor and noise figure both represent the relative noise added by a system to the input noise. An important point to highlight is that these metrics do not quantify the inherent increase or decrease of the output noise due strictly to the system gain. For example, a system with NF = 0 dB would exhibit the same output signal-to-noise ratio (SNR) as its input SNR. In a system with NF > 0 dB, the output SNR is smaller than the input SNR. Assuming a thermal noise limited input signal, the noise factor is a function of the output noise floor, system gain, and thermal noise, per the following relation [5] :

$$F = \frac{N_{out}}{g k_B T_s}, \qquad 2\text{-}1$$

where T_s is the standard noise temperature, and k_B is the Boltzmann constant. In decibel form, the noise figure at room temperature (300 K) is explicitly given as

$$NF = 174 + N_{out} - G. \qquad 2\text{-}2$$

Thus, these two expressions can be used to quantify a system's F and NF given careful measurement of the noise power spectral density and system power gain.

2.3 Dynamic Range and Linearity Metrics

Lastly, the dynamic range of a system describes the input and output signal levels over which the system remains perceivably linear. In other words, the dynamic range indicates the range of input signal powers usable before nonlinearities appear in the output. The most

common dynamic ranges references in RF systems are the compression dynamic range (CDR) and the spur-free dynamic range ($SFDR$). This work focuses on the latter metric but also references the nth order input and output intercept points, defined next.

This nth order output intercept point (OIP_n) is another useful metric, not only for calculating the spur-free dynamic range, but also to assess linearity itself. The output intercept point is the point (an output power) where extrapolations of the fundamental and a distortion product as functions of RF input power meet. Likewise, this intercept point can be referenced to the input power, rather than the output power, to yield what is called the nth-order input intercept point (IIP_n). This input intercept point is one of the best metrics of linearity for devices, such as modulators, because it is not a function of system noise or gain like the $SFDR$. The OIP_n is similarly independent of system noise but reflects the system gain. The third-order limited input and output intercept points are calculated:

$$OIP_3 = \left(\frac{P_\Omega^3}{P_3}\right)^{\left(\frac{1}{2}\right)} \tag{2-3}$$

$$IIP_3 = \frac{OIP_3}{g} \tag{2-4}$$

where P_Ω is the fundamental output (electrical) power, and P_3 is the power in the third-order distortion. The $SFDR$ is the range of input (or output powers) over which the intermodulation distortion products (the "spurs") remain below the noise floor. Typically, the intermodulation distortion products (IMDs) are dominated by either second-order or third-order effects. Hence, the $SFDR$ is usually specified as either the second-order limited $SFDR$ ($SFDR_2$) or third-order limited $SFDR$ ($SFDR_3$). Often the second order spurs remain

out-of-band of the RF spectrum of interest, and the IMD2 is typically generated near the second harmonics in sub-octave systems. Additionally, many RF photonic links bias the modulator near quadrature, which reduces second-order distortions originating from modulation. Hence, this work focuses on the $SFDR_3$ metric, as the IMD3s are generated within even very small RF bands and are generally unable to be filtered. Per the definition offered in [5], the nth order $SFDR$ is conveniently given in terms of the OIP_n, the nth order output intercept point:

$$SFDR_n = \left(\frac{OIP_n}{N_{out}B}\right)^{(n-1)/n} \tag{2-5}$$

Hence, the $SFDR_3$ is

$$SFDR_3 = \left(\frac{OIP_3}{N_{out}B}\right)^{2/3} = \frac{P_\Omega}{P_3^{\frac{1}{3}}}\left(\frac{1}{N_{out}B}\right)^{2/3} \tag{2-6}$$

The $SFDR_3$, OIP_3, and IIP_3 metrics are summarized graphically in Figure 2. Note that, because the slope of the P_Ω versus input RF power is unity, the $SFDR_3$ may be quantified experimentally by the range of input RF powers or the range of output RF powers with equal validity.

There is significant inconsistency in the literature regarding which linearity metrics are most meaningful for a given system or device. Generally, however, the definitions given here provide insight into where each metric is best cited. For example, because the $SFDR_n$ metric includes information about noise and bandwidth, it is best considered a *system* or *link* metric. Applying the $SFDR_n$ metric to devices is only useful in a comparative case, where different devices' impact on system linearity is measured by $SFDR_n$ using the same

link or surrounding hardware. The $SFDR_n$ metric can obscure a particular device's linearity by compensating through reduced noise or increased optical power. On the other hand, the OIP_n is relatively better for assessing device linearity, since it is not a function of system noise. Further, the IIP_n is likely the best candidate for assessing device linearity, since it is agnostic to both a system's gain and noise.

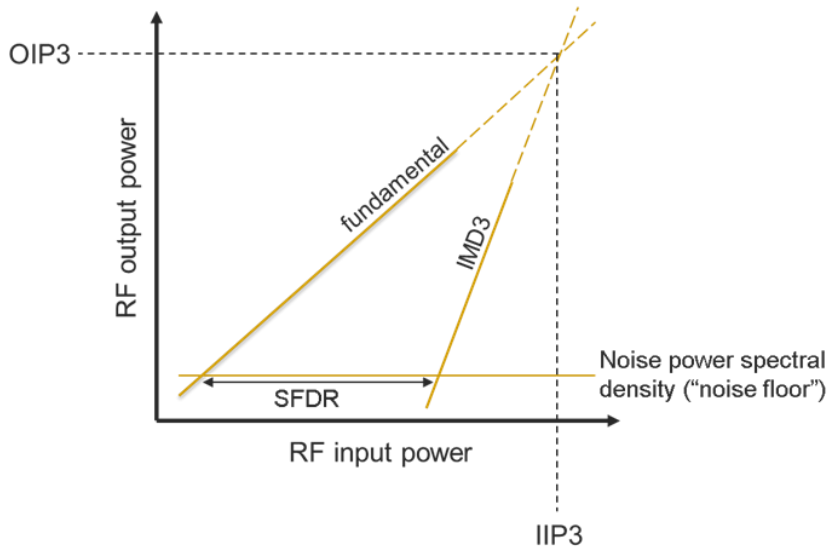

Figure 2 – Illustration summarizing the primary dynamic range and linearity metrics for a third-order limited system.

CHAPTER 3. RF PHOTONIC LINKS

While standard RF photonic links are not the focus of this work, discussing them is useful for several reasons: 1) demonstrating the application of the metrics in Chapter 2 to microwave photonic systems, 2) understanding many of the working principles for frequency converting systems of Chapters 7-9, and 3) motivating the need for improved power handling in Chapter 4 and linearization of Chapter 6. Frequency converting links share many similarities with these "fixed-frequency" RF photonic links, with a full comparison given in Chapter 7.

The RF photonic link discussed here is an intensity modulated, direct detect (IMDD) link employing a dual-drive (push-pull) MZM, Figure 3. The primary metrics of gain, noise figure, and $SFDR$ are presented as analytic functions of component metrics, with derivations found in [5].

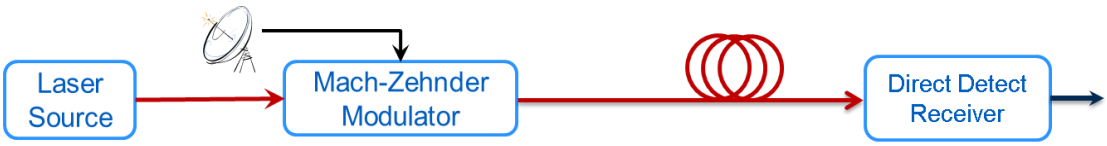

Figure 3 – Schematic of an intensity-modulated, direct detect RF photonic link.

3.1 Metric Expressions

For RF photonic links, the DC photocurrent I_{DC} is a key metric because it directly reflects the available optical power and link loss. As will be seen later, this is not the case for many frequency converting links, because null biased MZMs obfuscate a clear relationship between the I_{DC} and the optical power budget without further investigation of the

modulation extinction ratio. Hence, the frequency converters of Ch. 7 substitute available optical power and total link optical gain (or loss) for I_{DC}. On the other hand, RF photonic links usually employ quadrature bias, allowing a clear relationship between laser power, optical gain or loss, and generated DC photocurrent. In the equations of this section and Ch. 7, the variable I_{DC} is used for both single detection and balanced detection links. In the single detection case, the I_{DC} is simply the measurable photocurrent. In the balanced case, because balanced detection subtracts the photocurrents generated by the individual detectors and hence yields no measurable DC photocurrent, I_{DC} represents the *sum* of the individual detector photocurrents. This summed I_{DC}, though not reflective of the physical reality of balanced detection, is a convenient method for accounting for the improved gain and additional noise generated by the detector pair. For RF photonic links using quadrature bias, the photocurrent of a single detector is $I_{DC} = \frac{Rg_o l_{MZM} P_o}{2}$, where R is the photodiode responsivity; g_o is the net optical gain (or loss) between MZM and detector; l_{MZM} is the MZM insertion loss factor; and P_o is the optical launch power.

The gain of the link depicted in Fig. 3 is

$$g = \frac{I_{DC}^2}{V_\pi^2}\pi^2 R_i R_o \left|H_{pd}\right|^2 . \qquad 3\text{-}1$$

Here, V_π is the modulator half wave voltage; R_i is input impedance to the MZM; R_o is the photodetector output impedance; and H_{pd} is the photodetector filter response, which typically has a value of ½ due to a matching circuit on the photodetector output.

Concerning the noise metrics, N_{out} is

$$N_{out} = \frac{I_{DC}^2}{V_\pi^2}\pi^2 R_i R_o \left|H_{pd}\right|^2 k_B T_s + k_B T_s + 2qI_{DC}R_o\left|H_{pd}\right|^2 + RIN\, I_{DC}^2 R_o \left|H_{pd}\right|^2 \quad \text{3-2}$$

where k_B is Boltzmann's constant; T_s is the standard noise temperature; q is the fundamental charge; RIN is the relative intensity noise. The first term of the N_{out} expression is the input thermal noise translated to the link output by the gain. The second term is the output thermal noise, typically -174 dBm/Hz at room temperature. The third term is the shot noise, and the final term is the RIN, which may be composed of common-mode and non-common mode-components, the former which may be ignored in links using balanced detection. Using the definition of noise factor F in Ch. 2, the noise factor for the RF photonic link is

$$F = 1 + \frac{V_\pi^2}{\pi^2 R_i}\left(\frac{1}{I_{DC}^2 R_o\left|H_{pd}\right|^2} + \frac{2q}{I_{DC}k_B T_s} + \frac{RIN}{k_B T_s}\right). \quad \text{3-3}$$

Lastly the third-order spur-free dynamic range ($SFDR_3$) is

$$SFDR_3 = \left(\frac{4V_\pi^2}{\pi^2 R_i k_B T_s B}\right)^{\frac{2}{3}}\left(\frac{1}{F}\right)^{\frac{2}{3}} \quad \text{3-4}$$

where B is the bandwidth. While the $SFDR$ expression seems to show a strong dependence on the modulator V_π, note this V_π dependence only manifests when the link is input thermal noise limited, as determined upon substitution of the F expression. These metrics of gain, noise factor/figure, and $SFDR$ are calculated versus I_{DC} in Figure 4 for three RIN values:

-145 dBc/Hz, -155 dBc/Hz, and -165 dBc/Hz. These calculations assumed room temperature operation of an RF photonic link with V_π=4V, R_i =30 Ω (common for integrated transmitters), R_o=50 Ω, and H_{pd}=1/2. Figure 4(a) demonstrates that $g \propto P_0^2$ since $I_{DC} \propto P_0$; hence, maximizing optical power P_0 is key to maximizing the RF gain of the link. From Figure 4(b), the RIN limits the NF despite increasing I_{DC}; thus, increasing optical power can only benefit the NF until the RIN limited regime onsets. Reducing RIN enables lower NF.

Likewise, RIN sets the limit on maximum $SFDR$ per Figure 4(c). Lower RIN enables higher $SFDR$. Again, increasing optical power is vital to increasing the $SFDR$, but only until RIN sets the ceiling. Hence, minimizing RIN by using low noise optical sources and amplifiers or through balanced detection is a key method to improve microwave photonic system linearity.

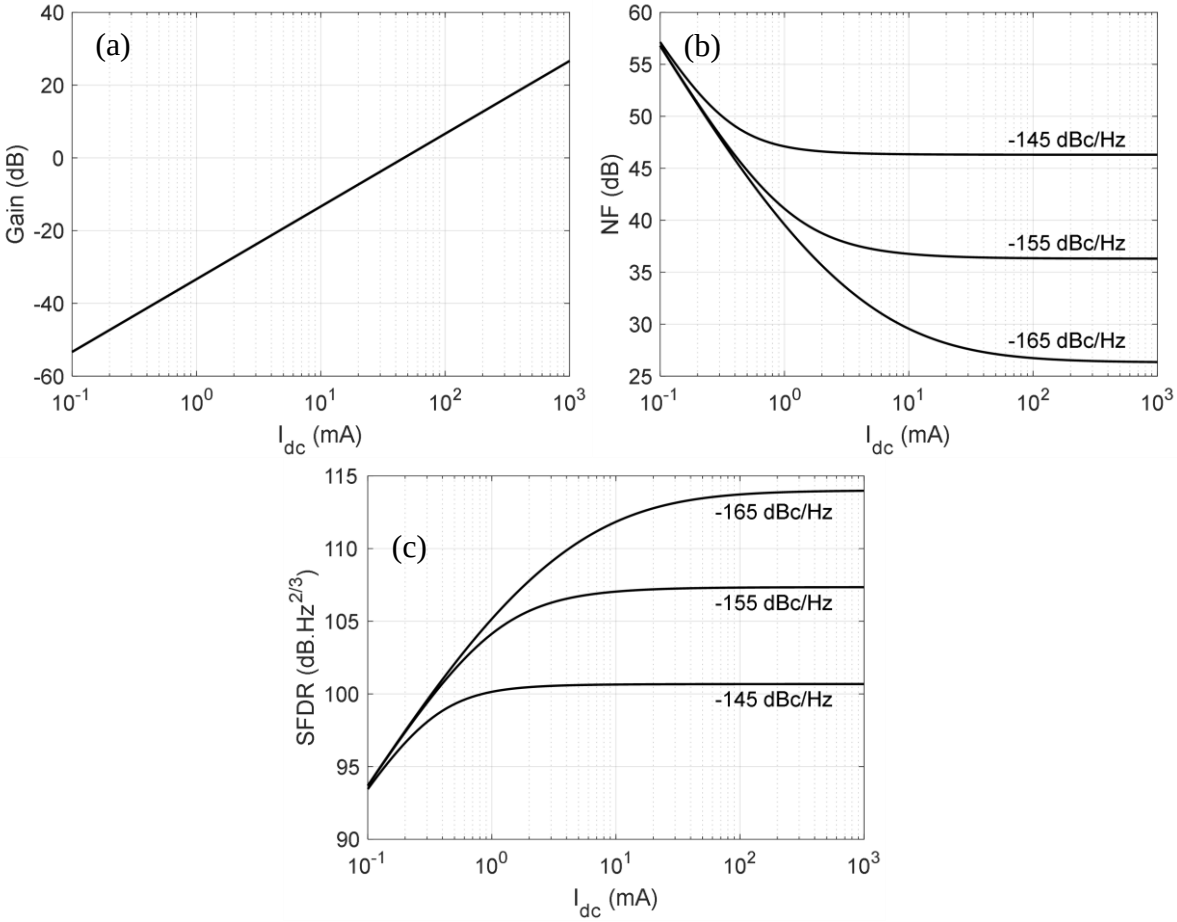

Figure 4 – Calculated externally modulated IMDD link metrics for various RIN values: (a) gain, (b) noise figure, (c) $SFDR$. All metrics increase with DC photocurrent and hence optical power. Upper limits on performance are due to RIN-dominated noise, at which point higher optical power does not improve noise figure and $SFDR$ metrics.

CHAPTER 4. SILICON PHOTONIC POWER HANDLING

As highlighted in the previous chapter, the primary microwave photonic metrics of interest all improve with increased optical power, barring certain conditions on the system's linearity and dominant noise source. Under linear conditions, the gain scales as the square of the optical power, and $SFDR$ and NF benefit from increasing optical power until the RIN limits further improvement. While discrete components can often handle optical powers up to and exceeding 1 W (+30 dBm), the optical power handling capacity of integrated photonics components remains largely unknown. Herein, the limits of optical power handling for one foundry's (AIM Photonics, using PDK v.1.5 [3]) silicon photonic waveguides, modulators, and photodetectors are investigated experimentally. Silicon and InP platforms are expected to exhibit lower power handling capacity than lithium niobate due to their lower two photonic absorption coefficients β_{TPA}, leading to increased two photon absorption (TPA) and subsequent free carrier absorption (FCA). Hence, ascertaining when the power handling of SiP components transitions from linear to nonlinear regimes is important for performance predictions of integrated MWP systems.

4.1 SiP Component Power Handling Measurements

The experimental setup consisted of a 1550 nm laser, an EDFA capable of outputting 1 W, a variable optical attenuator (VOA) to control the input power, and an optical power meter. The most reliable method of testing the input/output optical transfer function is by sweeping the attenuation of the VOA, rather than sweeping laser power or EDFA drive current since these do not act linearly under the test conditions. For example, increasing the laser output power will eventually lead to saturation of the EDFA, which will result in measurements indistinguishable from the onset of nonlinear absorption in the device under

test. Hence, the laser power and EDFA output power are fixed, while the attenuator linearly controls the power launched to the device under test.

First, the waveguide response (output vs. input optical power) of an edge-coupled loopback was measured and exhibits the onset of nonlinear absorption, Figure 5(a). The discrete derivative $\Delta P_{out}/\Delta P_{in}$ (right axis) most clearly indicates this onset of nonlinear absorption, as Figure 5(a) exhibits two distinct regimes: 1) the linear response with $\Delta P_{out}/\Delta P_{in} \approx 1$, and 2) the nonlinear response with $\Delta P_{out}/\Delta P_{in} < 1$. To approximate the optical power at which the nonlinear absorption onsets, the two regimes are linearly fitted and extrapolated until their intersection point, which indicates nonlinear absorption begins at 11.7±0.5 dBm.

The output power P_{out} is a function of both the loss induced by TPA and by FCA. Hence,

$$P_{out} = P_{in} e^{-(\alpha_{TPA}+\alpha_{FCA})L} \qquad 4\text{-}1$$

where P_{in} is the input optical power; α_{TPA} and α_{FCA} are the two photon and free carrier absorption (in Np/m); and L is the waveguide length. The calculation of both nonlinear loss and nonlinear refractive index responses are covered in detail in section 5.2, though the methods are incorporated here for calculating the expected power response of the waveguide.

Informed by Lumerical simulations of the foundry-specified waveguide geometry, silicon's β_{TPA} of 0.7 cm/GW, and estimated carrier lifetimes of ~30 ns, calculations model the measured responses well, indicating significant nonlinear absorption is due to free-carrier absorption [20-22]. Hence, the onset of TPA is particularly detrimental, as generation of carriers from TPA causes additional loss due to FCA.

Next, the optical power response of a SiP MZM fabricated in the AIM Photonics process was investigated for varied reverse bias on the MZM phase shifters, Figure 5(b). Presumably, the high dopant concentrations in SiP phase shifters may reduce the power handling of these devices as compared to undoped waveguides due to bandgap renormalization or enhanced free carrier absorption. Per Figure 5(b), nonlinear absorption onsets at 11.3±0.5 dBm on-chip optical power, slightly lower power than for the simple loopback (waveguide) structure, though well within its uncertainty bounds. Hence, the SiP MZM handles optical power nearly as well as undoped waveguides, though perhaps only due to moderate doping levels within the phase shifters. Because the MZM employs a 3 dB splitter at its input, the phase modulators receive 3 dB less optical power; hence, the phase modulator exhibit TPA and resultant FCA for optical power >+8.3 dBm.

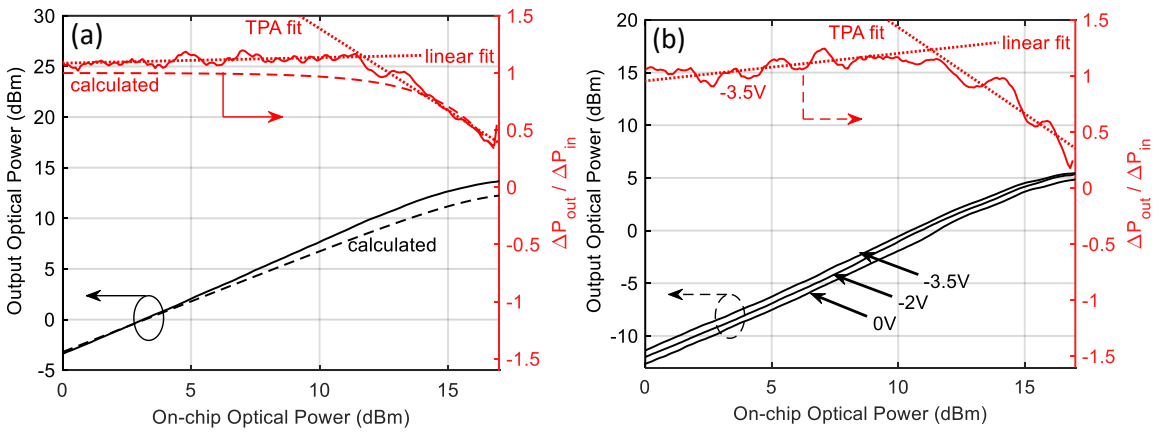

Figure 5 – (a) Waveguide optical power handling. Nonlinear absorption onsets at +11.7±0.2 dBm on-chip optical power at λ=1550 nm. (b) Modulator optical power handling. Nonlinear absorption onsets at 11.3±0.2 dBm on-chip optical power at λ=1550 nm. On-chip powers cite the estimated optical power immediately after the input edge coupler. Fitted lines (dotted) to linear absorption regions and nonlinear absorption regions are indicated, with their intersection defining an approximate onset of nonlinear absorption. Discrete derivatives $\Delta P_{out}/\Delta P_{in}$ are calculated for the right axis, and raw optical power responses are shown for the left axis. The calculated lines in (a) indicate responses due to TPA and TPA-induced FCA, yielding preliminary evidence that the power handling limitations are due to these processes.

Lastly, the optical power handling of the AIM Photonics photodiodes was evaluated for varied reverse biases, Figure 6. Rather than investigating optical nonlinearities in the photodetector, the most useful information is the combination of reverse bias and optical power that results in device failure. At 30 mW of optical power for -3V reverse bias, the photodiode was irreparably damaged. The current vs. optical power measurements exhibit supra-linear, nearly linear, and sub-linear responses for increasing reverse bias; these responses suggest system linearity may be affected by the photodetector input optical power and reverse bias conditions [23]. Further work should investigate the impact of reverse bias on link linearity, e.g. $SFDR$ vs. photodetector reverse bias. Though these photodetectors failed at only moderate optical power, higher power handling is possible through parallelization (arrays) [24].

This brief chapter has introduced the idea of optical power handling in SiP components and provided measurement-informed estimations on device power limitations. The next chapter expands on the nonlinear effects mentioned here and demonstrates how these perceived power limitations may be turned to an advantage for microwave photonic signal processing.

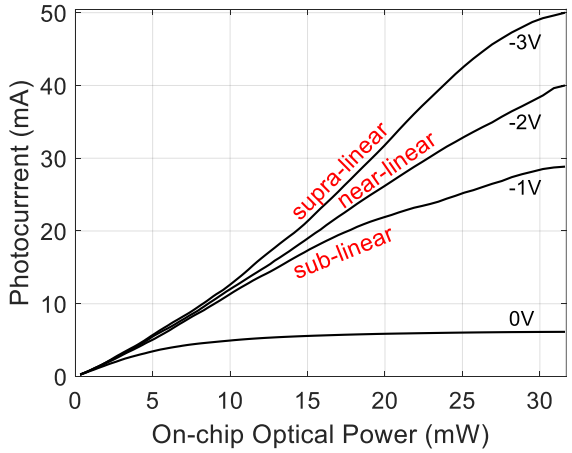

Figure 6 – Photodetector responsivity demonstrating a strong dependence on reverse bias; linearity and responsivity are both bias dependent. Note the device was damaged after testing at -3V for an on-chip power of 32 mW.

CHAPTER 5. SUB-GHZ OPTICAL FILTERS USING NONLINEAR RINGS

5.1 Narrowband Optical Filters

A major hurdle in IMWP is the achievement of narrowband filtering to accomplish sub-GHz RF filtering in the optical domain, particularly in a commercial silicon photonic process. Phased array antennas, RF photonic channelizers, and related technologies all require the ability to identify, select, and process data among a wide band of received signal. The most common integrated photonic filters include single and cascaded ring resonators and Bragg waveguides; yet these filters generally struggle to achieve the metrics required for many IMWP applications.

Here is presented an integrated optical filter based on single ring resonator and concentric ring resonator architectures coupled with TPA and free carrier effects to engineer filters with unprecedented performance in terms of both insertion loss and narrowband, fast roll-off responses.

5.2 Nonlinear Optical Effects

First, the nonlinear index and absorption effects are overviewed, culminating with a simple yet powerful model of nonlinear ring resonators in section 5.3 that will identify the nonlinear effects present in later experimental results.

The first nonlinear effect to consider is the (AC) Kerr effect, a result of silicon's relatively large $\chi^{(3)}$ parameter. The induced index perturbation Δn_{Kerr} is proportional to the optical intensity I by the Kerr coefficient $n_2 \sim 3\text{x}10^{-18}$ m^2/ W [25, 26],

$$\Delta n_{Kerr} = n_2 I \tag{5-1}$$

The Kerr effect also manifests as a small perturbation in the silicon's absorption response, by a proportionality constant r_{Kerr}, such that

$$\Delta \alpha_{Kerr} = n_2 r_{Kerr} I \tag{5-2}$$

Additionally, two photon absorption (TPA) induces further loss into the waveguide as a function of the optical intensity I by the TPA coefficient β_{TPA},

$$\Delta \alpha_{TPA} = \beta_{\text{TPA}} I \tag{5-3}$$

However, with TPA comes the generation of free carriers, in turn inducing further index and absorption perturbations via the plasma-dispersion effect. Hence, the free carrier induced index perturbation Δn_{FC} [25, 26] is

$$\Delta n_{FC} = -\frac{\mu_{lw}}{2k_p} \Delta \alpha_{FC}, \tag{5-4}$$

where u_{lw} is the linewidth enhancement factor with value ~7.5 at $\lambda = 1550$ nm; k_p is the propagation constant $k_p = 2\pi/\lambda$; and $\Delta \alpha_{FC}$ is the free carrier induced absorption perturbation, given by

$$\Delta\alpha_{FC} = \sigma N_c, \tag{5-5}$$

where σ is the carrier cross-section with value 1.45x10^{-21} m^2, and N_c is the carrier density given by

$$N_c = \frac{\tau_c \beta_{TPA} I^2}{2h\omega} \tag{5-6}$$

Here, τ_c is the carrier lifetime; h is Planck's constant; and ω is the optical frequency [25, 26]. The optical intensity I is related to the electric field by

$$I = \frac{1}{2}\sqrt{\frac{\epsilon}{\mu}}|E|^2 \tag{5-7}$$

This is useful because the calculation of the ring resonator responses at high optical powers will require quantification of the intra-ring intensity to account for nonlinear effects. Lastly, the thermo-optic effect is included, which manifests as an index perturbation Δn_{th} proportional to the change in temperature ΔT.

$$\Delta n_{th} = \frac{dn}{dT}\Delta T \tag{5-8}$$

Here, the thermo-optic coefficient $\frac{dn}{dT}$ for silicon near $\lambda = 1550$ nm is 1.84x10^{-4} K^{-1}. The approximate ΔT may be estimated [27] by

$$\Delta T = \frac{\tau_{th}\alpha I}{\rho C_t}, \tag{5-9}$$

where τ_{th} is a thermal dissipation time constant; ρ is the mass density of Si of 2.3x10^3 kg/m^3; and C_t is the specific heat capacity of Si, 705 J/(kg·K).

The total index [28, 29] is then:

$$n_{eff} = n_{eff,0} + \Delta n_{Kerr} + \Delta n_{FC} + \Delta n_{th} \quad 5\text{-}10$$

$$\alpha = \alpha_0 + \Delta\alpha_{Kerr} + \Delta\alpha_{TPA} + \Delta\alpha_{FC} \quad 5\text{-}11$$

The low intensity effective index $n_{eff,0}$ is calculated by a finite-difference element simulation of the fabricated waveguide geometry using Lumerical MODE. The baseline absorption α_0 is based on loss metrics given in the Globalfoundries PDK.

5.3 Nonlinear Ring Resonator Model

To include all the nonlinear effects, a simple model incorporating the nonlinear index and absorption effects was developed, following the methods of [31]. A pseudo-time domain method is used based on recursively calculating the electric fields inside the ring and output from the ring; the time dependence is normalized in terms of the number of circulations. This allows the user to understand both the steady-state response (after many iterations), or to observe the time evolution of the fields in the ring.

The input electric field to the ring is $E_1 = \sqrt{\frac{2P_{in}}{A_{eff}}}\left(\frac{\mu}{\epsilon}\right)^{\frac{1}{4}}$, where P_{in} is the input average optical power, and A_{eff} is the effective optical mode area. The input light is coupled to the ring with coupling coefficient κ, such that the initial electric field in the ring is $E_4 = \kappa e^{j\pi/2}E_1 + rE_3$. Here, r is the "reflection" or self-coupling coefficient, $r = \sqrt{1-\kappa^2}$. The field E_3 is

the propagated E_4 around the total ring circumference and hence is modified by phase ϕ and absorption α, such that $E_3 = e^{-j\phi}e^{-\alpha L}E_4$.

The phase ϕ and absorption α within the ring contain the nonlinearities described in the previous section; hence,

$$\phi = \frac{2\pi(n_{eff,0} + \Delta n_{Kerr} + \Delta n_{FC} + \Delta n_{th})L}{\lambda} \qquad 5\text{-}12$$

and $\alpha = \alpha_0 + \Delta\alpha_{Kerr} + \Delta\alpha_{TPA} + \Delta\alpha_{FC}$, as defined previously.

Finally, the output field E_2 is the sum of the throughput E_1 and coupled E_3 fields, $E_2 = rE_1 + \kappa e^{\frac{j\pi}{2}}E_3$. The power transmission response $T(\omega)$ is calculated via $T(\omega) = \frac{|E_2(\omega)|^2}{|E_1(\omega)|^2}$.

Figure 7 illustrates the locations of the referenced fields. The electric fields are calculated algorithmically using a MATLAB script, with the nonlinear index and absorption effects included from the previous section. This ring model is employed in the next section to compare to experiment and determine the primary nonlinear effects.

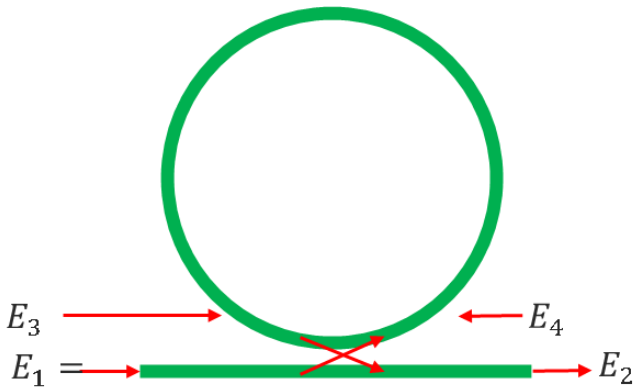

Figure 7 – Schematic illustrating locations of the calculated fields E_1, E_2, E_3, and E_4.

5.4 Nonlinear Ring Based Edge Filters

While optical bandpass filters have received the largest attention to date, numerous applications require only a spectrally sharp edge. For example, filtering out a sideband to produce single-sideband modulation or filtering out both carrier and a single sideband to isolate a carrier-less signal are two cases where only a sharp edge and high extinction are required. Furthermore, larger architectures of multiple edge filters can perform highly complex functions, such as channelization.

Previously, edge filters have been demonstrated using multimode subwavelength Bragg gratings, yielding a high-pass edge filter with 118 dB/nm roll-off and >40 dB extinction [30]. The same group later demonstrated another edge filter based on apodized sub-wavelength gratings, demonstrating 3.5 dB/nm roll-off, 40 dB extinction, and low insertion loss of 0.5 dB [31]. Another edge filter based on phase-shifted Bragg grating filters demonstrated 41.5 dB extinction over 18 GHz, corresponding to a roll-off of 2.3 dB/GHz or 288 dB/nm [32]. The roll-offs demonstrated shortly will be shown to exceed the previous literature by several orders of magnitude.

The edge filter presented in this section is based on nonlinear effects, particularly TPA and free-carrier (FC) effects described in the section 5.2. Although previous literature has demonstrated how nonlinear effects alter silicon-based ring responses and in particular cause highly asymmetric features at high optical powers [27, 29, 33, 34], no literature was found using such nonlinear rings for filtering, as is presented here in the context of filtering microwave photonic signals. Previous applications include using nonlinear effects in ring resonators for photon pair generation [27], all-optical modulation [35], and logic for all-

optical routing [36]. While traditional integrated filtering methods, such as by ring resonators or integrated Bragg gratings, must chase ever higher Qs through larger and lower loss structures to achieve high spectral resolution, the filtering method presented here does not require such stringent optical performance.

5.4.1 Single Ring Variant

A ring resonator with 20 μm radius using 500 nm wide strip waveguides and a 300 nm coupling gap was fabricated using the Globalfoundries 9WG (90 nm) silicon-on-insulator process. The single ring resonator was characterized by sweeping the laser wavelength and measuring the output response, Figure 8. For a launch power maintained at -9 dBm, the response of Figure 9(a) was obtained, showing very little asymmetry due to nonlinear effects. When the input optical power was increased to -3 dBm, the highly asymmetric response of Figure 9(b) was obtained. The calculated responses were obtained by varying the κ, τ_c, α_0, and τ_{th} parameters described in section 5.2. Though unknown, these parameters are well bounded. For example, the α_0 is assumed to remain within a factor of 2 of the PDK-provided absorption metrics of a standard waveguide, and the carrier lifetime τ_c is assumed to be on the same order of magnitude (~10^{-8} s) as those cited in relevant literature, using similar SiP processes [34]. The calculated responses, which include Kerr, thermal, TPA, and FC effects indicate that plasma-dispersion due to free carriers is the dominant nonlinearity. Further, the ring asymmetry is plainly due to plasma-dispersion effects from TPA-generated free carriers, since this is the only effect of section 5.2 with a negative index perturbation, which causes blue-shifting of the resonance. All other effects (Kerr and thermal) exhibit positive index perturbations that result in red-shifts in resonance.

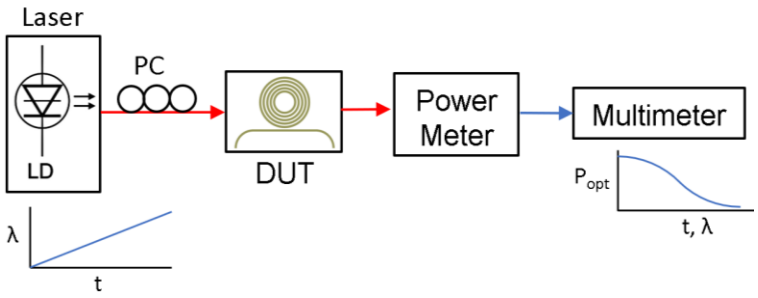

Figure 8 – Schematic of the experimental setup for characterizing the ring filters.

The sharp resonator asymmetry occurs as follows. As the input wavelength approaches the resonance, optical power begins to build in the resonator cavity. If this optical power is above the TPA threshold (~50 mW for SiP waveguides), TPA induced loss will occur, causing a generation of free carriers inside the ring waveguide. These free carriers then decrease the effective index via the plasma-dispersion effect, causing the resonance to blueshift. This begins a positive feedback loop whereby more optical power is coupled into the resonance, more TPA occurs to generate more free carriers, hence causing the index of refraction to further blue-shift until the resonant wavelength shifts lower than the input wavelength. At this point the positive feedback reaches its limit, and the process reaches steady state [36]. While a blue-shifted asymmetry leading to a sharp low-pass edge filter is here demonstrated, a red-shifted asymmetry leading to a sharp high-pass edge filter is also conceivable by engineering a ring with either dominant Kerr or thermal nonlinearities. In fact, in several transmission responses found in the literature, the high-pass edge filter is achieved, through presumably thermal effects [27, 34].

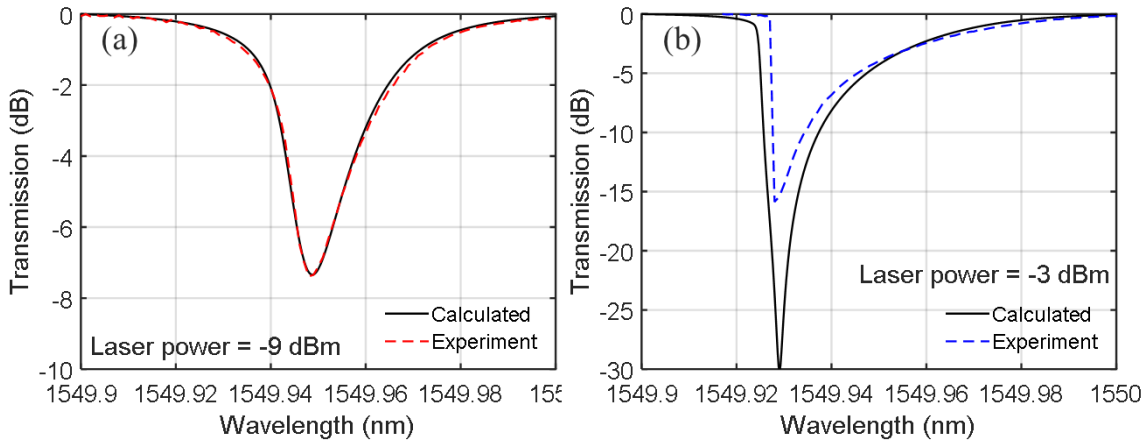

Figure 9 – Measured ring resonator transmission responses at (a) -9 dBm and (b) -3 dBm laser launch powers. At low powers, the ring response exhibits slight asymmetry due to nonlinear phase and absorption in the ring cavity. At higher powers, the response exhibits dramatic asymmetries due to strong nonlinear effects. This highly asymmetric response is useful as an edge filter, exhibiting 15.7 dB optical extinction over <0.001 nm, or <126 MHz. The edge exhibits an optical 3 dB bandwidth of <24.3 MHz. Finer laser step sizes likely reveal a spectrally finer edge, as later results indicate.

Figure 9(b) indicates the FC plasma-dispersion effect leads to an extraordinary edge filter response, exhibiting 15.7 dB optical extinction over <0.001 nm, or <126 MHz. This translates to a roll-off rate of 15,700 dB/nm or 124.6 dB/GHz. Later measurements using a finer laser step will characterize optical filters with even faster, record-setting roll-offs of over 10^3 dB/GHz. The optical 3 dB bandwidth is < 24.3 MHz, and the resolution of the laser step (0.001 nm here) limits further reduction of this estimate. The filter also exhibits very little loss, only 0.2 dB. However, the edge filter exhibits an optical extinction > 5 dB over a band of only 2.3 GHz. Hence, it is considered an edge filter over a narrow band.

Another resonance was measured at a slightly higher power, demonstrating no measurable insertion loss, Figure 10. As the input optical power increases, the nonlinearities onset faster as the input wavelength approaches the resonance, such that even a small fraction of coupled power will build up enough power in the ring to onset TPA. Hence, the insertion

loss effectively decreases for higher input optical power until there is virtually no insertion loss as in the case of Figure 10. This filter response demonstrates 24.0 dB maximum extinction and a roll-off rate > $155x10^3$ dB/nm or 1230 dB/GHz. This roll-off rate is a minimum since the step size here of 0.1 pm could not capture any intermediate points. The ring filter operates as a low pass edge filter with extinction > 5 dB over a 3.0 GHz wide band. This work demonstrates record-setting (to the best of the author's knowledge as of this writing) edge filter performance using nonlinear TPA-induced free carrier plasma-dispersion effects in simple ring resonators.

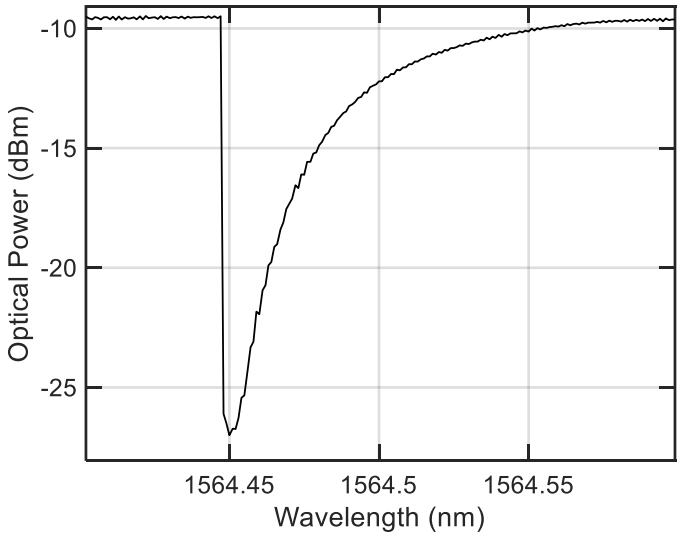

Figure 10 – Measured single ring resonator transmission responses at +0 dBm optical launch power, demonstrating no measurable insertion losses.

5.4.2 Concentric Ring Variants

Next, concentric rings were placed inside a single ring resonator identical to the ring of section 5.4.1 to modify the transmission response. To the authors' best knowledge, such concentric ring filters have only been previously reported for biosensing applications [37, 38]; these filters may be understood to be a special case of cascaded ring resonators, where

the ring-ring coupling length is extended to its limit as the average path length of the two coupled rings. Concentric rings include 2-ring, 3-ring, 4-ring, and 5-ring variants with the outermost ring radius $R_1 = 20$ µm. Inner concentric rings with a common center have radii $R_2 \ldots R_5$ such that $R_n = R_{n-1} - 0.8$ µm, resulting in nominally identical coupling gaps of 0.3 µm between each ring. The strip waveguide coupled to the concentric ring structure also had a 0.3 µm coupling gap. The responses were similarly measured as before, with highlighted results in Figure 11.

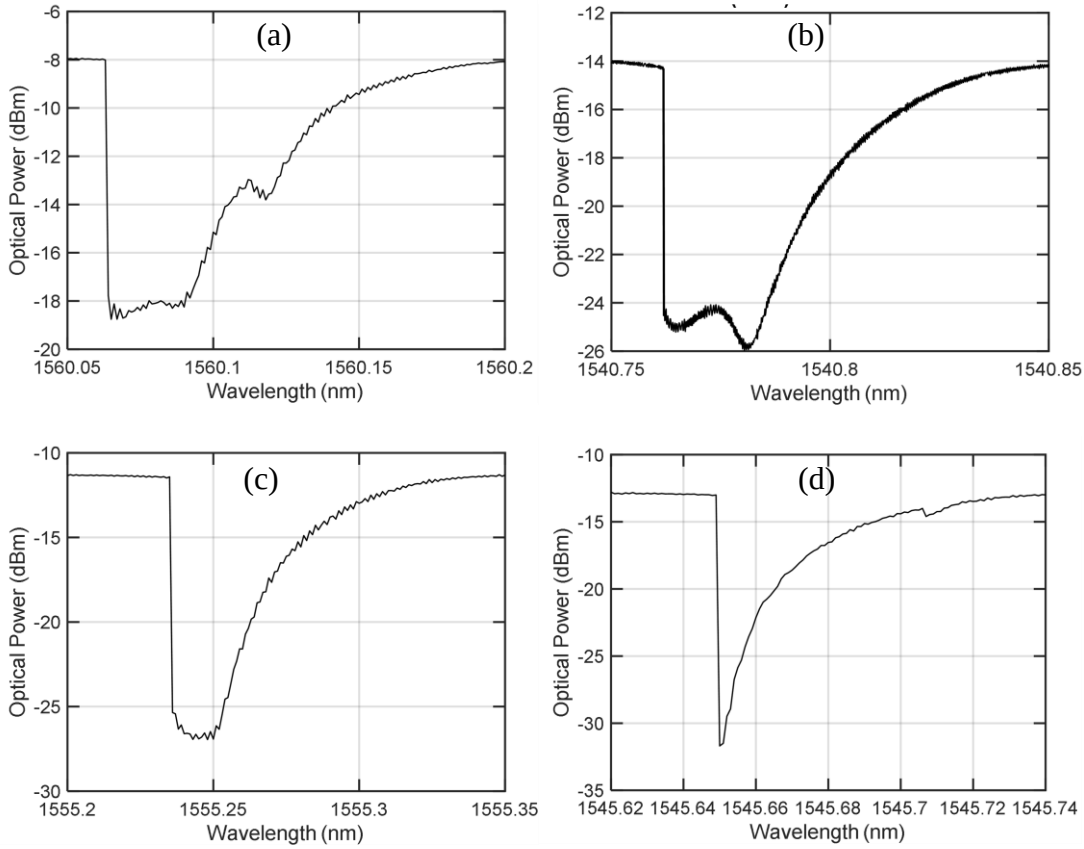

Figure 11 – Measured concentric ring edge filter transmission responses for (a) 2-ring, (b) 3-ring, (c) 4-ring, and (d) 5-ring variants.

The primary metrics of interest for each variant include the optical and effective RF 3 dB bandwidths, the roll-off rate, the peak optical extinction, and the band over which the filter behaves like and edge filter, here defined as the bandwidth over which the optical

extinction is > 5 dB. These metrics are quantified for both the single ring variant and the concentric ring variants in Table 1.

The best performing variants (single ring and 5-ring) are compared to the literature performance in Table 2. The edge filter performance here greatly outperforms previous literature known to the author in terms of roll-off, often by over three orders of magnitude.

Table 1– Summary of Nonlinear Single Ring (1-ring) and Nonlinear Concentric Ring (2-5 ring) Edge Filter Performance

	Optical 3 dB BW (MHz)	Effective RF 3 dB BW (MHz)	Roll-off Rate (dB/GHz)	Roll-off Rate (dB/nm)	Peak Optical Extinction (dB)	Optical Insertion Loss (dB)	Band for Extinction > 5 dB (GHz)
1-ring	<2.4	<1.2	>1230	>155x10^3	24.0	<0.1	3.0
2-ring	<3.8	<1.9	>790	>99.1 x10^3	10.5	<0.1	7.3
3-ring	<3.7	<1.9	>817	>103 x10^3	10.3	0.26	4.5
4-ring	<2.9	<1.5	>1020	>128 x10^3	15.5	0.13	4.9
5-ring	<2.0	<1.0	>1470	>186 x10^3	18.7	0.20	2.9

Table 2– Comparison of Optical Edge Filters in Literature

	Optical 3 dB BW (MHz)	Roff-off Rate (dB/GHz)	Roff-off Rate (dB/nm)	Peak Optical Extinction (dB)	Optical Insertion Loss (dB)
This work, single ring	<2.4	>1230	>155x10^3	24.0	<0.1
This work, 5-ring	<2.0	>1470	>186 x10^3	18.7	0.20
[30]	3.2x10^3	0.94	118	>40	-
[31]	10x10^4	~0.03	3.5	40	0.5
[32]	1.3x10^3	2.3	288	41.5	-

While the benefits of adding concentric rings for edge filters are yet unclear from the results of Table 1, the next subsection describes how such concentric ring filters in conjunction with the TPA-induced FC plasma-dispersion effect can be used to engineer superb bandpass filters.

5.5 Bandpass Optical Filters

The same concentric filters of the previous subsection also demonstrated bandpass responses at specific resonances. Generally, the resonances were edge filter responses, except where the resonances of inner rings aligned in a specific manner near the outermost ring resonance. The inner ring resonances (those corresponding to rings with radii $R_2 \ldots R_5$) must align slightly red-shifted within the tail end of the outmost ring resonance, such that a significant fraction of power can be transferred into both the R_1 ring and inner rings simultaneously. If the inner ring resonances are too far from this condition, insignificant power will enter the inner rings, resulting in very shallow transmission responses. Because the inner rings have different free-spectral ranges (FSRs) than the outer ring, this may be considered a Vernier effect, as the bandpass responses require the correct alignment of multiple resonances with different frequency spacings. This behavior is verified by a simple model of the 2-ring filter. Following the same approach as in 5.3, the ring model is modified by adding a second ring inside the first with a finite ring-ring coupling length L_2. The following electric fields are identified in the schematic of Figure 12. These fields are written:

$$E_1 = \sqrt{\frac{2P_{in}}{A_{eff}}}\left(\frac{\mu}{\epsilon}\right)^{\frac{1}{4}} \quad 5\text{-}13$$

$$E_2 = r_1 E_1 + \kappa_1 e^{j\pi/2} E_3 \quad 5\text{-}14$$

$$E_3 = r_2 e^{-j\phi_1} e^{-\alpha L_1} E_4 + \kappa_2 e^{\frac{j\pi}{2}} E_6 \quad 5\text{-}15$$

$$E_4 = \kappa_1 e^{\frac{j\pi}{2}} E_1 + r_1 E_3 \quad 5\text{-}16$$

$$E_5 = \kappa_2 e^{\frac{j\pi}{2}} E_4 + r_2 E_6 \quad 5\text{-}17$$

$$E_6 = e^{-j\phi_2} e^{-\alpha_2 L_2} E_5 \quad 5\text{-}18$$

where r_1 and κ_1 are the self-coupling and cross-coupling coefficient of the ring-bus waveguide coupling region, and r_2 and κ_2 are the coupling coefficients of the ring-ring coupling region. Likewise, ϕ_1 and α_1 are the excess phase and absorption of the outer ring, while ϕ_2 and α_2 are the excess phase and absorption of the inner ring. Solving the above system of equations for E_2 yields the following expression:

$$E_2 = E_1\left[\cos(\beta L_1) + \frac{\sin^2(\beta L_1) e^{j\pi}}{\frac{1}{Q} - \cos(\beta L_1)}\right] \quad 5\text{-}19$$

where

$$Q = \cos(\beta L_2) e^{-j\phi_1} e^{-\alpha_1 L_1} + \frac{\sin^2(\beta L_2) e^{j\pi} e^{-j\phi_2} e^{-\alpha_2 L_2}}{1 - e^{-j\phi_2} e^{-\alpha_2 L_2} \cos(\beta L_2)}. \quad 5\text{-}20$$

Here, the coupling coefficients $r_{1,2}$ and $\kappa_{1,2}$ are replaced with functions dependent on the coupling length $L_{1,2}$: $r_{1,2} = cos(\beta L_{1,2})$ and $\kappa_{1,2} = sin(\beta L_{1,2})$, where β is a coupling strength constant, dependent on the index mismatch between coupled waveguides and the coupling gap.

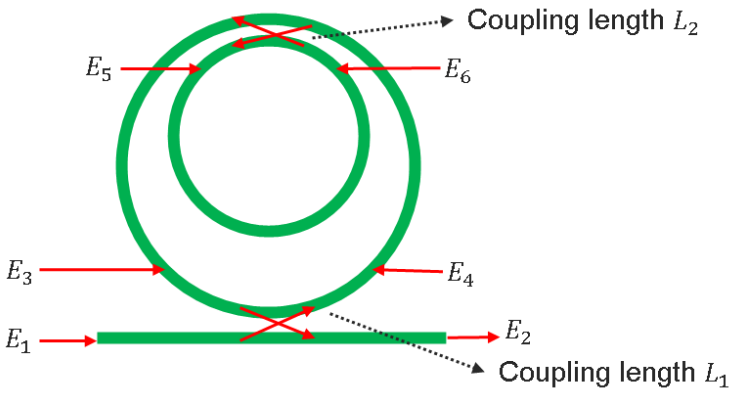

Figure 12 – Schematic of the 2-ring concentric field device with electric fields defined.

Lastly, the depiction of Figure 12 is not quite a concentric ring configuration, since the two rings are not coupling along their entire length and do not yet share a common center. Hence, the ring-ring coupling length L_2 is now set equal to the average roundtrip path lengths of the two rings, which forces the configuration to be truly concentric. Hence, $L_2 = 2\pi(R_1 + R_2)/2 = \pi(R_1 + R_2)$.

The transmission response $T = \left|\frac{E_2}{E_1}\right|^2$ is then calculated using assumed values of $\alpha_1 = \alpha_2$ =120 Np/m, A_{eff} = 0.15 µm x 0.3 µm, $\kappa_1 = 0.12$, and $\beta = 25\pi(\mathrm{n}_2 - \mathrm{n}_1)/\lambda$ where n_1 and n_2 are the Lumerical MODE calculated effective indices for rings R_1 and R_2, respectively. These are generally based on the assumptions used in 5.4.1, but are used only

to illustrate the generally operation of the concentric ring filter rather than to match experiment here.

Figure 13(a) demonstrates how the concentric ring filter operates similarly to any second order ring configuration (e.g. two rings cascaded) with slightly different roundtrip path lengths between the rings. The two sets of FSRs, when aligned, form a bandpass filter response.

Figure 13(b). This agrees with the explanation provided for forming a bandpass filter response given earlier in this subsection. When misaligned, insignificant optical power is coupled into the inner ring, leading to only small transmission notches due to the inner ring. However, the outer ring continues to demonstrate large notch filter responses at all its resonance frequencies.

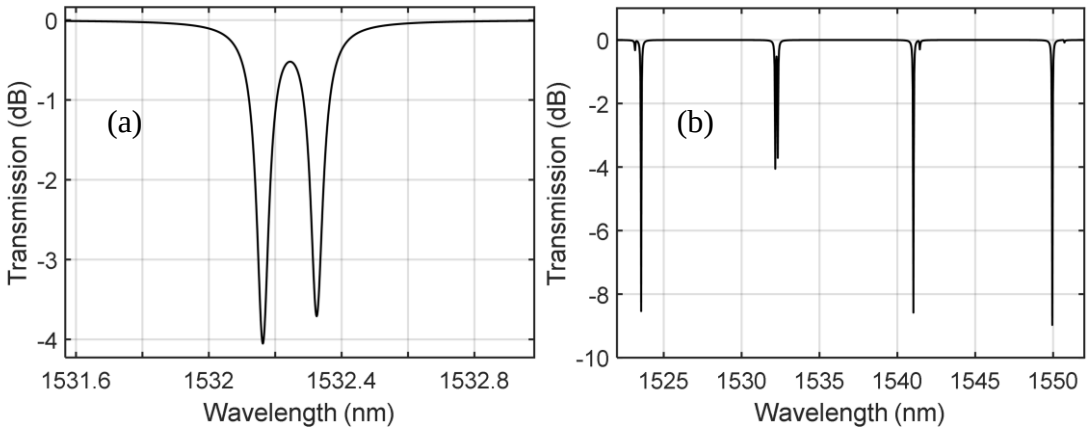

Figure 13 – (a) Calculated transmission response using the simple concentric ring model derived previously. The transmission response resembles a Vernier effect, whereby the alignment of two ring resonances with slightly different FSRs enables a narrow bandpass response. (b) Zoomed view of the bandpass response near λ = 1532 nm.

Next, the bandpass responses for 2-ring, 3-ring, 4-ring, and 5-ring concentric filters are measured, Figure 14. These responses were measured with an input optical power of 0 dBm; hence, the bandpass responses also exhibit the nonlinear effects present in section the single rings of section 5.4. Table 3 summarizes the performance metrics of each bandpass filter. The filters demonstrate optical 3 dB bandwidths between 930 MHz and 2.2 GHz with fairly flat bandpass responses (variations between 0.2 dB and 1.7 dB). The bandpass filters also demonstrate quite low insertion losses, approximately 1 to 2 dB.

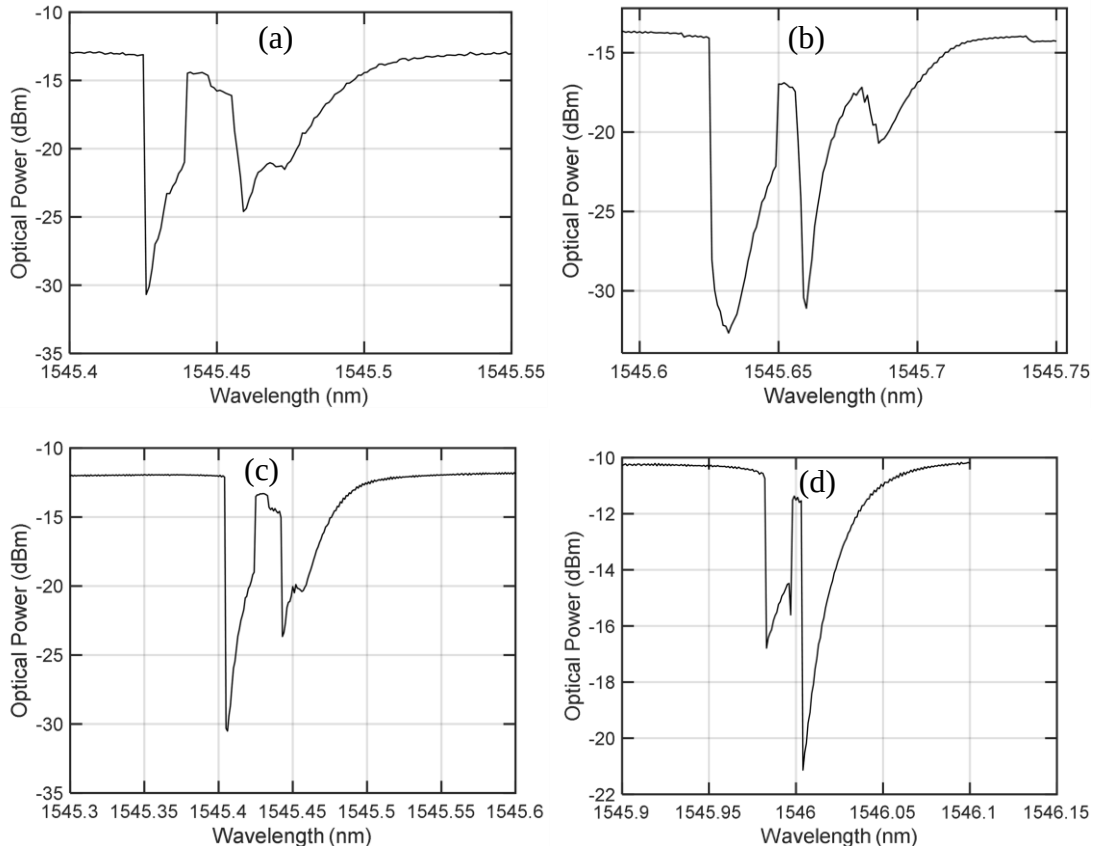

Figure 14 – Measured concentric ring bandpass filter transmission responses for (a) 2-ring, (b) 3-ring, (c) 4-ring, and (d) 5-ring variants. Performance of each filter is summarized in Table 3.

Table 3– Summary of Nonlinear Concentric Ring Bandpass Filter Performance

	Optical 3 dB BW (GHz)	Effective RF 3 dB BW (GHz)	Optical 6 dB BW (GHz)	Flatness (dB)	Peak Optical Extinction (dB)	Optical Insertion Loss (dB)	Band for Extinction > 5 dB (GHz)
2-ring	2.0	1.5	2.3	1.7	17.6	1.4	7.5
3-ring	0.93	0.75	1.4	0.6	15.8	2.9	8.8
4-ring	2.2	1.6	2.5	1.4	18.4	1.3	4.9
5-ring	0.98	0.67	~2.5	0.2	11.0	1.1	3.8

Using Lumerical MODE, the group indices n_g for the modes in rings of radii $R_1 \ldots R_5$ were calculated to estimate the FSR produced by each ring resonance. Using $FSR = \frac{\lambda^2}{n_g L}$, where λ is the optical wavelength and L is the ring's roundtrip path length, the FSRs for rings with radii $R_1 \ldots R_5$ were estimated to be FSR_1=4.90 nm, FSR_2=5.09 nm, FSR_3=5.31 nm, FSR_4=5.56 nm, and FSR_5=5.82 nm. Experimentally and by observation of Figure 14, the innermost ring resonances of the higher order filters (R_3, R_4, R_5) likely contribute little to the filter response, since it is unlikely that any one wavelength satisfies all the resonance conditions – even partially – of the outer rings (R_1 ... R_2) and inner rings simultaneously. Hence, the experimentally observed FSRs are compared to the calculations for these outer rings only, since no discernible and verifiable resonances were identified as corresponding to the inner ring resonances. The experimental FSRs for R_1 and R_2 were 4.78 nm and 4.97 nm, respectively, both slightly lower but in general agreement with the calculated FSRs.

5.6 Practical Considerations

While the filters presented in this chapter have demonstrated superb performance, practical issues in the fabrication, tuning, and deployment of such filters should be addressed. Such

filters will be at least as sensitive as ordinary add-drop ring filters, if not somewhat more sensitive due to the ultra-sharp edges demonstrated by measurement. The filters measured here demonstrated stability in frequency within 0.01 nm over a 10 minute period in a largely uncontrolled laboratory environment. In frequency, these variations correspond to shifts on the order of 1.3 GHz, which could be detrimental for many sensitive filtering applications. Hence thermal tuners with control circuitry should be implemented for deployment, as is the case for many high Q optical filters. Regarding hysteresis effects, none were observed for the filters presented here; sweeping the wavelength in the forward and reverse directions produced the same results.

Another challenge for high-performance optical filters is the variation among devices due to fabrication errors. Using the Globalfoundries 90 nm SiP process, identical filters fabricated on different parts of the chip varied in resonant wavelength by approximately +/-0.1 nm for a sample size of four. Hence, for a target resonant wavelength of 1545.5 nm, the same design could exhibit resonances between 1545.4 nm and 1545.6 nm. While thermal tuning can easily adjust the resonant wavelength, smaller process nodes like those offered by the Globalfoundries 45CLO (45 nm) process could significantly reduce the resonant wavelength variation from device-to-device.

One aspect of these filters yet to be decisively demonstrated is how the filters interact with high-speed signals, as these signals may reveal filter features imperceivable to single-tone sweeps. It is possible that the optical filters here preliminarily characterized could show time-variant features that are less desirable in a filter. For example, [36] indicated such TPA and free carrier plasma-dispersion effects enable all-optical modulation with bandwidths limited on the order of 10 GHz. However, a filter need not demonstrate high-

speed modulation characteristics to be useful. The time limitation of the all-optical modulator in [36] arises from the relatively long lifetime of the free carriers, which can range anywhere picosecond to nanosecond regimes in silicon waveguides. However, filtering with TPA-induced free carrier plasma-dispersion effects only requires the maintenance of a high free carrier density within the ring in order to achieve the high-performance filter metrics characterized previously. If these free carriers are not present as a high-speed signal impinges on the filter, the signal will pass before significant free carrier concentrations can be generated to induce the high spectral roll-off desired. Hence, a simple method of overcoming the "startup time" for the filter is to introduce a pilot tone (a CW pump) at the resonance to maintain a constant flux of TPA-generated free carriers in the ring. The pilot tone should have a high average power, significantly larger than that of the signal to be filtered, because these filters are functions of optical power. A high-power pilot tone can help stabilize the filter from responding to variations in average signal power.

This chapter has described edge filters with the sharpest roll-offs of any integrated photonic filters to date (to the author's knowledge) as well as bandpass filter variants, all leveraging TPA induced free carrier plasma-dispersion effects. These filters could herald the next generation in optical filters for microwave photonics, enabling narrowband RF channelization, system linearization by removing unwanted sidebands, carrier suppression, single-sideband modulation schemes, and more.

CHAPTER 6. SYNTHETIC POCKELS EFFECTS IN SILICON

6.1 Integrated Photonic Modulators/Transmitters for Analog Applications

While integrated photonic modulators have been successfully commercialized after two decades of research, they remain largely optimized for digital applications, such as those for datacenter and long-haul networks. Many IMWP applications require the modulation of analog signals, requiring attention to distinct link metrics, such as noise figure, gain, and spur-free dynamic range ($SFDR$), as well as other linearity metrics. Linearization of integrated photonic modulators is key to enabling IMWP technologies to compete with discrete MWP systems and for adoption in new deployment opportunities, such as aerospace communications and modern warfighter systems.

Though the Pockels effect used by $LiNbO_3$ modulators is near-perfectly linear, the intrinsic transfer function of the Mach-Zehnder interferometer is nonlinear – sinusoidal to be precise. The need for highly linear MWP systems spurred many efforts in the 1990s to linearize the $LiNbO_3$ Mach-Zehnder modulator (MZM) response by a variety of methods, including the use of series and parallel dual MZM architectures [39, 40], dual wavelength and polarization schemes [41], and feedforward and predistortion methods. Because these methods addressed nonlinearities generated by the MZM architecture, they were immediately applicable to *integrated* MZMs as well and provided a nice starting point as integrated modulators emerged in the 21st century.

However, the previous linearization methods of $LiNbO_3$ were insufficient, since new integrated modulators relied on the plasma-dispersion effect, in which the index of refraction is modulated by depletion (or injection) of free carriers by a voltage [42]. Despite the relatively good efficiency of the plasma-dispersion effect, it is unfortunately non-linear, being roughly square-root-like or natural log-like in its index vs. voltage response, resulting

in the need for intrinsic device linearization. Dopant placement and active length optimization [43-46] are demonstrated methods of linearization. Other methods augment the interferometer structure, such as by ring-assisted MZMs [47, 48] or through parallelization of the MZM structure [49, 50].

A third strategy for linearizing integrated modulators lies in their operation. Driving the integrated modulators differentially has demonstrated improved linearity [51, 52]. Other works have used pn junction reverse bias and MZM bias point optimizations to reduce nonlinearities [43, 46, 53-56]. The MZM bias point can compensate for fabrication errors in MZM length and pn junction characteristics [45, 46]. Particularly, Sorace-Agaskar *et al*. demonstrated that active length optimization can reduce nonlinearities by careful control of the nonlinearity-generating mechanisms, namely i) the inherent MZM transfer function shape, ii) the nonlinear refractive index response, and iii) the optical loss response [43, 56]. These three mechanisms generate intermodulation distortion products (IMDs).

Typically, the linearity of MWP systems spanning less than an octave is limited by these IMDs (as opposed to harmonics). The MZM (apart from external electronics) is often the limiting component and generates third-order IMD (IMD3) that are difficult to filter out given their proximity to the signal of interest. Thus, linearization efforts often use metrics based on measurements of the IMD3 and its relative strength to the fundamental signal.

Highlighted in this work is the exploitation of silicon's $\chi^{(3)}$ effect for the linearization of SiP MZMs and as a standalone linear effect for pure phase modulation, i.e. a "synthetic" Pockels effect in silicon.

6.2 DC Kerr Effect Theory

The DC Kerr effect onsets when a strong electric field breaks of the intrinsic centro-symmetry of silicon (or similar crystals). This strong DC electric field E_{DC} induces a third-order polarizability to the silicon of the form:

$$P^3_{x,\,tot}\,(\omega_o) = 12\varepsilon_0\chi^{(3)}_{xxxx}E_{opt}\,E^2_{DC}e^{-j\omega_o t} \tag{6-1}$$

where $\chi^{(3)}_{xxxx}$= 2.45 × 10^{-19} m^2 V^{-2} is the third-order nonlinear susceptibility [57, 58]; ε_{Si} is the relative permittivity of silicon; and ω_o is the optical angular frequency. Here, E_{DC} is the DC applied field magnitude, and E_{opt} is the optical electric field magnitude. Upon adding an AC modulating field E_{AC} with angular frequency ω_{AC} in addition to the DC field, the third-order polarizability of the silicon has new components governed by

$$P^3_{x,\,tot}\,(\omega_o + \omega_{AC}) = 12\varepsilon_0\chi^{(3)}_{xxxx}E_{opt}\,E_{DC}\,E_{AC}\,e^{-j(\omega_o+\omega_{AC})t}. \tag{6-2}$$

Each of these third-order polarizabilities lead to an index change governed by the two equations (for DC fields and DC+AC fields, respectively):

$$\Delta n_{DC} \approx \frac{6\chi^{(3)}_{xxxx}E^2_{DC}}{\sqrt{\varepsilon_{Si}}} \tag{6-3}$$

$$\Delta n_{AC} \approx \frac{6\chi^{(3)}_{xxxx}E_{DC}E_{AC}}{\sqrt{\varepsilon_{Si}}} \tag{6-4}$$

While the linear electro-optic effect, or “Pockels” effect, exhibits a linear index response with respect to voltage or electric field, the plasma-dispersion (PD) effect exhibits an index response roughly proportional to $\sqrt{V}$ because of the junction depletion width’s $\sqrt{V}$

dependence. See Table 4 for a summary of Pockels, plasma-dispersion, and DC Kerr effects.

Table 4– Comparison of Pockels, plasma-dispersion, and DC Kerr effects.

	Pockels	Plasma-Dispersion	DC Kerr (DC)	DC Kerr (DC+AC)
Material Polarization	$\epsilon_0\chi^{(1)}E$	N/A	$\epsilon_0\chi^{(1)}EEE$	$\epsilon_0\chi^{(1)}E_{opt}E_{DC}E_{AC}$
Δn_{eff}	$\propto V_{DC\|AC}$	$\propto \sqrt{V_{DC\|AC}}$	$\propto V_{DC}^2$	$\propto V_{DC}V_{AC}$
$\Delta\alpha$	~0	$\propto -\sqrt{V_{DC\|AC}}$	~0	~0
Control Parameter	DC or AC Voltage	DC or AC Voltage	DC Voltage	DC+AC Voltages

For both PD and Pockels effects, both DC and AC voltages modulate the phase according to the same function; e.g. for a $LiNbO_3$ phase shifter, a DC field and an AC field both theoretically induce a linear change in optical phase. However, DC Kerr effects exhibit functionally different behaviors in the DC and AC cases since the DC Kerr effect is dependent on the strength and frequency of the third field (besides the optical field and the modulating field). In the DC case, the third field is degenerately E_{DC}, and the index change response with electric field in quadratic. Thus, in practice, the optical carrier phase can be tuned quadratically with the applied voltage. However, when DC+AC fields are applied to a phase shifter, the relevant index response to the signal is not quadratic, but proportional to E_{AC}, enabling near-perfect linear phase modulation. To further clarify this distinction, the strength of the optical sideband generated by modulating a phase shifter with DC+AC fields is a function of $E_{DC}E_{AC}$; however, the carrier phase is tuned by E_{DC}^2. Hence, the DC Kerr effect is unique in that DC voltages do not equally affect both signal and carrier, as is

typically true in Pockels and plasma-dispersion effects. Intrinsically, the voltage required for a π phase change will be different in the DC and AC cases.

One may wonder whether there is a case where E_{AC} is degenerate and leads to a useful quadratic AC index response. Indeed, this component occurs and exhibits a third order polarizability of the form

$$P^3_{x,\,tot}\,(\omega_o + 2\omega_{AC}) = 12\varepsilon_0\chi^{(3)}_{xxxx}E_{opt}\,E^2_{AC}\,e^{-j(\omega_o+2\omega_{AC})t} \qquad 6\text{-}5$$

However, this degenerate E_{AC} case does not produce index modulation at the fundamental frequency of interest, but rather at a second harmonic, $2\omega_{AC}$ [59].

6.3 SiP Transmitter Linearization

An important distinction to make is that the goal for an intensity-modulated analog link, like that described in Chapter 3, is not to engineer a perfectly linear phase shifter. While a perfectly linear phase shifter is exactly what is desired for phase-modulated links, intensity modulated links require that the amplitude modulation is linear rather than the phase modulation. Practically, this means the goal for intensity modulated links is to engineer a phase shifter response that compensates the Mach-Zehnder interfometer response to yield linear amplitude modulation. In silicon, this phase shifter engineering can be accomplished through careful control of plasma-dispersion (PD) effects, loss responses, and as shown here, the DC Kerr effect.

Though largely ignored until recently, silicon exhibits a $\chi^{(3)}$ effect [57-59] strong enough to significantly modulate the refractive index in silicon photonic modulators. The incorporation of the DC Kerr effect in SiP modulators adds a degree of control over the phase shifter index response, since DC Kerr and plasma-dispersion effects exhibit different functional forms of refractive index with respect to electric field (or voltage). Hence, the

DC Kerr effect can be used cooperatively with PD effects to engineer a more linear phase shifter, or a more linear overall MZM. As will be shown, a combination of PiN junction design and tunable reverse bias can vary the relative contributions of PD and DC Kerr effects, which together determine the overall modulator transfer function (electrical to optical conversion). At the time this work was performed, previous analyses of SiP MZM nonlinearities had not sufficiently included the DC Kerr effect. In this section, a combination of experiments and simulations demonstrate how judicious choice of PiN junction design, phase modulator reverse bias, and MZM bias point can improve modulator and hence system linearity, i.e. link $SFDR$.

Two MZMs were fabricated in the AIM Photonics process, each using custom-designed phase shifter cross-sections (PN and PiN junctions) depicted in Figure 15. The PiN junction modulator is expected to demonstrate a greater ratio of DC Kerr effects to plasma-dispersion effects than the PN modulator. The MZMs use thermo-optic phase shifters to set the bias points in one of the MZM arms. Because the thermally tuned refractive index responses vary nearly linearly with heater power, the electrical power consumed by the thermo-optic phase shifters acts as a proxy for the MZM bias point.

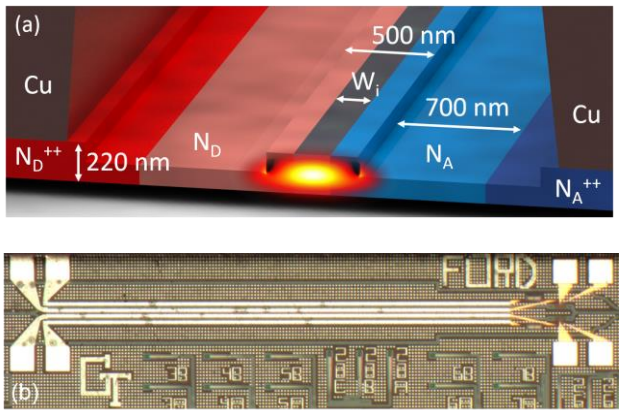

Figure 15 – (a) Cross-sectional schematic of phase modulator structure with simulated mode profile. W_i is the width of the undoped intrinsic region. The PN MZM has W_i = 0 nm, and the PiN MZM has W_i = 200 nm. (b) Top-down image of the fabricated MZM. The PN and PiN modulators are identical except for a difference in W_i.

6.3.1 DC Characterization and Simulations

First, the current-voltage (IV) responses of PN and PiN junction diodes specified in Figure 15 were measured, which yields important information regarding the range of useable reverse biases. The IV curve data, Figure 16, exhibit breakdown voltages of -8.1±0.1 V and -10.5±0.1 V for the PN and PiN structures, respectively. Hence, the DC bias voltages should remain below these breakdown voltages to avoid generating high nonlinearities, as is demonstrated later in this section.

Because the DC Kerr effect has been largely ignored until recently, commercial tools were augmented with custom MATLAB code to account for its contribution to index modulation. The plasma-dispersion index and absorption responses were calculated using Lumerical DEVICE and MODE [60]. Lumerical DEVICE, a 2D/3D charge transport solver, handles the electrical carrier perturbations with voltage in the PN or PiN junction geometry, and separately MODE calculates the optical properties of the waveguide as a function of the voltage, informed from the carrier dynamics from the DEVICE simulation. While MODE (which simulates optical modes, effective indices, and free carrier absorption) calculates the plasma-dispersion effect well based on the Soref/Bennet model [42], it does not yet (as of this writing) include DC Kerr effects in a convenient manner. Hence, custom Matlab code was developed to use the applied and optical electric fields from DEVICE and MODE, respectively, to calculate the contribution of DC Kerr effects as a function of voltage for both PN and PiN junction designs [59]. Because the DC Kerr effect incurs negligible loss, simulations assume plasma-dispersion (free carrier) absorption dominates the loss response. The simulation workflow is depicted schematically in Figure 17.

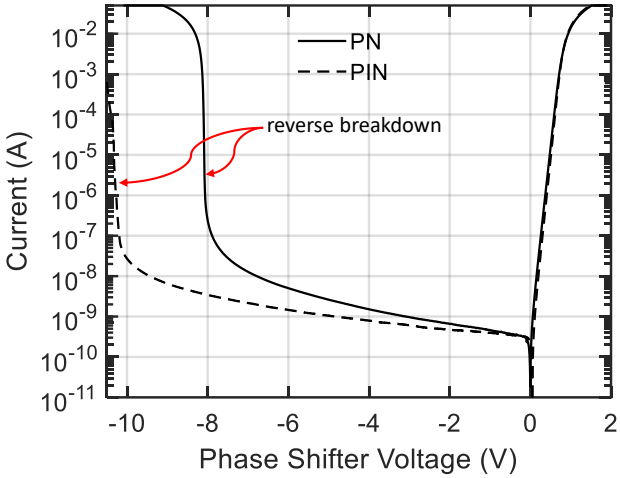

Figure 16 – Measured IV curves for PN and PiN phase shifters. Breakdown voltages limit the range of useful reverse bias voltages.

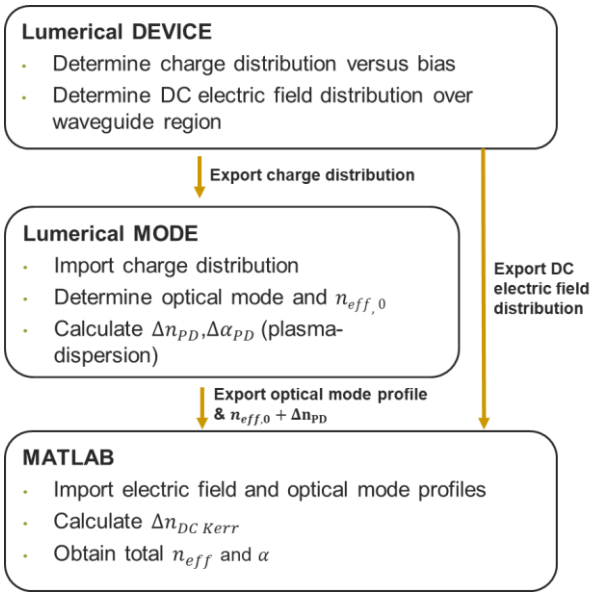

Figure 17 – Simulation workflow between Lumerical DEVICE, MODE and custom MATLAB code to calculate both plasma-dispersion and DC Kerr effects generated by a phase modulator.

SiP platforms hence have two modulation effects with different index vs. voltage functions at disposal. As a result, *transfer function engineering* can be accomplished by combining PD and DC Kerr effects through PiN junction design and tunable DC bias on phase shifters.

The index responses for both PN and PiN based MZMs were measured by sweeping the bias voltage applied V_{bias} to one phase shifter and measuring both bar and cross optical outputs (optical powers P_{bar} and P_{cross}, respectively). The optical transmission was measured per the biasing scheme of Figure 18(a), yielding measured transfer functions of both PN and PiN modulators in Figure 18(b) and Figure 18(c).

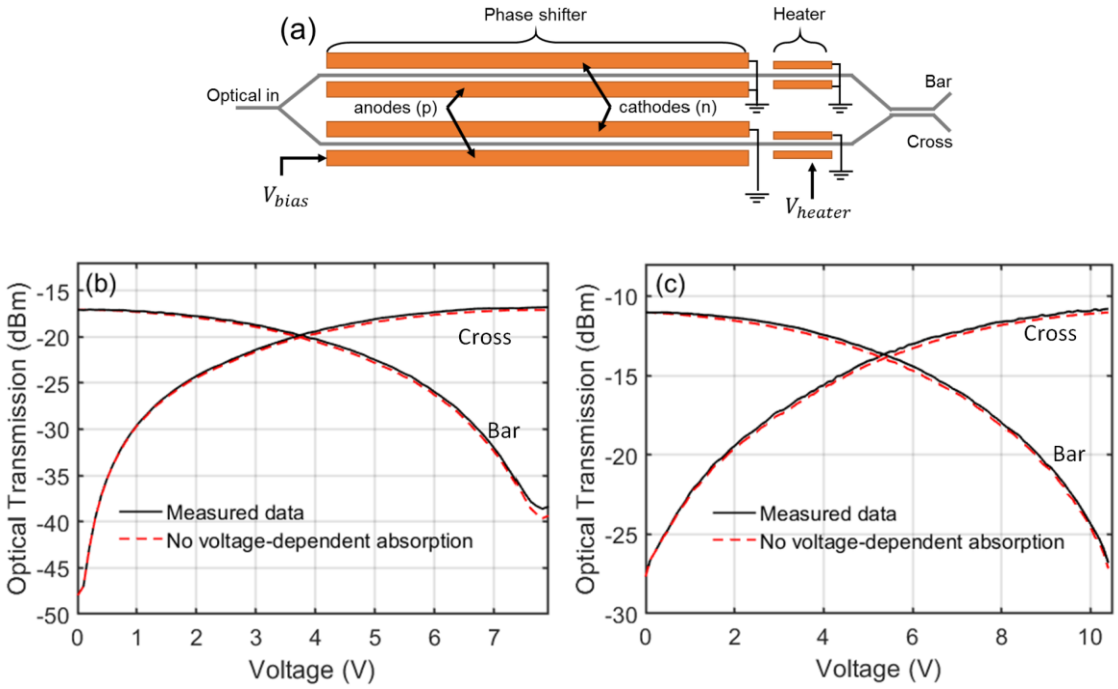

Figure 18 – (a) Biasing scheme for measuring the transfer functions of the SiP MZMs. Thermo-optic phase shifters adjust the relative phase between Mach-Zehnder arms to set the MZM bias point. The DC electrical-optical responses are shown in (b) for the PN modulator and (c) for the PiN modulator. The x-axis represents reverse bias. The transfer functions without voltage-dependent absorption are shown by using the extracted index changes only. This illustrates how voltage-dependent absorption affects, albeit weakly, the MZM transfer functions.

Because both optical outputs are measured simultaneously as a function of V_{bias}, the index response Δn_{eff} and absorption response $\Delta \alpha L$ can be uniquely extracted per the following equations:

$$\Delta n_{eff} = \frac{\boldsymbol{\lambda}}{2\pi L}\cos^{-1}\left(-\frac{P_{bar} - P_{cross}}{e^{-2\alpha_0 L}e^{-\Delta\alpha L}|E_i|^2}\right) \quad 6\text{-}6$$

$$\Delta\alpha L = \frac{-1}{2}ln\left(\frac{2(P_{bar} + P_{cross})}{e^{-2\alpha_0 L}|E_i|^2} - 1\right) \quad 6\text{-}7$$

where λ is the optical wavelength; L is the phase shifter active length, α is the absorption per unit length (hence αL is total phase shifter loss in dB); $\alpha_0 L$ is the zero-bias phase shifter loss or insertion loss; and E_i is the input optical electric field. While the Δn_{eff} response can be uniquely extracted, experimentally determining the contributions to this total index response is challenging. Hence, simulations are used to estimate the relative contributions of the DC Kerr effect and plasma-dispersion effect to the extracted Δn_{eff}. Given limited knowledge of the foundry's process, the index and absorption responses are fit in simulation, allowing for variation of only two uncertain parameters: dopant concentration and junction depth (spread). Varying these two parameters within the relatively narrow ranges common to SiP foundry capabilities and phase shifter designs, the Δn_{eff} and $\Delta\alpha L$ responses were matched well for both PN and PiN modulators, both using the same process assumptions (because they are from the same silicon die). Both simulated and experimentally extracted responses for PN and PiN modulators are shown in Figure 19.

Figure 19(a) demonstrates a nearly linear index response with voltage, indicating DC Kerr effects are significantly augmenting the PD effect's $\sqrt{V}$ dependence. In

Figure 19(b) the DC Kerr effect is even more apparent, as its quadratic response inverts the curvature of the total index response, given a higher ratio of DC Kerr to PD effect in the PiN modulator. Note that, even when simulated for wide variations in extracted parameters, the plasma-dispersion effect alone cannot achieve the index/absorption responses of Figure 19. In the next subsection, this DC Kerr effect used to linearize the MZM response.

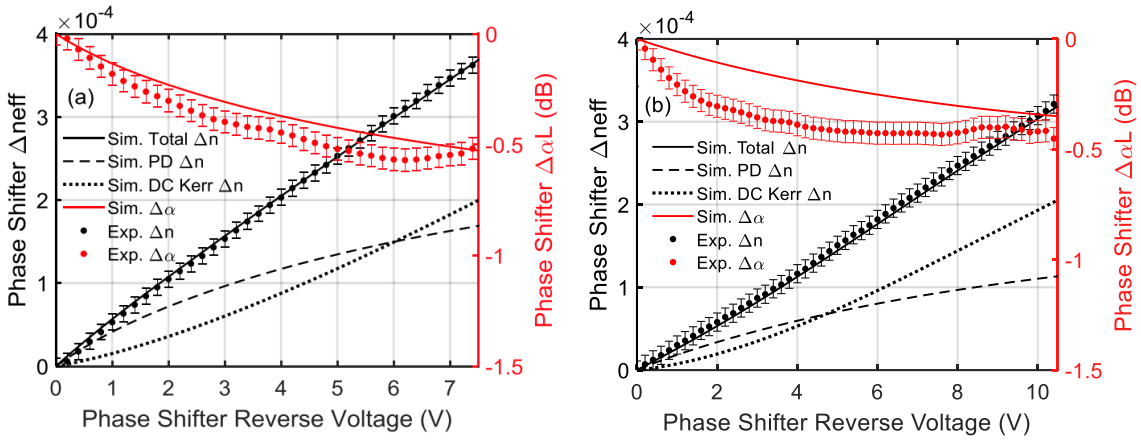

Figure 19 – Extracted effective index response and absorption decrease for (a) PN junction and (b) PiN junction based SiP phase shifters, demonstrating strong DC Kerr effects as the PD effect alone cannot account for the near-linear index response of (a) and the negative curvature or quadratic response of (b).

The DC performance metrics, including $V_\pi L$, insertion loss, the avalanche breakdown voltage, and the DC extinction ratio, are summarized for both PN and PiN modulators in Table 5.

Table 5– Summary of SiP Modulator DC Performance.

METRICS	PiN MZM	PN MZM
$V_\pi L$ (V·cm)	2.08±0.02	1.56±0.02
Insertion Loss (dB)	7.5±1	10.5±1
Breakdown Voltage (V)	-10.5±0.1	-8.1±0.1
DC Extinction Ratio (dB)	>17	>20

6.3.2 SiP Transmitter Linearity

A useful first step in assessing the linearity of an RF electronic or optical component or system is the measurement and observation of the intermodulation distortion products (IMDs), typically the second and third order IMDs (IMD2s and IMD3s), since these are the distortions which often limit the system $SFDR$. The IMDs are measured for the PN and

PiN modulators using a setup depicted in Figure 20. Here, two RF tones close in frequency (100 MHz apart) are added electrically and input to the modulator. The fundamental, IMD2, and IMD3 RF powers and average output optical power were tracked simultaneously as a function of MZM bias point (set by thermo-optic phase shifter) with PN and PiN junctions reverse biased at -5V, Figure 21. For modulators with nearly perfectly linear phase shifters, e.g. lithium niobate modulators, the fundamental and IMD3 align and behave functionally similar versus bias point, while the IMD2 and all other even-ordered distortions behave oppositely. For the PN and PiN silicon photonic responses of Figure 21, the RF fundamental and IMDs appear to roughly follow the behavior of MZMs with linear phase shifters: the fundamental/IMD3 are minimized where the optical transmission is at its extremes. The IMD2 is minimized near the -3 dB optical transmission points, what would nominally be called the quadrature point for lithium niobate modulators. Upon closer inspection, however, these behaviors are imprecisely manifested due to the nonlinear index responses of the SiP phase shifters. From Figure 21(a), the fundamental null (e.g. at ~45 mW) is misaligned or shifted horizontally from the IMD3 null (e.g. at ~40 mW). Given these results were measured simultaneously, there is no error in the position of the nulls due to bias point drift over time. Hence, these results demonstrate how the nonlinear index responses of SiP phase shifters can result in decoupling of the fundamental from the IMD3, opening the door to modulator linearization. In modulators with perfectly linear phase shifters, the ratio of the fundamental to the IMD3 is theoretically constant vs. bias point; hence, counterintuitively, introducing nonlinearities into the phase shifter can enhance the fundamental-IMD3 ratio and hence increase device and system linearity as quantified by $SFDR$.

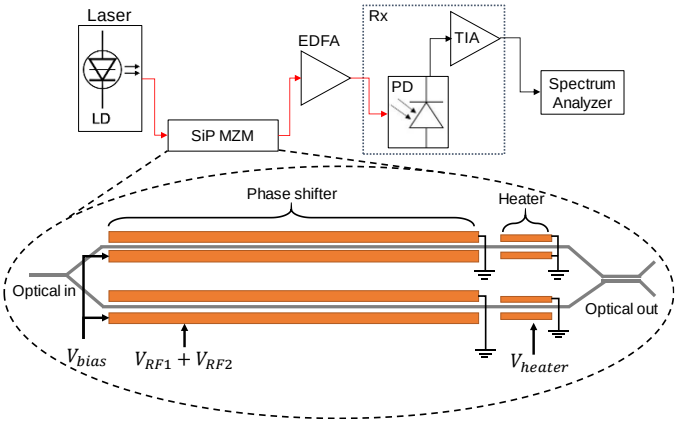

Figure 20 – Link configuration for IMD and $SFDR$ measurements along with the SiP MZM biasing (DC) and driving (RF) scheme. The parameter V_{bias} controls the strength of the DC Kerr effect and (weakly) the amount of absorption in the phase shifters. The parameter V_{heater} adjusts the relative phase between the two arms of the MZM.

Unlike lithium niobate MZMs, silicon photonic MZMs possess two distinct types of bias: reverse bias on the phase shifters and the MZM bias point that sets the relative phase between MZM arms. In lithium niobate MZMs, applying a DC field to one arm of the MZM can set the bias point in a way indistinguishable from applying the DC field to a separate phase shifter, apart from the RF modulation electrodes. In SiP modulators, the interferometer bias point is typically set by thermal phase shifters, while reverse biases are applied to the RF electrodes to prevent the PN or PiN junctions from swinging into the forward bias regime when modulated by a signal. This reverse bias improves modulation speed by reducing junction capacitance and avoiding the perturbation of large carrier concentrations. Hence, silicon photonic MZMs possess an additional degree of freedom through the reverse bias of the PN/PiN junctions. Hence, the IMDs are explored as a function of reverse bias as well.

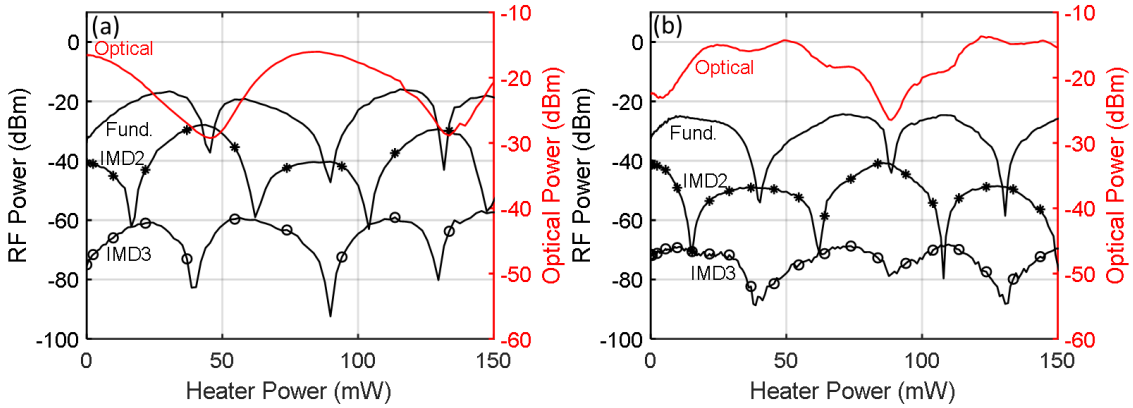

Figure 21 – Two-tone experimental results and measured optical responses measured vs. MZM bias point (heater power) for the (a) PN modulator and (b) PiN modulator. Sweeping MZM bias point (heater power) on one arm reveals a shift between fundamental and IMD3 minima. The optimal heater power and reverse bias combinations are made clear in Figure 23 and Figure 24 for PN and PiN modulators, respectively.

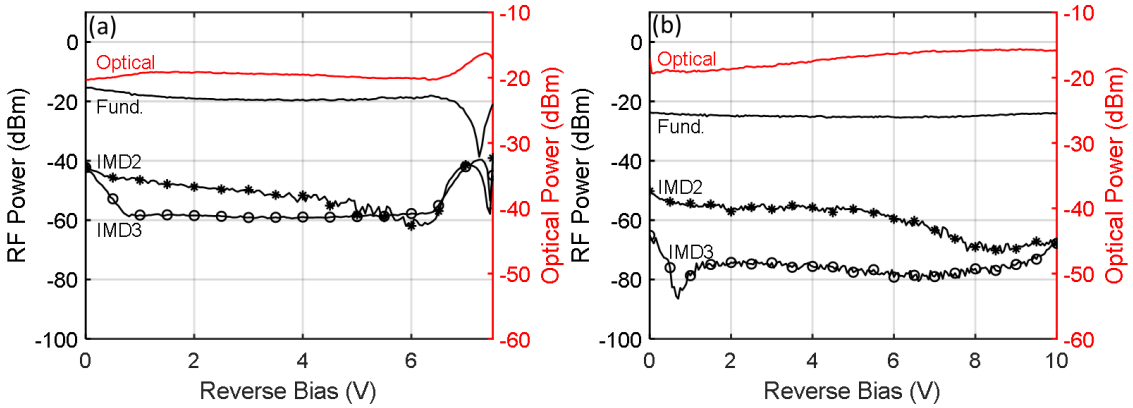

Figure 22 – Two-tone experimental results and measured optical responses measured vs. reverse bias for (a) the PN modulator and (b) the PiN modulator. Sweeping reverse bias voltage on both arms simultaneously exhibits optical loss and IMD2 reduction, with minor variations in fundamental and IMD3 powers. The optimal heater power and reverse bias combinations are made clear in Figure 23 and Figure 24 for PN and PiN modulators, respectively.

The two-tone results of Figure 22 demonstrate the change in linear and nonlinear behaviors of the (a) PN and (b) PiN based phase modulators versus reverse bias. As the reverse bias in increased, the interplay of the PD effect, DC Kerr effect, and absorption response changes the transfer function shape and hence the magnitudes of the linear (fundamental)

and nonlinear (IMD2 and IMD3) terms. These results hint at a complex bias space (comprised of two free variables: reverse bias and MZM bias point), which is fully explored next.

To explore the bias space fully, the RF fundamentals, IMD3s, and optical power are tracked while the reverse bias is swept for fixed heater powers, incremented from 0 to 150 mW. From the measured fundamentals and IMD3s are calculated the approximate gain, NF, and $SFDR$ across the entire bias space for both links employing the PN and PiN based modulators, Figure 23 and Figure 24, respectively. Here, the $SFDR$s are estimated by using a single pair of fundamental and IMD3 data points, assuming slopes of one and three with increasing RF input power, and extrapolating the data to the measured noise floor (noise power spectral density). Here the noise floor was limited by the electrical spectrum analyzer to -152 dBm/Hz.

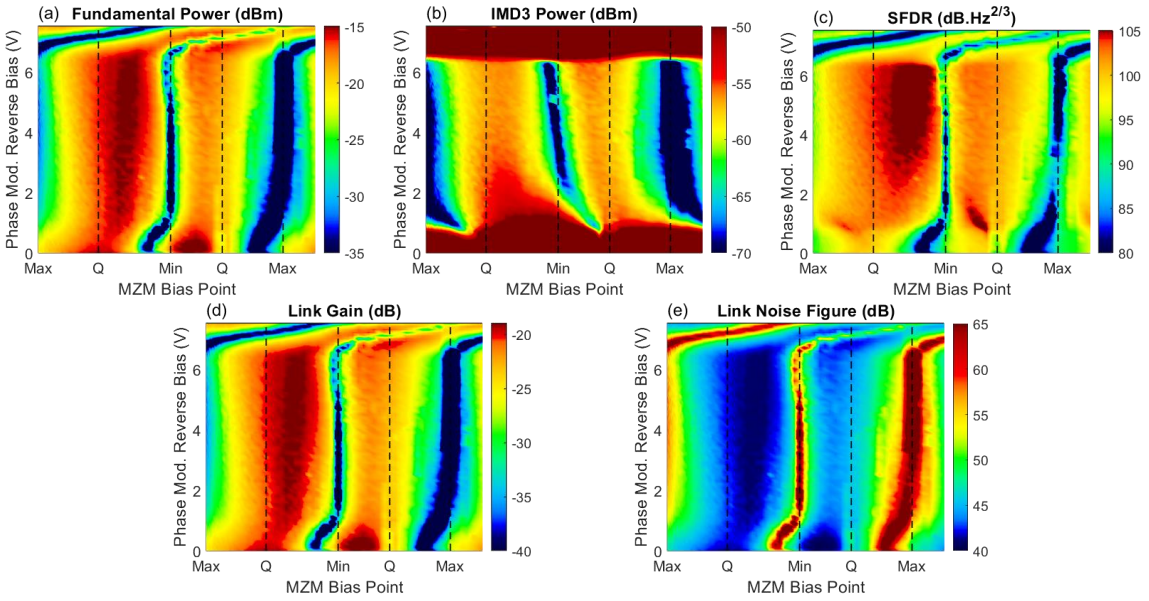

Figure 23 – Contour plots for the PN MZM of the (a) measured fundamental RF power, (b) measured IMD3 power, (c) extracted link $SFDR$ showing optimal performance at high reverse biases (-4 V to -6 V) and MZM bias points between the first Q and Min, (d) extracted link gain, and (e) extracted link noise figure. Metrics are defined in detail in Chapter 2.

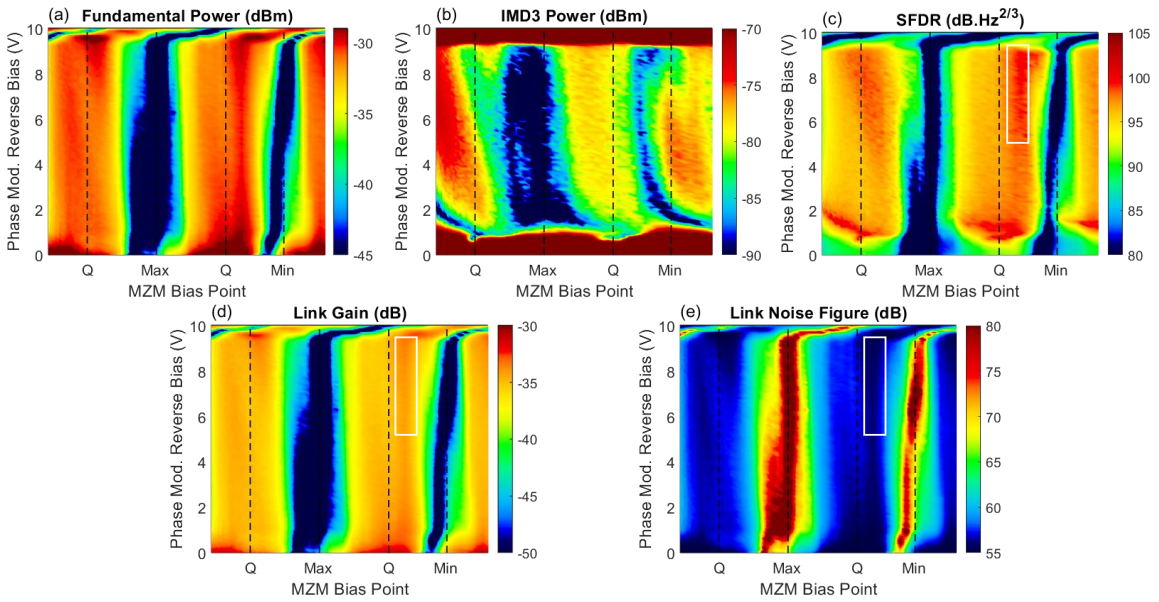

Figure 24 – Contour plots for the PiN MZM, shown versus phase modulator reverse bias (equally applied to both arms) and MZM bias point: (a) measured fundamental RF power, (b) measured IMD3 power, (c) extracted link $SFDR$ showing optimal performance at high reverse biases (-5 V to -9 V) and MZM bias points between the second Q and Min, (d) extracted link gain, and (e) extracted link noise figure. The input RF power is +4 dBm. The white boxes marked in (c), (d), and (e) indicate the optimal biasing space. Metrics are defined in detail in Chapter 2.

Commentary is limited to the contour plot measurements for the PN modulator results of Figure 23 for simplicity; the PIN modulator results of Figure 24 demonstrate similar features. These contour plots demonstrate many of the behaviors exhibited in the 2D cuts through the bias space, such as the shifts in the IMD3 null away from the fundamental nulls and the general periodic nature of the fundamentals and IMDs versus MZM bias point. From both Figure 22(a) and Figure 23(b), the IMD3s rise significantly for reverse biases < 1V due to voltage-dependent depletion capacitance and effects from the AC signal swinging into forward biased regimes. The voltage-dependent depletion capacitance scales approximately as $1/\sqrt{V}$ and can limit linearity performance; hence, high reverse bias is helpful beyond its usefulness in generating DC Kerr effects by reducing capacitance [61]. On the other end of the reverse bias extreme, as the diode avalanche breakdown voltage is

approached (by comparing to the IV curves of Figure 16), the nonlinearities rapidly increase beyond -7V to the detriment of the system linearity.

For IMDD links using discrete components, the link $SFDR$ is maximized when the $LiNbO_3$ MZM bias point is set to its quadrature point (nominally the -3 dB transmission point) when limited optical power precludes the use of low-biasing techniques. However, in the case of the silicon photonic transmitters here, Figure 23 and Figure 24 indicate optimal $SFDR$ (as well as gain and NF) are achieved at MZM bias points between the nominally quadrature (-3 dB transmission point) and null bias (minimum transmission). For example, in the PN modulator case of Figure 23(c), the $SFDR$ is significantly increased at a bias lower than quadrature for a -5 V reverse bias.

While the results here were tested using a tones near 1 GHz, the results were also verified for higher frequencies including two tone tests near 2 GHz, 5 GHz, and 10 GHz. Hence, the bias point optimization holds for wideband modulation over a range acceptable for S, C, and X band satellite communications (for example) Higher speed modulators are required for extending the application range to cover Ku, K, and Ka band communications. The PiN based modulator exhibited similar behaviors as those described here for the PN based modulator.

From the fundamental and IMD3 data measured in Figure 23(a,b) and Figure 24(a,b), the $IIP3$s and $OIP3$s can be estimated (see section 2.3 for $IIP3$ and $OIP3$ definitions). Further, the ratio of $OIP3$ to $IIP3$ yields the approximate link gain G (Figure 23(d) and Figure 24(d)) across the bias space. Similarly, the noise figures (Figure 23(e) and Figure 24(e)) are estimated by $NF = 174 + N_{out} - G$, where N_{out} is the noise floor (dBm/Hz); G is in dB; and N_{out} is in dBm/Hz [5].

Lastly, the single-point method of estimating the $SFDR$ in Figure 23(c) and Figure 24(c) is compared to the multi-point method of measuring the $SFDR$, where the extrapolation of

the fundamental and IMD3 tones are not based on assumed slopes of 1 and 3, respectively, but rather are fitted to fundamental and IMD3 data taken at multiple RF input powers. The multi-point assessment of the $SFDR$ is exemplified by Figure 25(a). Here is shown the equal-amplitude, two-tone experimental results for the PN modulator, biased near slightly off quadrature with a reverse bias of -5 V. The filled circles indicate experimental data points for the fundamental (black) and IMD3 (red). These data points are fitted and extrapolated (solid black and red lines) to the measured noise floor of -152 dBm/Hz The dashed black and red extrapolations indicate the expected experimental results if the excess EDFA amplification is removed, resulting in a 103 dB·Hz$^{2/3}$ $SFDR$.

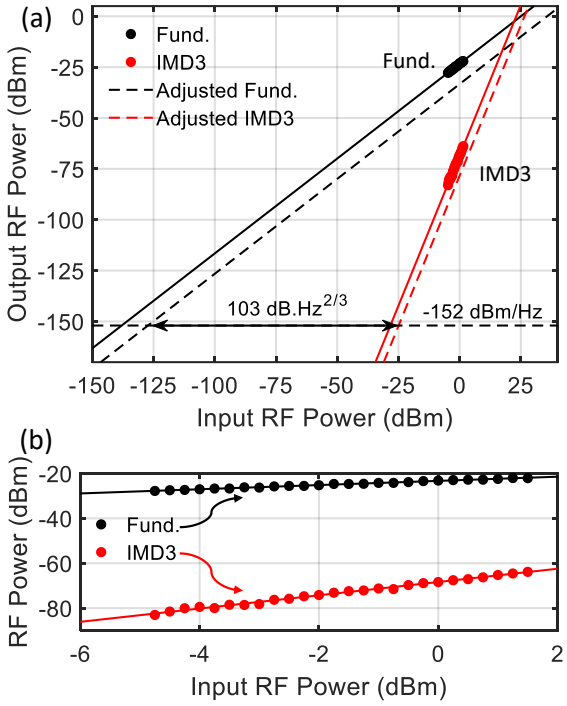

Figure 25 – (a) Multi-point link $SFDR$ measurement with the PN MZM, showing $SFDR$ = 110±2 dB·Hz$^{2/3}$ at an MZM bias point just before the second quadrature point and for -5 V PN junction reverse bias. Adjustment for excess EDFA gain yields an $SFDR$ = 103±2 dB·Hz$^{2/3}$. (b) Zoomed view of data points and fits.

Next, the single-point and multi-point results are compared by performing the multi-point $SFDR$ assessment for several MZM bias points with a -5 V reverse bias. The resulting

$SFDR$s are then compared to the single-point $SFDR$s for both PN and PiN modulators, Figure 26. The single point $SFDR$s provide reasonable estimation of the multi-point $SFDR$s; errors result from the deviation of multi-point extrapolations of fundamental and IMD3 data away from the ideal values of one and three, respectively.

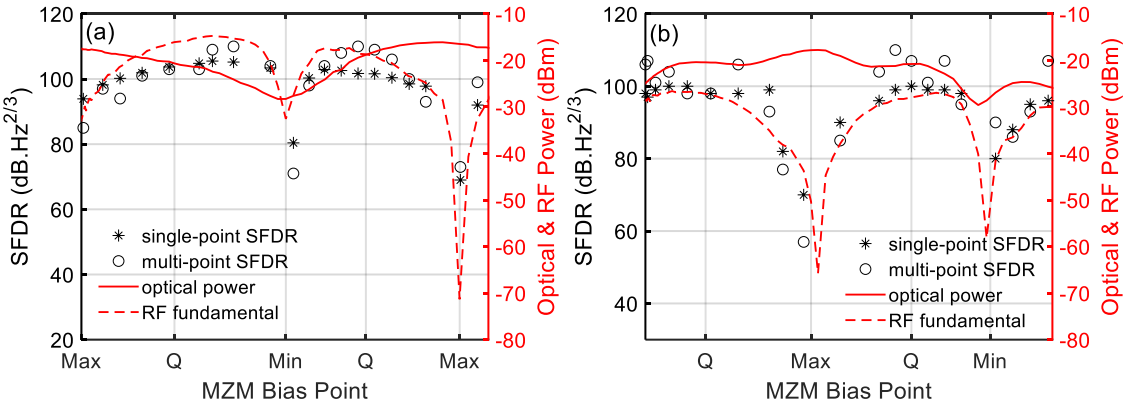

Figure 26 – Comparison of $SFDR$ from the single RF input power (single-point) two-tone measurement and multi-point measurement versus MZM bias point for a fixed reverse bias on both phase modulators of -5 V. Optical power and fundamental RF power are also shown for reference. (a) the PN MZM and (b) the PiN MZM. Input RF power is +4 dBm for all measurements.

Lastly, the PN and PiN modulator RF performance metrics, including bandwidths and $IIP3$s are summarized in Table 6. Here, only the $IIP3$ is cited for quantifying device linearity, since $OIP3$ and $SFDR$ depend heavily on the link parameters and other components.

Table 6– Summary of SiP Modulator RF Performance.

METRICS	PiN MZM	PN MZM
3 dB Electrical-Electrical Bandwidth (GHz)	12.9±0.5	10.9±0.5
3dB Electrical-Optical Bandwidth (GHz)	> 20	> 20
IIP3 (dBm)	+24±1	+23±1

Here, the DC Kerr effect and plasma-dispersion effects were judiciously combined along with an appropriate bias point to linearize the SiP MZM transfer function and hence optimize the link $SFDR$. Additionally, this work highlights the importance of including the DC Kerr effect in the simulation and characterization of SiP modulators at higher reverse biases due to silicon's large $\chi^{(3)}$. Comments on the power consumption of using DC Kerr effects are included later section 6.4.5.

6.4 **Pure DC Kerr Effect Modulators**

Silicon has emerged as a leading optical material despite silicon's indirect bandgap and centrosymmetry that intrinsically prohibit optical gain and the Pockels effect, respectively. To achieve optical gain and a practical Pockels effect on silicon – while maintaining compatibility with CMOS processes – is the holy grail of silicon photonics and would enable a new generation of SiP circuitry. The former would greatly improve power budgets, ease optical packaging, and reduce cost, while a SiP Pockels effect would forego the need for heterogeneous modulators, reduce cost, and enable highly linear all-silicon photonic integrated circuits (PICs). Herein, the potential of using the DC Kerr effect, a demonstrated phenomenon in SiP modulators [62-63], as a *synthetic Pockels effect* for optical modulation is investigated. This terminology is used to distinguish this electric-field induced Pockels effect from *mechanically strained* Pockels effects in silicon [64]. Based on underlying validated DC Kerr effect theory [59, 62], here simple expressions for the basic figures of merit (FOMs) for synthetic Pockels effect silicon modulators are presented along with characterization of a fabricated DC Kerr effect modulator. Through simulations, the modulator efficiency is optimized as a function of the effective electrode spacing. Using the optimized phase shifter design, the tradeoff in modulation bandwidth associated with

using resonant enhancement of the modulation efficiency is explored. Finally, an analysis of the likely usage scenarios for these synthetic Pockels effect modulators is presented and compared to existing state-of-the-art SiP modulation methods.

To clarify the behavior of the DC Kerr effect as a synthetic Pockels effect, the index response equations are cast into an *effective* linear electro-optic coefficient r_{eo} and an *effective* $\chi^{(2)}$ nonlinearity, $\chi^{(2)}_{eff}$:

$$\chi^{(2)}_{eff} = 6\chi^{(3)}E_{DC} \tag{6-8}$$

$$r_{eo} = -\frac{2\chi^{(2)}}{n_i^4} = -\frac{12E_{DC}\chi^{(3)}}{n_{Si}^4} \tag{6-9}$$

In the above two expressions, E_{DC} is the applied DC electric field across the waveguide to induce the synthetic Pockels effect. The $\chi^{(2)}_{eff}$ and effective r_{eo} are shown versus E_{DC} in Figure 27, up to a maximum bias field equal to silicon's breakdown electric field of $3\text{x}10^5$ V/cm. The $\chi^{(3)}$ value of silicon used in this work is $2.45\text{x}10^{-19}$ m^2/V [57]. The maximum effective r_{eo} and $\chi^{(2)}$ achievable before the field breakdown of silicon are 0.6 pm/V and 44.1 pm/V. With these parameters, a direct comparison to lithium niobate and other Pockels materials is possible. Notably, the index of refraction (and thus the optical phase) can be near perfectly linearly modulated with an AC voltage, just as in natural Pockels materials.

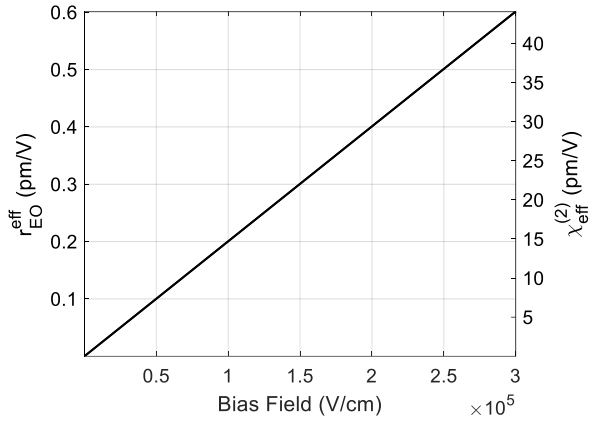

Figure 27 – (a) Calculated r_{eo} (left axis) and $\chi_{eff}^{(2)}$ (right axis) as functions of the applied DC bias field.

6.4.1 DC Performance

The first FOM to quantify is the absorption and efficiency (per unit length) of the synthetic Pockels effect in silicon to shift the optical phase. When assessing the potential performance of a modulator based on the synthetic Pockels effect, a reasonable (and easily fabricated) design is assumed. The general design of the phase shifter looks quite similar to most pn junction based SiP phase shifters: metal electrodes connect electrically to highly doped silicon regions to concentrate the voltage over a small region containing the optical mode. However, in contrast to plasma-dispersion modulators, a pure synthetic Pockels effect modulator should not have significant dopants in the waveguide region for three reasons: 1) the dopants in the waveguide will cause unintended phase shifting from the plasma-dispersion effect; 2) the dopants will increase the insertion loss, and 3) the pn junction will increase the capacitance of the device and reduce bandwidth. The $V_\pi L$ for a pure DC Kerr effect (synthetic Pockels effect) phase modulator is written as

$$V_\pi L = \frac{\lambda n_{Si} d}{12 E_{DC} \chi^{(3)} \Gamma}. \qquad 6\text{-}10$$

Here, L is the active length of the phase shifter, d is the effective electrode spacing (the distance between the n++ and p++ doped regions), λ is the optical wavelength and Γ is the overlap factor between the applied electric field and the optical mode. The overlap factor Γ is best simulated via Lumerical or other commercial tools, and its value was simulated as a function of the electrode spacing d. This $V_\pi L$ expression provides a convenient means for calculating the phase shifting efficiency and mimics the same form of the expression for a Pockels effect modulator.

The insertion loss for the phase shifter is calculated through finite-element mesh simulations using Lumerical DEVICE and MODE [60], which directly calculates the absorption α in dB/cm. This α accounts only for free-carrier absorption due to the mode overlap with doped silicon; thus, the calculated α is added to a baseline 2 dB/cm loss commensurate with state-of-the-art waveguide loss dominated by optical scattering. The Lumerical simulations assume a phase shifter cross-section matching custom designed phase shifters using the Globalfoundries 9WG SiP process. Lumerical MODE was also used to calculate the overlap factor Γ. The phase shifter $V_\pi L$ (right axis) and α (left axis) metrics are calculated as functions of electrode spacing d, Figure 28.

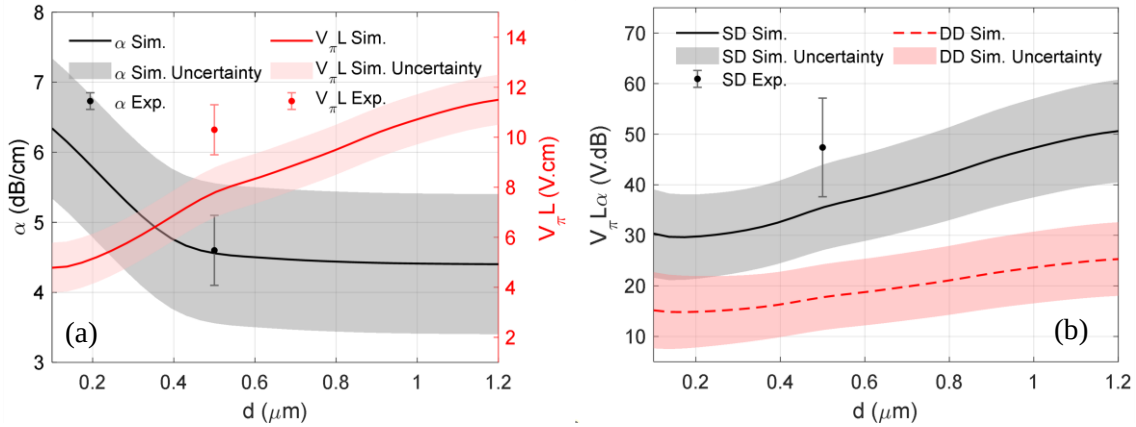

Figure 28 – (a) Calculated absorption in dB/cm (left axis) and $V_\pi L$ in V·cm (right axis) versus effective electrode spacing d for DC Kerr effect phase modulators. (b) Calculated $V_\pi L\alpha$ products for phase modulators (or single-drive MZMs) in solid lines and dual-drive MZMs in dashed lines versus the effective electrode spacing d on the x-axis. Interestingly, there is a clear optimum for $d \approx 0.19\ \mu m$. This optimum point best balances phase shifting efficiency with insertion loss. Note the α within the product accounts for both scattering loss and free-carrier absorption.

Because a common figure-of-merit also considers the phase shifting efficiency and loss together in a single product, the $V_\pi L\alpha$ product in Figure 28(b) versus d is also calculated. In the same figure, the $V_\pi L\alpha$ product is shown for both a phase modulator or single-drive Mach-Zehnder modulator (MZM) (solid black) and a dual-drive MZM (dashed red), the latter which generally exhibits twice the phase-shifting efficiency as a single phase modulator. Generally, reducing d imparts a benefit in terms of overall efficiency; however, reducing d also incurs a greater amount of plasma-dispersion index response, which may not be desired for linear phase modulation.

The best dual-drive (single-drive) MZM $V_\pi L\alpha$ product calculated was ~15V·dB (~30 V·dB) for d = 0.19 µm. This efficiency-loss product is competitive with reported FOMs of other

plasma-dispersion silicon MZMs, including lateral pn junction MZMs with $V_\pi L\alpha$ = 19.4 V·dB [65] and vertical pn junction modulators with $V_\pi L\alpha$ = 20.0 V·dB [66].

The experimental data points indicated in Figure 28 are from DC experiments performed in section 6.4.4. The experimental α agrees well with theory, and the measured $V_\pi L$ is within the calculated $V_\pi L$ by approximately 20%. The deviation between experiment and theory is amplified in the $V_\pi L\alpha$ metric by the compounded errors of the component $V_\pi L$ and α measurements.

6.4.2 Expectations on AC Performance

In terms of modulation speed, the DC Kerr effect is expected to have fundamental limitations similar to lithium niobate, where the theoretical *material* maximum modulation speed is limited by the speed of the electronic polarizability of the constituent atoms. This leaves practical bandwidth limitations due to RC time constants and group velocity mismatch effects, both of which are specific engineering problems tackled through careful traveling wave electrode and junction design. In terms of RF phase velocity mismatches with optical group delays, lithium niobate modulators enjoy the advantage, as their generally low (~2.2) optical group index generally falls within an easily designable range of RF phase effective indices (2.0 – 2.4). SiP modulators generally have high optical group indices (~4.0) that make matching the electrode's RF phase velocity more difficult. On the other hand, Si/SiO_2 possesses an electric permittivity far lower than the permittivity of lithium niobate. Hence, SiP DC Kerr effect modulators should enjoy advantages of very low capacitance over lithium niobate modulators. Of course, adding dopants in the waveguide for plasma-dispersion based SiP modulators adds further capacitance. Thus, the

practical upper limit of the DC Kerr effect modulator will likely be more competitive with lithium niobate modulators when in an RC-limited bandwidth regime, rather than in an index mismatch regime. As integrated lithium niobate modulators have demonstrated bandwidths >100 GHz [67], similarly wide bandwidths may be achievable with silicon synthetic Pockels effect modulators.

6.4.3 Resonant Enhancement

Here, the pros and cons of using the synthetic Pockels effect in silicon to modulate within a resonant cavity, such as a ring resonator, are assessed. Resonant enhancement has demonstrated clear benefits in modulation efficiency, which is the largest hurdle for practical use of the DC Kerr effect for modulation. The main tradeoff for enhanced efficiency is a reduction of the modulation bandwidth. The balance between efficiency and modulation bandwidth will determine the modulator's application as either a low-speed tuning device or a high-speed modulator.

A useful way to assess the efficiency of a ring enhanced modulator is to develop an equivalent V_π. As found in [68], the equivalent V_π for a phase modulator inside a resonant cavity is

$$V_\pi^{eq} = \frac{\pi}{2}\left(\left|\frac{dT}{dV}\right|_{max}\right)^{-1} = \frac{\pi}{2}\left(\left|\frac{dT}{d\Theta}\frac{d\Theta}{dV}\right|_{max}\right)^{-1} = \frac{V_\pi}{2}\left(\left|\frac{dT}{d\Theta}\right|_{max}\right)^{-1} \qquad 6\text{-}11$$

where dT/dV is the sensitivity of the transmission amplitude to voltage, $d\Theta/dV$ is the sensitivity of the phase to voltage, and $dT/d\Theta$ is the sensitivity of the transmission amplitude to phase. The final expression shows a separation of the inherent phase shifter's V_π and a resonant enhancement factor (G_R):

$$G_R = \frac{1}{2}\left(\left|\frac{dT}{d\Theta}\right|_{max}\right)^{-1} \qquad 6\text{-}12$$

Unfortunately, the enhancement factor does not yield a convenient analytic expression; thus, it is best calculated numerically. Here, the resonant enhancement factor for a ring as a function of its coupling factor r and loss factor a (where a = 1 is lossless) is calculated; contours showing the ring's finesse and extinction ratio were also calculated to indicate the ring characteristics. Calculations were done in three steps: 1) by calculating the first and second derivatives of the ring transfer function and 2) by numerically solving for the roots of the second derivative to find the maximum slope along the transfer function, and 3) evaluating the first derivative of the transfer function at the roots. See Figure 29(a).

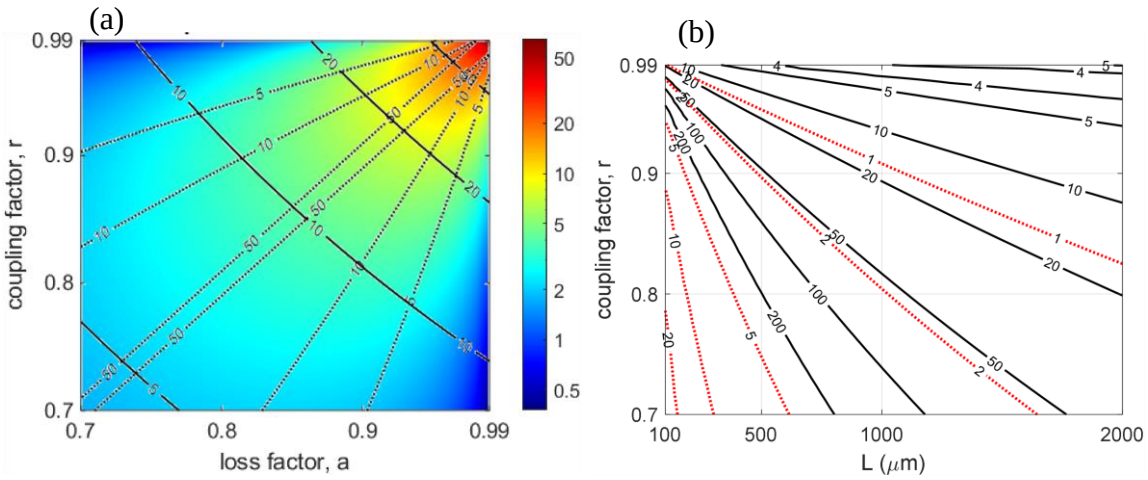

Figure 29 – (a) Calculated efficiency enhancement factor (colored axis), which indicates the reduction of the intrinsic phase shifter V_π due to resonant enhancement for a ring resonator with coupling factor r and loss factor a. Contours of the ring's finesse (solid lines) and extinction ratio (dashed lines) are also plotted. The enhancement factor calculations assume a fixed active electrode length. (b) Calculated contours of V_π^{eq} (black, solid) and 3 dB bandwidth (red, dotted) over the space consisting of reasonable coupling factors r and electrode lengths L. These calculations used the optimal electrode spacing d and corresponding loss factor a (related to α) determined for lowest $V_\pi L\alpha$ in Figure 28(b).

Next, the tradeoff of the ring modulator efficiency and bandwidth is considered. First, an optimal phase shifter design is chosen based on the results of Figure 28 Figure 28.

Figure 28, which indicates d = 0.19 μm to exhibit optimal efficiency-loss characteristics. This choice of specific phase shift design sets the loss factor a. Thus, the only major design parameters left to consider are the coupling factor r (a function of the coupling gap) and the phase shifter length L. Following the approach in [69], the photon lifetime limiting the ring modulator bandwidth is given by

$$\tau_p = \frac{n_g L}{2\pi c} F = \frac{n_g L}{2c} \frac{\sqrt{ra}}{1 - ra} \qquad 6\text{-}13$$

Where F is the ring resonator finesse [70], n_g is the optical group index, and c is the speed of light in vacuum. This photon lifetime yields an upper limit on the ring modulator 3 dB bandwidth [69] of

$$f_{3dB} = \frac{\sqrt{\sqrt{2} - 1}}{4\pi\tau_p} \qquad 6\text{-}14$$

Using this expression for bandwidth and previous expressions for V_π^{eq}, contours of bandwidth and V_π are calculated over the design space of reasonable values for the coupling factor r and the phase shifter length L, Figure 29(b).

From the results of Figure 29(b), resonant enhancement is only suitable for low bandwidth modulation, as the voltage requirements become far too large for high-speed modulation. High speed modulation applications will thus best use Mach-Zehnder modulators along with careful traveling wave electrode design and longer electrode lengths.

6.4.4 Experiments

To verify some of the major results of this work, custom MZMs were fabricated using Globalfoundries 9WG (90 nm) electronic-photonic SOI process. An MZM with 2.4 mm long phase shifters comprised of PIN junctions with an intended intrinsic region 500 nm wide was designed, fabricated, and tested. The design minimizes plasma-dispersion effects while still enabling a strong electric field to be applied transverse to the direction of propagation of a TE wave through the waveguide, enabling strong DC Kerr effects to be observed.

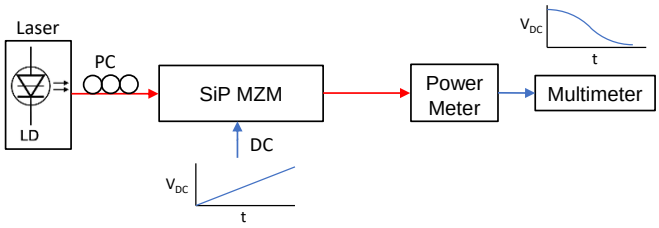

Figure 30 – Schematic of the experimental setup for DC characterization of the pure DC Kerr effect modulator.

The DC transfer function of the MZM was measured by sweeping the voltage applied to one arm of the MZM while ground the phase shifter electrodes on the second MZM arm. The optical response was captured by a power meter, and a multimeter recorded the response in terms of voltage, Figure 30. The measurement was then repeated for using the second optical output of the MZM to obtain two transfer functions corresponding to two outputs of the MZM's output 2x2 directional coupler. This method, used in [62], enables the unambiguous extraction of both the index (or phase) and absorption responses of the MZM's phase shifter, Figure 31.

The experimental index response of Figure 31 indicates a clear DC Kerr effect dominated response, as the curvature is negative due to the square dependence of the index on the electric field. Typically, a plasma-dispersion response exhibits a positive curvature. Simulations can determine reasonable estimates for the contributions of the DC Kerr effect and plasma-dispersion effects to the total index response.

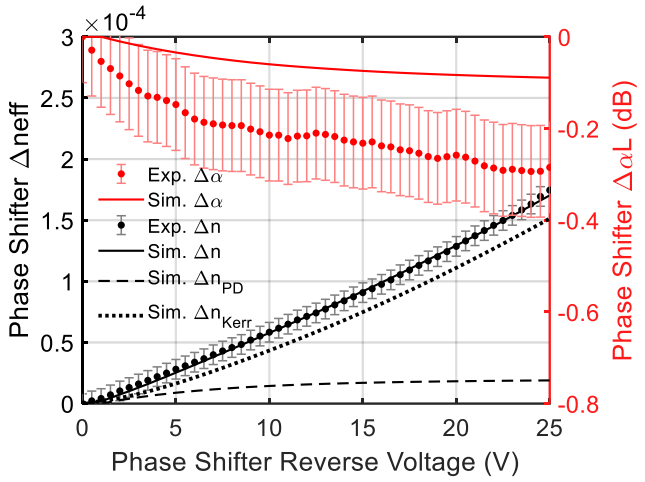

Figure 31 – Experimental extraction of the index (left axis) and absorption (right axis) responses. The total simulated index response, comprised of plasma-dispersion and DC Kerr contributions, matches well with the experimentally extracted index response. The simulated absorption response is also shown alongside its experimental counterpart.

Using Lumerical DEVICE to simulate the carrier concentrations in response to an electric field and Lumerical MODE to calculate the optical mode and index response resultant from the carrier concentrations, the simulated plasma-dispersion response was obtained, Figure 31. To include DC Kerr effects, the applied electric field distributions were calculated by Lumerical DEVICE, and the DC Kerr effect theory of section 6.2 was used to obtain the material index response. Following, the overlap integral between the optical and applied electric fields was calculated to yield the effective index response due to the DC Kerr effect. The total index response is the sum of the plasma-dispersion and DC Kerr index responses.

Figure 31 shows excellent matching between simulated and experimental index responses. The absorption response, due entirely to plasma-dispersion, was simultaneously calculated by Lumerical DEVICE and shows reasonable agreement with experiment. Dopant concentrations were assumed within typical ranges and found to provide good fits to the data for n and p concentrations in the low 10^{17} cm^{-3}. Generally, the choice of different dopant concentrations cannot achieve similar index responses to the experiment. While small (<10%) tradeoffs in n and p dopant concentrations can still maintain a relatively good fit to the index response, such new concentrations cannot achieve a totally different total index response that would lead to vastly different conclusions. Furthermore, the shape of the experimental curve can only be achieved with significant DC Kerr effects present and cannot be explained by purely plasma-dispersion effects.

Next, the gain of the link is measured as a function of the reverse bias. This experiment is performed to confirm the behavior of the DC+AC modulation response described in section 6.2, which until now, has never been experimentally confirmed in the literature, to the authors' best knowledge. The DC+AC modulation response, $\Delta n_{AC} \propto E_{DC}E_{AC}$, indicates that the index response is linearly proportional to the applied DC electric field. The experiment is not as straightforward as it initially appears, because the bias point of the modulator will also shift with index modulation following a quadratic response, as observed when measuring the MZM transfer function. Thus, for the AC experiment, the reverse bias is applied to both arms to not perturb the bias point, while a single arm is driven with the RF signal. Thus, the gain of the link vs. reverse bias is measured while accounting only for the increased modulation efficiency from the DC Kerr effect according to $\Delta n_{AC} \propto E_{DC}E_{AC}$. The experimental setup is given in Figure 32, and the results are shown

in Figure 33(a) along with the calculated gain response. Good accuracy in magnitude is confirmed along with generally similar curvature. The experimental curve appears flatter than in theory, indicating a truly sub-linear index response due to other junction effects. Depletion width modulation was accounted for according to basic semiconductor equations in the calculated curve of Figure 33(a). Comparison is highlighted over the range of reverse biases greater than 10 V to avoid any forward bias effects and because the gain is very small below 10 V reverse bias, such that small plasma-dispersion effects may dominate the response.

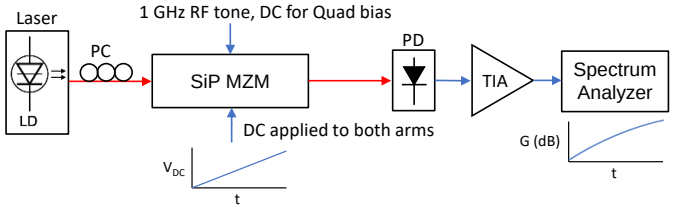

Figure 32– Schematics of experimental setups for AC characterization.

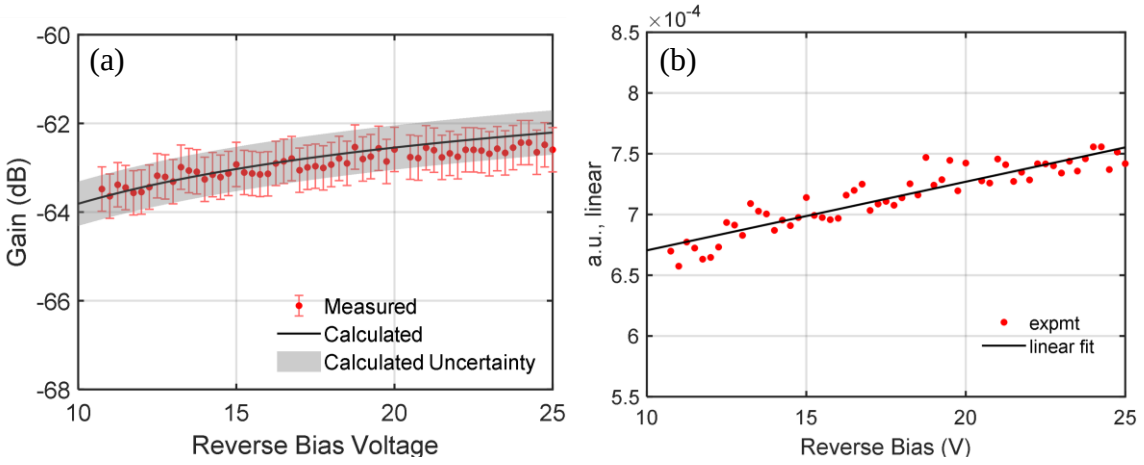

Figure 33 –(a) Experimental RF gain vs. reverse bias for a 1 GHz tone and calculated gain curve based on analog link gain (Eq. 3-1) and a simulated depletion width (a function of reverse bias) using Lumerical DEVICE. (b) $\sqrt{g} \propto V_{out}$ where g = gain in arbitrary linear units vs. reverse bias, demonstrating the linearity of AC modulation of synthetic Pockels effect as compared to a linear fit of the data. The experimental data is not perfectly linear since there is still residual depletion width modulation with increasing reverse bias.

Next, the linearity of the gain response is assessed qualitatively in relation to an ideal linear fit of the data, Figure 33(b). A decibel form of Eq. 3-1 is

$$G[dB] = -22.1 + 20\log_{10} I_{DC}[mA] - 20\log_{10} V_{\pi}[V] \qquad 6\text{-}15$$

Inserting the DC Kerr V_{π} expression from Eq. 6-10 and assuming $E_{DC} \approx \frac{V_{DC}}{d}$ yields

$$G_{DC\,Kerr}[dB] = -22.1 + 20\log_{10} I_{DC}[mA] - 20\log_{10} \frac{\lambda n_{Si} d^2}{12 V_{DC} L \chi^{(3)} \Gamma}[V] \qquad 6\text{-}16$$

From this expression, the gain $G_{DC\,Kerr}$ is a function of $+20\log_{10} V_{DC}$; hence, on a linear scale, $g_{DC\,Kerr} \propto V_{DC}^2$. Therefore in Figure 33(b), $\sqrt{g_{DC\,Kerr}}$ vs. V_{DC} is compared to a linear fit of the data to demonstrate the relative linearity of the AC modulation response of the synthetic Pockels effect. The measured data is not perfectly linear since residual depletion width modulation persists with increasing reverse bias, yielding a slightly sublinear response.

6.4.5 Applications of the Synthetic Pockels Modulator

Here, the DC Kerr effect was cast into an effective synthetic Pockels effect, through both an effective linear electro-optic coefficient r_{eo} and a $\chi_{eff}^{(2)}$, both dependent on the DC electric field strength. The performance of a proposed modulator based solely on the DC Kerr effect (a synthetic Pockels effect) was investigated in terms of modulation efficiency, loss, and bandwidth for standalone phase shifters, Mach-Zehnder modulators, and ring implementations. There are several strengths of the pure DC Kerr effect for modulation: 1) highly linear phase responses, 2) large modulation bandwidths due to low junction

capacitance and freedom from moving large electron/hole concentrations, 3) pure phase modulation and negligible amplitude modulation in phase shifters, 4) relative inertness to temperature and radiation effects. The strengths and weaknesses of the synthetic Pockels effect in Si is compared to state-of-the-art SiP plasma-dispersion, InP, and $LiNbO_3$ phase shifters in Table 7.

Table 7– Comparison of Common Phase Shifter Technologies

Phase Shifter Type	$V_\pi L\alpha$ **(V·dB)**	**Strengths**	**Weaknesses**
SiP / plasma-dispersion	19	Compact, moderate V_π, cost of integration	Loss, bandwidth
SiP / DC Kerr	30	Low loss, linear, bandwidth, cost of integration	$V_\pi L$, phase shifter length
$LiNbO_3$	6	Low $V_\pi L$, low loss, linear, bandwidth	Cost of hybrid integration
InP	20	Compact, moderate V_π, cost of integration, optical gain	Bandwidth, noise

However, using the synthetic Pockels effect for modulation poses a few challenges: 1) the requirement for large reverse biases, typically 5-12 V_{DC}, 2) relatively high current draw through resistive terminations and subsequent high DC power consumption, 3) modulation efficiency, i.e. the V_π. Of these drawbacks, the first drawback is mitigated through judicious junction design to reduce the required reverse bias voltages; practically, this is done by reducing the effective electrode spacing d. Generally, junctions that exhibit low breakdown voltages will similarly require low reverse biases to manifest strong DC Kerr effects. The large current draw derived from the reverse bias voltage difference over the modulator termination resistance (typically 35-50 Ω) may be solved by using capacitive terminations. When such capacitive terminations are implemented, the electrical power consumption

difference between SiP plasma-dispersion, SiP DC Kerr effect, InP, and $LiNbO_3$ is determined by the signal power required for driving the modulator. As $LiNbO_3$ modulators generally exhibit the best $V_\pi s$ in the range of 1V to 5 V, these will consume the least power. On the other hand, a SiP plasma-dispersion modulator with a typical V_π in the range of 4V to 8 V, will require a drive voltage proportionately larger in comparison with $LiNbO_3$, Fortunately, linearization by DC Kerr effect costs very little extra power, as the strong DC field draws low current (<1 μA) if capacitive terminations are used. When capacitive terminations are used, the current is primarily drawn across the PiN junction. A pure DC Kerr effect modulator will similarly only require more electrical power insofar as the higher V_π requires a higher drive voltage.

These strengths and challenges to synthetic Pockels modulators indicate three main applications areas of interest: microwave photonics, digital transmitters, and computing. The DC Kerr modulator's high linearity and large expected bandwidths could greatly benefits microwave photonic deployments, including phased arrays, next-gen fronthaul links, intra-vehicular RF photonic links, and frequency converting systems. Further, the DC Kerr effect's relative resilience to temperature and radiation effects bodes well for airborne and spaceborne photonic communication systems. Digital transmitters using high order modulation formats may similarly find benefit from the DC Kerr effect modulator's inherent linearity and high-speed modulation characteristics. Lastly, the modulator's pure phase modulation makes it a great candidate for use in quantum gates, while its relative resilience in temperature swings (due to its lack of need for carrier density perturbations) lends itself well to low temperature computing applications. In fact, the DC Kerr effect has been shown to operate more efficiently at 5 K compared to room temperature [71].

Future work should pursue further optimization of the DC Kerr effect modulator through optimizing the PiN junction design, investigating pure metal electrode stacks, engineering high breakdown field junctions, and implementing push-pull (dual-drive) MZM schemes.

CHAPTER 7. PHOTONIC FREQUENCY CONVERSION & DESIGN EQUATIONS

7.1 Photonic Frequency Converters in the Literature

Frequency converters, also known as mixers, translate information to a new frequency, a function required in many communications systems and applications, including phased arrays, next-gen fronthaul links, intra-vehicular communications, inter- and intra-satellite communications, antenna remoting, metrology, test and measurement, and more. These applications leverage microwave photonics' strengths in low loss transmission of RF signals, large optical bandwidths, increased immunity to electromagnetic interference, ability to reduce usage of bulky RF cables, high linearity over wide bands, and good isolation between electrical signals. Frequency conversion includes frequency translations to higher frequencies (upconversion) and to lower frequencies (downconversion).

A mixer requires a nonlinear mechanism. In electronic mixers, the nonlinear mechanism is provided by the transistor. In photonic mixers, the nonlinear mechanism is typically provided by the square law behavior of the photodetector. However, other nonlinear mechanisms for mixing have been reported, such as the use of high Q optomechanical oscillations [72].

Focusing on methods using the detector as the nonlinear element, photonic frequency converters mix two optical signals: 1) the RF-modulated optical sideband and 2) the local oscillator (LO). For optical LO's, the LO wavelength is simply tuned relative to the RF-modulated optical sideband to upconvert or downconvert at the photodetector. For an electrical LO, an electro-optic modulator transduces the oscillator signal onto the same optical carrier that the RF data is modulated upon. In the optical frequency domain,

modulation generates sidebands on either side of the optical carrier, with amplitude and phase dependent on the type of modulation (e.g. phase or amplitude modulation) and the bias point. In photonic mixing using an electronic LO, the relative frequency offset between the LO-generated and RF-generated sidebands determines the final frequency of the RF data. This new frequency is called the intermediate frequency (IF) in most applications, and its power is a function of RF, LO, and optical powers. Hence, achieving high RF-to-IF mixing gain requires sufficient optical and LO power.

Photonic mixing has advantages over electronic mixers in instantaneous bandwidth, broadband linearity, and immunity to electromagnetic interference. Photonic mixers are also naturally compatible with existing fiber-optic links for efficient RF transport. Typically, such RF photonic links are single wavelength systems spanning anywhere from a few meters (e.g. for airborne platform signal routing and processing) up to a 10s of kilometers (e.g. for radioastronomy and remote antenna signal routing and processing).

Photonic mixing is not a new subject and has benefited from more than two decades of research and has leveraged high quality discrete components [73-75]. Several mixer architectures have been reported over the years. High dynamic range methods include amplitude or phase modulation of two modulators in series (one for the RF, the second for the LO) [76-78]; however, these methods demonstrated reduced performance beyond 10 GHz. The main weakness of series modulator implementations is a multiplicative behavior that inherently inhibits linearity; modulation by the second modulator will create sidebands on either side of any existing optical sidebands. Other methods, as mentioned, use a second laser for the LO along with an optical phase-locked loop (OPLL) [79, 80]; unfortunately, the phase noise of the lasers and the OPLL's bandwidth limitations increase the system's overall phase noise [81]. Narrowband optical filtering via fiber Bragg gratings lower the system phase noise [73, 82, 83]. Another approach uses phase modulators within a Sagnac interferometer to suppress the carrier and attain high conversion efficiency [84].

A common frequency conversion architecture uses a single laser source along with two modulators nested in parallel within a larger Mach-Zehnder interferometer. This results in a highly linear architecture whereby the LO-generated sidebands and RF-generated sidebands add optically before photodetection. This architecture also naturally enables balanced photodetection by using a directional coupler to close the larger MZI after modulation. As measured in intensity-modulated, direct-detect (IMDD) fiber links, balanced detection has demonstrated dramatically reduced noise power spectral densities (i.e. "noise floors") to enable higher dynamic range and reduced noise figures [85]. Balanced detection reduces common-mode noise, such as laser and optical amplifier noise added before modulation. Electrical noise and shot noise are not common-mode and thus are not reduced significantly by balanced detection.

However, few have reported fully *integrated* photonic mixers. Moreover, among those reporting the use of any integrated components, most demonstrations only integrated a single component of the mixing architectures [53, 86-88]. For example, in [53, 86-87], only the modulators were integrated as part of a larger frequency converter architecture. Likewise [88] integrated the optical filter but not the modulators nor detectors. Integrated photonic mixers by S. Jin et al. have demonstrated the highest levels of integration in InP [10, 11, 89] to date along with the SiP work of Chapter 8. S. Jin's result from [89] integrated the laser as well (given the InP platform) and achieved a $SFDR$ of 112 dB·Hz$^{2/3}$, though with very limited (250 MHz) bandwidth. Together the works of Jin *et al*. and the work presented in Chapters 8-9 exemplify the current state-of-the-art in integrated photonic mixers. Figure 34 summarizes the evolution of integrated frequency converter work over the past decade.

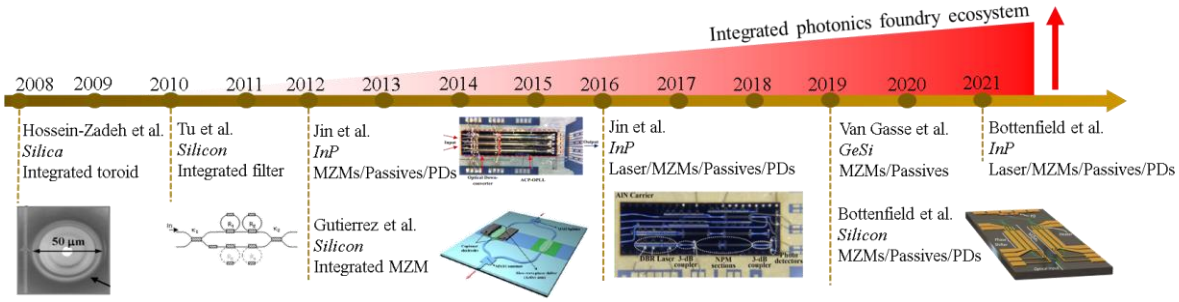

Figure 34 – Timeline highlighting the major integrated photonic mixers reported in the literature. The material systems on which frequency converters have been demonstrated here include silica, silicon-on-insulator, GeSi, and InP. Over the past decade, the integrated photonics foundry ecosystem has emerged and enabled full integration of frequency converters.

Initial target metrics for the adoption of integrated photonic mixers into phased array antennas (for example) include greater than 100 dB·Hz$^{2/3}$, 10s of GHz wide instantaneous bandwidths, and noise figures comparable to those of discrete mixers (<20 dB). To date, no single integrated photonic mixer has achieved all these metrics simultaneously, nor even two simultaneously. Later in this work, the architectures and device-level performance required to achieve this are identified.

This chapter introduces frequency converter operation and design equations, detailing the main component metrics desired for high performance frequency converter systems.

Chapter 8 demonstrates through experiment and calibrated simulations that state-of-the-art implementations of silicon photonic (SiP) IMWP mixers can achieve the performance required by most applications. The first silicon frequency converter with electrical RF-to-IF conversion completely on-chip is also demonstrated. As of this writing, the frequency converter presented in Chapter 8 demonstrates the widest RF bandwidth of any fully integrated frequency converter on any material platform.

Chapter 9 demonstrates a high-performance frequency converter using Infinera's InP platform, exhibiting $SFDR$s > 100 dB·Hz$^{2/3}$ and gains approaching unity.

7.2 Photonic Frequency Converter Operating Principles

Photonic frequency converters, like their electronic counterparts, require a nonlinear component to perform the mixing function. In electronics, this nonlinear component is a transistor operated in a nonlinear regime; similarly, the photonic mixing element is most commonly a diode – a photodiode. In fact, virtually all ordinary operation of photodiodes leverages its frequency mixing properties. In RF photonic links, for example the fundamental electrical signal is produced by the beating of the RF-generated optical sideband and the optical carrier. Even the DC photocurrent can be understood as the self-beating of the optical carrier with itself. The generated photocurrent is $I(t) = RP_0$, where R is the responsivity. P_0 is the average optical power given by

$$P_0 = \frac{A}{2}\left(\frac{\epsilon}{\mu}\right)^{1/2} E_{opt}E_{opt}^*, \qquad 7\text{-}1$$

where A is the fiber core or waveguide cross-sectional area; ϵ is the electric permittivity; μ is the magnetic permeability; and E_{opt} is the optical electric field just before photodetection. Hence, the generated photocurrent is linear with average optical power, but the generated electrical signal power is quadratic. This square-law behavior of the photodetector is what enables the mixing of various optical signals. In photonic frequency converters, the mixed optical signals are typically 1) the RF signal modulated onto an optical carrier, and 2) a local oscillator (LO). This LO may be generated by the same or another laser (as that serving the RF modulation), or by an electrical source modulated onto an optical carrier. The new electrical carrier frequency generated at the photodetector is

called the intermediate frequency (IF). The IF power scales favorably with RF, LO, and optical powers provided linearity of the system is maintained.

The following Chapters 7-9 will focus on photonic frequency converters employing electrical LO's that drive an optical modulator. The operation of these frequency converters works generally as follows, per Figure 35. A laser's output power is split evenly, with half the optical power modulated by the RF signal at frequency f_{RF} and the other half modulated by the electrical LO (by a separate modulator in parallel) at frequency f_{LO}. The RF modulator transduces the RF signal onto the optical carrier at optical frequency f_c. The frequency content of the RF modulator output contains residual carrier power at f_c plus the RF data modulated onto new optical carriers at $f_c \pm f_{RF}$, $f_c \pm 2f_{RF}$, $f_c \pm 3f_{RF}$, ... depending on the type and bias point of the modulator employed. Likewise, the LO modulator outputs f_c, $f_c \pm f_{LO}$, $f_c \pm 2f_{LO}$, $f_c \pm 3f_{LO}$, ... The optical modulated outputs are then added and the sum optical power is photodetected, generating a DC current, the fundamental signals and their harmonics, and beat (sum and difference) frequencies. Typically, an electrical filter is employed to isolate the desired IF ($f_{RF} \pm f_{LO}$) from other frequencies generated by the photodetector. The schematic of Figure 35 supposes a downconverting function, whereby $f_{IF} = f_{RF} - f_{Lo}$; hence, a low-pass filter (LPF) is indicated to isolate the IF from other generated frequencies. The IF is set by the proximity of the RF-generated and LO-generated optical sidebands. When using a single laser source for both RF and LO modulators, $f_{IF} = f_{RF} - f_{LO}$ (assuming $f_{RF} > f_{LO}$). However, if the two modulators employ different optical sources, the relative frequencies of the two lasers will also determine the IF.

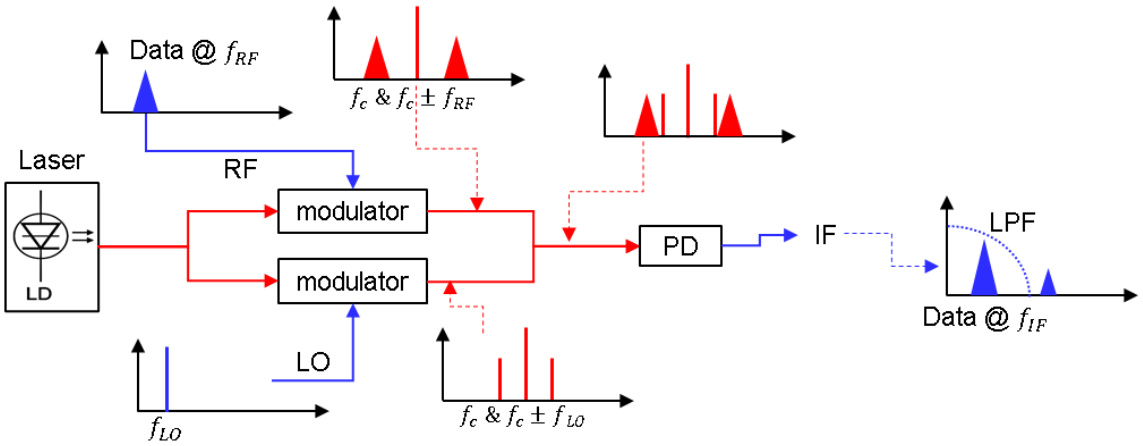

Figure 35 – Schematic of a commonly employed photonic frequency converter using electrical LO source and dual parallel modulators fed by a single laser. Blue indicates electrical signals or connections, and red indicates optical signals or connections.

7.3 Design Equations

In this section, the key MWP metrics for several variants of dual-parallel MZM based photonic frequency converter architectures are derived and used to study performance trends.

7.3.1 Frequency Converter Architectures

The photonic frequency converters described here are all dual-parallel MZM-based architectures with combinations of single or dual-drive MZM operation and single or balanced detection schemes, Figure 36. The dual-parallel MZM architectures are the most common photonic frequency conversion architectures due to their high linearity, wide tunability, and ability to mitigate common-mode noise originating before the modulation stages, such as laser noise. Architectures like those in Figure 36 have been demonstrated numerously in the literature in both discrete [75, 80, 84] and integrated platforms [10, 11, 23, 87, 89-91]; Chapters 8 and 9 characterize SiP and InP implementations, respectively.

All the architectural variants of Figure 36 use a single laser source, coupled via a 2x2 splitter to a macro-interferometer consisting of an RF branch and an LO branch, each which identically consists of an MZM, optical amplifier, and DC phase shifter. The RF and LO branches are recombined by a 2x2 combiner, where the signal is photodetected and converted back to the electrical domain.

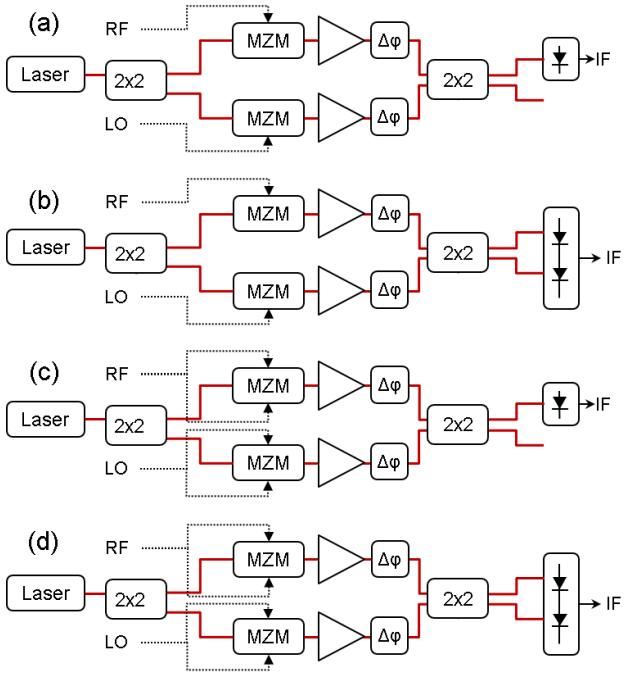

Figure 36 – Schematics of frequency converting architectures investigated, which are differentiated by the drive and detection configurations: (a) single-drive, single detection, (b) single-drive, balanced detection, (c) dual-drive, single detection, and (d) dual-drive, balanced detection.

The equations derived here are flexible beyond their applicability to the four architectural variants of Figure 36. For example, the optical amplifiers and their impact on system performance can also be treated as excess optical loss or ignored altogether. Likewise, the DC phase shifters may be implemented in a variety of ways, since the derived equations only consider the relative phase between the RF and LO branches. Hence, whether there is

a DC phase shifter in the top or bottom branch – or both – is irrelevant so long as the relative phase is referenced in the equations. Still further, the order of components within the macro-interferometer branches may be reconfigured as desired. Lastly, the 2x2 couplers may be replaced with Y-branch couplers without reducing the validity of the equations except for a simple replacement of the relative phase between RF and LO branches $\Delta\phi_{int}$ with $\Delta\phi_{int} - \frac{\pi}{2}$.

Throughout this work, *single-drive* modulation is defined as the application of a single voltage source over one arm of an MZM, Figure 37(a). On the other hand, *dual-drive* (also called *push-pull*) modulation is defined here as a driving scheme whereby the same voltage is applied equally and oppositely across the MZM arms to drive the modulator differentially, Figure 37(b). In both cases, a single source supplies a voltage of the same magnitude.

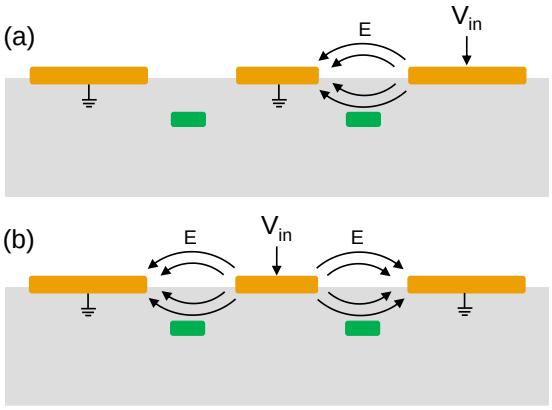

Figure 37 – Schematics defining (a) single drive and (b) dual drive modulator operation.

7.3.2 Derivation of DC Photocurrent and Gain

For brevity, only the single-drive, single detection architecture (Figure 36(a)) equations are derived explicitly here. Sufficient details are given for the reader to independently derive the equations for dual-drive and balanced detection scenarios. Nonetheless, the key metric equations are summarized for all four architectural variants at the end of this subsection. Mathematical notations generally follow the conventions found in [5]. The general derivation strategy is to calculate the electric fields as they propagate through the architecture until they are converted to electrical current and power by the photodetector. Subsequently, the definitions of the metrics covered in Chapter 2 are applied.

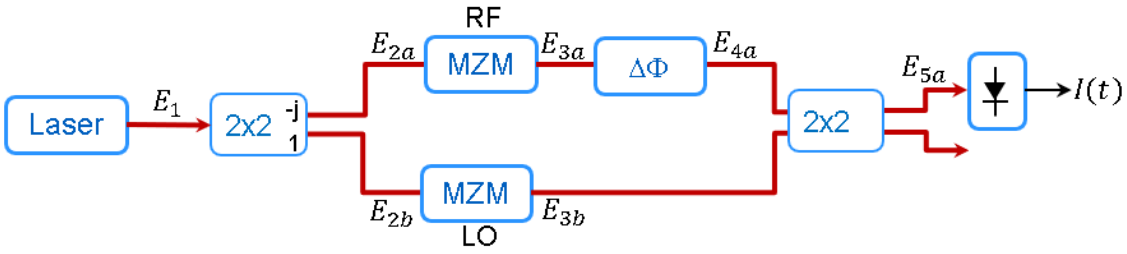

Figure 38 – Schematic of generic photonic frequency converter with electric fields indicated to aid in the derivation of the gain, linearity, and noise metrics.

A schematic with electric fields marked throughout a generic architecture is given in Figure 42 to aid in the derivation. First the laser's output electric field is

$$E_1 = \gamma e^{j\omega t}, \tag{7-2}$$

where ω is the angular optical carrier frequency, t is time, and γ is a constant defined as

$$\gamma = \sqrt{\frac{2g_{opt}P_0}{A_M}}\left(\frac{\mu}{\epsilon}\right)^{1/4}. \qquad 7\text{-}3$$

Here, P_0 is the optical launch power; μ is the magnetic permeability; ϵ is the effective electric permittivity; and A_M is the optical mode area. The parameter g_{opt} is the net optical gain or loss between the laser and the photodetector. When the gain or loss of components in one branch of the macro-interferometer are different than the gain or loss of components in the second branch, the average gain or loss may be used to calculate g_{opt}. For example, for a photonic frequency converter using an RF MZM with 3 dB insertion loss and an LO MZM with 6 dB insertion loss, the loss factor contributing to the g_{opt} factor will be the average of 3 dB (0.5) and 6 dB (0.25) losses on a linear scale, i.e. 0.375 or 4.26 dB effective insertion loss.

The E_1 electric field of the laser output is then split by a 2x2 directional coupler with transfer function

$$\begin{bmatrix} E_{o1} \\ E_{o2} \end{bmatrix} = \frac{1}{\sqrt{2}}\begin{bmatrix} 1 & j \\ j & 1 \end{bmatrix}\begin{bmatrix} E_{i1} \\ E_{i2} \end{bmatrix}. \qquad 7\text{-}4$$

Here, E_{o1} and E_{o2} are the output electric fields of the 2x2 directional coupler for input electric fields E_{i1} and E_{i2}. For these architectures, $E_{i1} = E_1$ is the input field from the laser, and $E_{2i} = 0$. The output electric fields from the directional coupler are thus:

$$E_{2a} = \frac{\gamma}{\sqrt{2}}e^{j\omega t} \qquad 7\text{-}5$$

$$E_{2b} = \frac{j\gamma}{\sqrt{2}} e^{j\omega t} \tag{7-6}$$

Next, E_{2a} propagates through the top branch of the macro-interferometer until it is modulated by the RF MZM. Likewise, E_{2b} propagates through the bottom branch until it undergoes modulation by the LO MZM. The resultant electric fields output by the RF and LO MZMs are (respectively):

$$E_{3a} = \frac{\gamma}{2\sqrt{2}}\, e^{j\omega t}\left(e^{j\phi_{DC}} \sum_{k=-\infty}^{\infty} J_k(A_{RF}) e^{jk\Omega_{RF}t} - 1 \right) \tag{7-7}$$

$$E_{3b} = \frac{j\gamma}{2\sqrt{2}}\, e^{j\omega t}\left(e^{j\phi_{DC}} \sum_{k=-\infty}^{\infty} J_k(A_{LO}) e^{jk\Omega_{LO}t} - 1 \right). \tag{7-8}$$

Here, J_k is the kth order Bessel function of the first kind; ϕ_{DC} is the bias phase of the MZMs; A_{RF} and A_{LO} are the input RF and LO amplitudes; and Ω_{RF} and Ω_{LO} are the RF and LO angular frequencies, treated as single tones here. Later, the RF input is explicitly derived with two RF tones to obtain linearity metrics, which require calculation of intermodulation distortion products (IMDs).

The field E_{3a} is comprised of a residual optical carrier (corresponding to the J_0 and -1 terms) and a theoretically infinite number of RF-generated optical sidebands corresponding to terms J_k with nonzero k. The frequency spectrum is generally symmetric about the carrier frequency, since $|J_k| = |J_{-k}|$. Likewise, the field E_{3b} consists of a residual optical carrier (corresponding to the J_0 and -1 terms) and a series of LO-generated optical sidebands. Although the infinite sums appear to make compact, analytic descriptions of the

frequency converter unlikely, fortunately very few terms contribute to the IF, $\Omega_{IF} = \Omega_{LO} - \Omega_{RF}$. To illustrate this, the kth optical sidebands generated by the RF and LO modulators are at frequencies $\omega + k\Omega_{RF}$ and $\omega + k\Omega_{LO}$, respectively. Upon mixing of these RF- and LO-generated sidebands, a signal at $k\Omega_{LO} - k\Omega_{RF} = k(\Omega_{LO} - \Omega_{RF}) = k\Omega_{IF}$ is produced, which is simply the kth harmonic of the target IF. Hence, the higher order optical sidebands manifest primarily as harmonics of the IF, rather than at the IF. Hence, the infinite sums are truncated to retain only the J_{-1}, J_0, and J_{+1} terms for both RF and LO modulation. The harmonics of the IF are easily suppressed by low-pass filters on the photodetector output for downconversion applications.

When considering linearity metrics, these IF harmonics could interfere with the IF of interest. However, later a small signal approximation is assumed for RF modulation that renders the RF-generated optical signals weak beyond the first or second order. Hence, when the LO-generated optical signals mix with a relatively weak RF-generated optical sideband, the resulting harmonic of the IF will be weak. Furthermore, mixing products such as those between LO-generated optical sidebands (e.g. $\omega + \Omega_{LO}$ and $\omega + 2\Omega_{LO}$) will produce frequencies generally out-of-band, particularly for downconverting applications where $\Omega_{IF} < \Omega_{LO}$ by significant margin. The mixing between LO-generated (or RF-generated) optical sidebands can be a severe problem in photonic upconverters on the other hand; optical filtering must be used to remove undesirable optical sidebands in such situations.

Assuming the DC phase shift $\Delta\phi_{int}$ is applied only to the top branch to set the macro-interferometer bias point, the top field expression simply gains a fixed phase term $e^{j\Delta\phi_{int}}$:

$$E_{4a} = \frac{\gamma}{2\sqrt{2}}\, e^{j\omega t}\, e^{j\Delta\phi_{int}} \left(e^{j\phi_{DC}} \sum_{k=-\infty}^{\infty} J_k(A_{RF}) e^{jk\Omega_{RF}t} - 1 \right) \qquad 7\text{-}9$$

Recall again that whether this $\Delta\phi_{int}$ is physically applied to the top branch, bottom branch, or both differentially is irrelevant, as this $\Delta\phi_{int}$ merely represents the relative phase shift between top and bottom branches. The E_{3b} and E_{4a} fields are then added (with a phase shift) by the 2x2 directional coupler, yielding the electric field incident on the high-speed photodetector:

$$E_{5a} = \frac{\gamma}{4} e^{j\omega t} \Big[e^{j\phi_{DC}} \Big(e^{j\Delta\phi_{int}} J_0(A_{RF}) + e^{j\Delta\phi_{int}} J_1(A_{RF}) \big(e^{j\Omega_{RF}t} - e^{-j\Omega_{RF}t} \big) - J_0(A_{LO}) - J_1(A_{LO}) \big(e^{j\Omega_{LO}t} - e^{-j\Omega_{LO}t} \big) \Big) - e^{j\Delta\phi_{int}} + 1 \Big] \qquad 7\text{-}10$$

The generated photocurrent is a linear function of the incident optical power P_d, equal to $\frac{1}{2} A_M \left(\frac{\epsilon}{\mu}\right)^{1/2} E_{5a} E_{5a}^*$. Hence. The photocurrent is

$$I(t) = RP_d = \frac{R}{2} A_M \left(\frac{\epsilon}{\mu}\right)^{1/2} E_{5a} E_{5a}^* \qquad 7\text{-}11$$

where R is the photodetector responsivity. Because the $E_{5a}E_{5a}^*$ product has many terms, the DC terms and IF terms are focused on separately, beginning with the DC terms.

$$I_{DC} = \frac{R g_{opt} P_0}{16}\Big[J_0^2(A_{RF}) + J_0^2(A_{LO}) + 2J_1^2(A_{RF}) + 2J_1^2(A_{LO}) \\ - 2cos(\Delta\phi_{int})J_0(A_{RF})J_0(A_{LO}) + 2J_0(A_{RF})cos(\phi_{DC} + \Delta\phi_{int}) \\ + 2cos(\phi_{DC} - \Delta\phi_{int})J_0(A_{LO}) \\ - 2\big(J_0(A_{LO}) + J_0(A_{RF})\big)cos(\phi_{DC}) + -2cos(\Delta\phi_{int}) + 2\Big] \quad 7\text{-}12$$

This I_{DC} is a general expression, with virtually no major assumptions made except the effective filtering out of optical sidebands beyond the first order. Here, further assumptions are made to yield simple equations, albeit for more limited use cases. General expressions are revisited in section 7.3.7. Null biased MZMs typically improve performance by minimizing carrier power and hence excess shot noise at the photodetector; hence $\phi_{DC} = 0$. Furthermore, the macro-interferometer bias $\Delta\phi_{int} = 0$ is assumed as this optimizes the system gain, as shown later for the general expressions. Under small signal assumptions for the RF drive condition, i.e. $\frac{V_{RF}}{V_{\pi,RF}} \ll 1$, the Bessel functions with RF arguments are approximated as $J_0(A_{RF}) \approx 1$ and $J_1(A_{RF}) \approx \frac{A_{RF}}{2}$. For LO modulation, a small signal approximation is inappropriate as the optimal LO drive voltage is a significant fraction relative to the LO modulator half-wave voltage, $V_{\pi,LO}$. The analysis proceeds by assuming the optimal drive condition for the LO modulator, since first-order Bessel functions of the first-kind exhibit a global maximum $J_{1,max} \approx 0.5819$ for an input amplitude of $A_{LO} \approx 1.842$. This amplitude is related to the input electrical power by $A_{LO} = \sqrt{\frac{2\pi^2 P_{in,LO} R_{i,LO}}{V_{\pi.LO}^2}}$, where $R_{i,LO}$ and $V_{\pi,LO}$ are the LO modulator input impedance and half-wave voltage, respectively. Optimizing the LO drive voltage is reasonable for modulators with low to

moderate V_π. For example, for $V_\pi = 4$ V the optimal drive voltage has peak amplitude of 2.35 V. With the aforementioned assumptions, the DC photocurrent simplifies to

$$I_{DC} = \frac{R g_{opt} P_0}{16}\left[1.1455 + \frac{\pi^2 P_{in,RF} R_{i,RF}}{V_{\pi.RF}^2}\right]. \qquad 7\text{-}13$$

The first term of the I_{DC} expression corresponds to the self-beating of the LO sidebands at the photodetector, while the second term corresponds to the self-beating of the RF sidebands at the photodetector. Note, there is no DC photocurrent contribution from the self-beating of the optical carrier at the photodetector since the null bias condition is assumed perfect, leaving no optical carrier power at the photodetector. In real implementations, however, the null bias condition will not be perfect due to limited modulator extinction ratio and imperfect bias point precision, resulting in a small contribution of the residual optical carrier power to the DC photocurrent. Nonetheless, as long as the magnitude of the residual optical carrier remains small compared to the magnitudes of the LO generated sidebands or RF generated sidebands, the contribution of residual optical carrier power to the DC photocurrent will be insignificant.

Similarly, the $I(t)$ terms corresponding to the IF are grouped together to describe the strength of the IF current:

$$I_{\Omega_{IF}}(t) = \frac{R g_{opt} P_0}{4} J_1(A_{RF}) J_1(A_{LO}) cos(\Omega_{IF} t) cos(\Delta\phi_{int}) \qquad 7\text{-}14$$

This $I_{\Omega_{IF}}(t)$ expression explicitly shows the beating between the RF and LO generated optical sidebands through the Bessel function product, $J_1(A_{RF})J_1(A_{LO})$. For the key MWP

metrics of interest, the IF electrical power $P_{\Omega_{IF}}$ is of greater interest than the IF photocurrent. The output IF electrical power of the photodetector is $P_{\Omega_{IF}} = \langle I_{\Omega_{IF}}^2 \rangle R_0 |H_{pd}|^2$, where $\langle I_{\Omega_{IF}}^2 \rangle = \frac{1}{2} I_{\Omega_{IF}}^2$ is the time averaged square of the photocurrent at Ω_{IF}; R_0 is the photodetector output impedance; and H_{pd} is the photodetector filter function. Hence, the IF output power is

$$P_{\Omega_{IF}} = \frac{R^2 g_{opt}^2 P_0^2 R_0 |H_{pd}|^2}{32} J_1^2(A_{RF}) J_1^2(A_{LO}) \cos^2(\Delta\phi_{int}). \quad 7\text{-}15$$

Applying the small signal approximation $J_1(A_{RF}) \approx \frac{A_{RF}}{2}$ and substituting $A_{RF} = \sqrt{\frac{2\pi^2 P_{in,RF} R_{i,RF}}{V_{\pi.RF}^2}}$ yields

$$P_{\Omega_{IF}} = \frac{R^2 g_{opt}^2 P_0^2 R_0 |H_{pd}|^2}{64} \frac{\pi^2 P_{in,RF} R_{i,RF}}{V_{\pi.RF}^2} J_1^2(A_{LO}) \cos^2(\Delta\phi_{int}). \quad 7\text{-}16$$

Rearranging the terms and dividing by the input RF power $P_{in,RF}$ results in the RF-to-IF gain expression:

$$g_{IF} = \frac{\pi^2 R^2 g_{opt}^2 P_0^2 R_{i,RF} R_0 |H_{pd}|^2}{64 V_{\pi.RF}^2} J_1^2(A_{LO}) cos^2(\Delta\phi_{int}) \quad 7\text{-}17$$

The optimal LO drive condition further simplifies this to:

$$g_{IF} = \frac{0.338\pi^2 R^2 g_{opt}^2 P_0^2 R_{i,RF} R_0 |H_{pd}|^2}{64 V_{\pi.RF}^2} cos^2(\Delta\phi_{int}) \quad 7\text{-}18$$

The factor of 0.338 arises from this optimal LO drive condition assumption since $J_{1,max} \approx 0.5819$ and $J_{1,max}^2 \approx 0.5819^2 \approx 0.338$.

7.3.3 Derivation of Linearity Metrics

Next, the derivation of the third-order limited spur-free dynamic range ($SFDR_3$) is derived for the single-drive, single detection photonic frequency converter architecture of Figure 36(a). The analysis must begin again from the optical electric fields just prior to modulation. In the analysis of section 7.3.2, the intermodulation distortion products were not accounted for since the RF input was a single tone. Here, the RF input consists of two tones such that the mixing products between them may be calculated. Again, the derivation here is completed in detail for the single drive, single detection case to illustrate the methodology used for all single-drive/dual-drive and single/balanced detection combinations, with all results summarized in section 7.3.6. Luckily, the electric fields calculated within the LO branch of the macro-interferometer remain valid. Hence, attention is first directed toward recalculating the electric fields throughout the RF branch of the macro-interferometer.

Now, the RF input $A_{RF}(t)$ is:

$$A_{RF}(t) = \phi_{DC} + A_1 \sin(\Omega_1 t) + A_2 \sin(\Omega_2 t). \qquad 7\text{-}19$$

Here, the first term is a DC component; the second term is an RF tone at Ω_1; and the third term is another RF tone at Ω_2. Upon modulation by the RF MZM, the generated optical electric field is

$$E_{3a} = \frac{\gamma}{2\sqrt{2}} e^{j\omega t} \left(e^{j\phi_{DC}} \sum_{k=-\infty}^{\infty} J_k(A_1) e^{jk\Omega_1 t} \sum_{k=-\infty}^{\infty} J_k(A_2) e^{jk\Omega_2 t} - 1 \right) \quad 7\text{-}20$$

Passing through the DC optical phase shift $\Delta\phi_{int}$ and truncating Bessel function terms with order higher than 2 results in

$$\begin{aligned} E_{5a} = \tfrac{\gamma}{2\sqrt{2}} e^{j\omega t} e^{j\Delta\phi_{int}} \big(e^{j\phi_{DC}} \big(& J_2(A_1) e^{-j2\Omega_1 t} - J_1(A_1) e^{-j\Omega_1 t} + J_0(A_1) + \\ & J_1(A_1) e^{j\Omega_1 t} + J_2(A_1) e^{j2\Omega_1 t} \big) \big(J_2(A_2) e^{-j2\Omega_2 t} - J_1(A_2) e^{-j\Omega_2 t} + J_0(A_2) + \\ & J_1(A_2) e^{j\Omega_2 t} + J_2(A_2) e^{j2\Omega_2 t} \big) - 1 \big). \end{aligned} \quad 7\text{-}21$$

Then E_{5a} and E_{5b} are added (with a phase shift) by the 2x2 directional coupler, yielding the optical field incident on the photodetector.

$$\begin{aligned} E_{6a} = \frac{\gamma}{4} e^{j\omega t} \Big(& e^{j\Delta\phi_{int}} \big(e^{j\phi_{DC}} \big(J_2(A_1) e^{-j2\Omega_1 t} - J_1(A_1) e^{-j\Omega_1 t} + J_0(A_1) \\ & + J_1(A_1) e^{j\Omega_1 t} + J_2(A_1) e^{j2\Omega_1 t} \big) \big(J_2(A_2) e^{-j2\Omega_2 t} \\ & - J_1(A_2) e^{-j\Omega_2 t} + J_0(A_2) + J_1(A_2) e^{j\Omega_2 t} + J_2(A_2) e^{j2\Omega_2 t} \big) - 1 \big) \\ & + j\big(e^{j\phi_{DC}} \left(J_0(A_{LO}) + J_1(A_{LO}) \big(e^{j\Omega_{LO} t} + e^{-j\Omega_{LO} t} \big) \right) - 1 \big) \Big) \end{aligned} \quad 7\text{-}22$$

As the terms arising from modulation of Ω_1 and Ω_2 are multiplied out, proceeding yields unwieldy expressions. Hence, substitutions are made with temporary variables U and V to simplify the mathematics:

$$E_{6a} = \frac{\gamma}{4} e^{j\omega t} \big(e^{j\Delta\phi_{int}} \big(e^{j\phi_{DC}} (U) - 1 \big) + j\big(e^{j\phi_{DC}} (V) - 1 \big) \big) \quad 7\text{-}23$$

where,

$$
\begin{aligned}
&U \\
&= J_2(A_1)J_2(A_2)e^{-j2(\Omega_1+\Omega_2)t} - J_1(A_2)J_2(A_1)e^{-j(2\Omega_1+\Omega_2)t} \\
&+ J_0(A_2)J_2(A_1)e^{-j2\Omega_1 t} + J_1(A_2)J_2(A_1)e^{-j(2\Omega_1-\Omega_2)t} \\
&+ J_2(A_1)J_2(A_2)e^{-j2(-\Omega_2+\Omega_1)t} - J_1(A_1)J_2(A_2)e^{-j(2\Omega_2+\Omega_1)t} \\
&+ J_1(A_1)J_1(A_2)e^{-j(\Omega_1+\Omega_2)t} - J_0(A_2)J_1(A_1)e^{-j\Omega_1 t} - J_1(A_1)J_1(A_2)e^{-j(\Omega_1-\Omega_2)t} \\
&- J_1(A_1)J_2(A_2)e^{-j(\Omega_1-2\Omega_2)t} + J_0(A_1)J_2(A_2)e^{-j2\Omega_2 t} \\
&- J_0(A_1)J_1(A_2)e^{-j\Omega_2 t} + J_0(A_1)J_0(A_2) + J_0(A_1)J_1(A_2)e^{j\Omega_2 t} + J_0(A_1)J_2(A_2)e^{j2\Omega_2 t} \\
&+ J_1(A_1)J_2(A_2)e^{-j(2\Omega_2-\Omega_1)t} - J_1(A_1)J_1(A_2)e^{-j(\Omega_2-\Omega_1)t} + J_0(A_2)J_1(A_1)e^{j\Omega_1 t} \\
&+ J_1(A_1)J_1(A_2)e^{j(\Omega_1+\Omega_2)t} + J_1(A_1)J_2(A_2)e^{j(\Omega_1+2\Omega_2)t} \\
&+ J_2(A_2)J_2(A_1)e^{j2(\Omega_1-\Omega_2)t} - J_1(A_2)J_2(A_1)e^{j(2\Omega_1-\Omega_2)t} + J_0(A_2)J_2(A_1)e^{j2\Omega_1 t} \\
&+ J_1(A_2)J_2(A_1)e^{j(2\Omega_1+\Omega_2)t} + J_2(A_1)J_2(A_2)e^{j2(\Omega_1+\Omega_2)t}
\end{aligned}
\tag{7-24}
$$

and

$$V = J_0(A_{LO}) + J_1(A_{LO})\left(e^{j\Omega_{LO}t} + e^{-j\Omega_{LO}t}\right). \tag{7-25}$$

Hence, the conjugate of E_{6a}, necessary for calculating the detected photocurrent is

$$E_{6a}^* = \frac{\gamma}{4}e^{-j\omega t}\left(e^{-j\Delta\phi_{int}}\left(e^{-j\phi_{DC}}(U^*) - 1\right) - j\left(e^{-j\phi_{DC}}(V^*) - 1\right)\right) \tag{7-26}$$

Next, the product $E_{6a}E_{6a}^*$ is calculated:

$$E_{6a}E_{6a}^{*} = \frac{\gamma^2}{16}\Big[\Big(e^{j\Delta\phi_{int}}\big(e^{j\phi_{DC}}(U)-1\big) + j\big(e^{j\phi_{DC}}(V) - 1\big)\Big)\Big(e^{-j\Delta\phi_{int}}\big(e^{-j\phi_{DC}}(U^*)-1\big) - j\big(e^{-j\phi_{DC}}(V^*)-1\big)\Big)\Big] \quad 7\text{-}27$$

Fortunately, from observation of the expressions for U, V, and their conjugates, the only terms relevant to the IF arise from products of VU^* and UV^*.

Hence the field product relevant to the $SFDR$ is:

$$E_{6a}E_{6a}^{*}(IF\ terms\ only) = \frac{j\gamma^2}{16}\big[-e^{j\Delta\phi_{int}}(UV^*) + e^{-j\Delta\phi_{int}}(VU^*)\big] \quad 7\text{-}28$$

$$\begin{aligned} VU^*(IF\ terms\ only) &= J_1(A_{LO})\big(e^{-j\Omega_{LO}t} + e^{+j\Omega_{LO}t}\big)\big[J_1(A_2)J_2(A_1)\big(e^{j(2\Omega_1-\Omega_2)t} \\ &- e^{-j(2\Omega_1-\Omega_2)t}\big) + J_0(A_2)J_1(A_1)\big(e^{-j\Omega_1 t} - e^{j\Omega_1 t}\big) \\ &+ J_1(A_1)J_2(A_2)\big(e^{j(2\Omega_2-\Omega_1)t} - e^{-j(\Omega_2-2\Omega_1)t}\big) \\ &+ J_0(A_1)J_1(A_2)(e^{-j\Omega_2 t} - e^{j\Omega_2 t})\big] \end{aligned} \quad 7\text{-}29$$

$$\begin{aligned} VU^*(IF\ terms\ only) &= J_1(A_{LO})J_1(A_2)J_2(A_1)\big(e^{j(2\Omega_1-\Omega_2-\Omega_{lo})t} - e^{-j(2\Omega_1-\Omega_2-\Omega_{lo})t}\big) \\ &+ J_1(A_{LO})J_0(A_2)J_1(A_1)\big(e^{-j(\Omega_1-\Omega_{lo})t} - e^{j(\Omega_1-\Omega_{lo})t}\big) \\ &+ J_1(A_{LO})J_1(A_1)J_2(A_2)\big(e^{j(2\Omega_2-\Omega_1-\Omega_{lo})t} - e^{-j(2\Omega_2-\Omega_1-\Omega_{lo})t}\big) \\ &+ J_1(A_{LO})J_0(A_1)J_1(A_2)(e^{-j(\Omega_2-\Omega_{lo})t} - e^{j(\Omega_2-\Omega_{lo})t}) \end{aligned} \quad 7\text{-}30$$

As it turns out, for the IF terms $VU^* = -UV^*$, simplifying the $E_{6a}E_{6a}^{*}$ product relevant to the IF terms:

$$E_{6a}E_{6a}^{*}(IF\ terms\ only) = \frac{-j\gamma^2}{8}UV^{*}\cos\left(\Delta\phi_{int}\right) \tag{7-31}$$

Resubstituting in U and V expressions then yields:

$$\begin{aligned} E_{6a}E_{6a}^{*} = -j\frac{\gamma^2}{8}cos(\Delta\phi_{int})\big[&J_1(A_{LO})J_1(A_2)J_2(A_1)\big(e^{-j(2\Omega_1-\Omega_2-\Omega_{LO})t} \\ &- e^{j(2\Omega_1-\Omega_2-\Omega_{LO})t}\big) \\ &+ J_1(A_{LO})J_0(A_2)J_1(A_1)\big(e^{j(\Omega_1-\Omega_{LO})t} - e^{-j(\Omega_1-\Omega_{LO})t}\big) \\ &+ J_1(A_{LO})J_1(A_1)J_2(A_2)\big(e^{-j(2\Omega_2-\Omega_1-\Omega_{LO})t} - e^{j(2\Omega_2-\Omega_1-\Omega_{LO})t}\big) \\ &+ J_1(A_{LO})J_0(A_1)J_1(A_2)(e^{j(\Omega_2-\Omega_{LO})t} - e^{-j(\Omega_2-\Omega_{LO})t})\ \big] \end{aligned} \tag{7-32}$$

The fundamental and IMD3 frequencies can now be explicitly identified as the following. Assuming $\Omega_2 > \Omega_1 > \Omega_{LO}$, the "left" of carrier or lower frequency IF fundamental is $\Omega_{fund,L} = \Omega_1 - \Omega_{LO}$. The "right" of carrier or higher frequency IF fundamental is $\Omega_{fund,R} = \Omega_2 - \Omega_{LO}$. The "left" and "right" IF IMD3's are similarly identified as $\Omega_{imd3,L} = 2\Omega_1 - \Omega_2 - \Omega_{LO}$ and $\Omega_{imd3,R} = 2\Omega_2 - \Omega_1 - \Omega_{LO}$. Applying these definitions and further simplifying terms yields:

$$\begin{aligned} E_{6a}E_{6a}^{*} = \frac{\gamma^2}{8}cos(\Delta\phi_{int})\big[&-2J_1(A_{LO})J_1(A_2)J_2(A_1)sin\big(\Omega_{imd3,L}t\big) \\ &+ 2J_1(A_{LO})J_0(A_2)J_1(A_1)sin\big(\Omega_{fund,L}t\big) \\ &- 2J_1(A_{LO})J_1(A_1)J_2(A_2)sin\big(\Omega_{imd3,R}t\big) \\ &+ 2J_1(A_{LO})J_0(A_1)J_1(A_2)sin\big(\Omega_{fund,R}t\big)\big] \end{aligned} \tag{7-33}$$

Hence, four terms remain, each a function of the LO tone and the two RF input tones. Substituting $\gamma^2 = \frac{2l_{MZM}P_0}{A}\left(\frac{\mu}{\epsilon}\right)^{1/2}$, the time averaged IF currents $\langle I^2_{\Omega_{\mathrm{IF}}}\rangle = \left(\frac{1}{\sqrt{2}}\right)^2 I^2_{\Omega_{\mathrm{IF}}}$ are calculated for each term:

$$\left\langle I^2_{\Omega_{imd3,L}}\right\rangle = \frac{R^2 l^2_{MZM} P_0^2}{32} cos^2(\Delta\phi_{int}) J_1^2(A_{LO}) J_1^2(A_2) J_2^2(A_1) \quad 7\text{-}34$$

$$\left\langle I^2_{\Omega_{fund,L}}\right\rangle = \frac{R^2 l^2_{MZM} P_0^2}{32} cos^2(\Delta\phi_{int}) J_1^2(A_{LO}) J_0^2(A_2) J_1^2(A_1) \quad 7\text{-}35$$

$$\left\langle I^2_{\Omega_{imd3,R}}\right\rangle = \frac{R^2 l^2_{MZM} P_0^2}{32} cos^2(\Delta\phi_{int}) J_1^2(A_{LO}) J_1^2(A_1) J_2^2(A_2) \quad 7\text{-}36$$

$$\left\langle I^2_{\Omega_{fund,R}}\right\rangle = \frac{R^2 l^2_{MZM} P_0^2}{32} cos^2(\Delta\phi_{int}) J_1^2(A_{LO}) J_0^2(A_1) J_1^2(A_2) \quad 7\text{-}37$$

Because $\left\langle I^2_{\Omega_{imd3,L}}\right\rangle = \left\langle I^2_{\Omega_{imd3,R}}\right\rangle$ and $\left\langle I^2_{\Omega_{fund,L}}\right\rangle = \left\langle I^2_{\Omega_{fund,R}}\right\rangle$ if the input amplitude A_1 and A_2 are equal, as is the case in standard equal-amplitude two-tone experimental methods, the left fundamental/IMD3 pair and the right fundamental/IMD3 will each produce the same $SFDR$ and other linearity metrics. Hence, the derivations need only proceed with one pair, the left pair in this case.

Converting to electrical power via $P_{\Omega_{\mathrm{IF}}} = \langle I^2_{\Omega_{\mathrm{IF}}}\rangle R_0 \left|H_{pd}\right|^2$ and applying the optimal LO drive condition assumption and the small signal approximations for both RF input tones then produces

$$P_{\Omega_{imd3,L}} = \frac{0.338R^2 l_{MZM}^2 P_0^2 R_0 \left|H_{pd}\right|^2}{32} cos^2(\Delta\phi_{int}) \frac{A_2^2}{16} \frac{A_1^4}{32^2} \quad 7\text{-}38$$

$$P_{\Omega_{fund,L}} = \frac{0.338R^2 l_{MZM}^2 P_0^2 R_0 \left|H_{pd}\right|^2}{32} cos^2(\Delta\phi_{int}) \frac{A_1^2}{16}, \quad 7\text{-}39$$

where $A_1^2 = \frac{2\pi^2 P_{in,1} R_{i,rf}}{V_{\pi.rf}^2}$ and $A_2^2 = \frac{2\pi^2 P_{in,2} R_{i,rf}}{V_{\pi.rf}^2}$.

Assuming an equal-amplitude test such that $P_{in,1} = P_{in,2}$, the fundamental and third-order intermodulation distortion powers are

$$P_{\Omega_{imd3,L}} = \frac{0.338\pi^6 R^2 l_{MZM}^2 P_0^2 R_0 \left|H_{pd}\right|^2}{2 \cdot 32^3} cos^2(\Delta\phi_{int}) \frac{P_{in,1}^3 R_{i,rf}^3}{V_{\pi.rf}^6} \quad 7\text{-}40$$

$$P_{\Omega_{fund,L}} = \frac{0.338\pi^2 R^2 l_{MZM}^2 P_0^2 R_0 \left|H_{pd}\right|^2}{256} cos^2(\Delta\phi_{int}) \frac{P_{in,1} R_{i,rf}}{V_{\pi.rf}^2}. \quad 7\text{-}41$$

Recalling the definition of the third-order output intercept point from Chapter 2, $OIP_3 = \left(\frac{P_{\Omega_{fund}}^3}{P_{\Omega_{imd3}}}\right)^{\left(\frac{1}{2}\right)}$, the $OIP3$ expression is obtained.

$$OIP3 = \frac{0.338R^2 l_{MZM}^2 P_0^2 R_0 \left|H_{pd}\right|^2}{16} cos^2(\Delta\phi_{int}) \quad 7\text{-}42$$

Subsequently, the $SFDR_3$ is derived from the $OIP3$:

$$SFDR_3 = \left(\frac{OIP_3}{N_{out}B}\right)^{2/3} = \left(\frac{0.338R^2 I_{MZM}^2 P_0^2 R_0 \left|H_{pd}\right|^2}{16 N_{out} B} cos^2(\Delta\phi_{int})\right)^{\frac{2}{3}} \quad 7\text{-}43$$

7.3.4 Derivation of Noise Metrics

Lastly, the metrics of noise power spectral density N_{out} and noise factor F are derived by beginning with the noise factor expression for the standard RF photonic link:

$$N_{out,RFoF} = g_{ss} k_B T_s + k_B T_s + 2qI_{dc} R_o \left|H_{pd}\right|^2 + RIN\, I_{dc}^2 R_o \left|H_{pd}\right|^2 \quad 7\text{-}44$$

The first term corresponds to the input thermal noise contribution to the output noise; the second term is the output thermal noise; the third term is the shot noise contribution; and the final term is the relative intensity noise (RIN) contribution. Comparing the architectures of the photonic frequency converters here and the intensity-modulated, direct-detection RF photonic link, the only new source of noise is the input noise to the LO modulator. Hence, the N_{out} for the photonic frequency converting link simply includes an extra noise term for the input noise from the LO modulator, assumed to be thermally limited.

$$N_{out} = g_{RF} k_B T_s + g_{LO} k_B T_s + k_B T_s + 2qI_{dc} R_o \left|H_{pd}\right|^2 + RINI_{dc}^2 R_o \left|H_{pd}\right|^2 \quad 7\text{-}45$$

Here, g_{RF} is the small signal gain of the photonic frequency converter, referred to the RF path, i.e. relating the ratio of IF output power to RF input power. The small signal approximation is used since the input noise equivalent voltages are assumed small in comparison to the modulator half-wave voltages. This g_{RF} is identical to the previously derived gain, simply denoted g_{IF}. Here again, the g_{IF} expression assuming optimal LO drive conditions is employed. The new second term $g_{LO}k_BT_s$ is the LO modulator input noise multiplied by the small signal LO-referred gain, g_{LO}, which relates the ratio of the IF output power to the input LO power.

$$g_{LO} \approx \frac{\pi^4 l_{MZM}^2 R^2 P_0^2 R_0 \left|H_{pd}\right|^2}{128} \frac{R_{i,LO}}{V_{\pi.LO}^2} \frac{P_{in,rf} R_{i,rf}}{V_{\pi.rf}^2} cos^2(\Delta\phi_{int}) \tag{7-46}$$

Besides this difference, the existing shot noise and RIN noise contributions remain unchanged as these are written in terms of I_{DC}. From N_{out}, the noise factor F is simply derived via $F = \frac{N_{out}}{g k_B T_s}$:

$$F = \frac{1}{g_{RF} k_B T_s}\Big(g_{RF} k_B T_s + g_{LO} k_B T_s + k_B T_s + 2qI_{DC}R_o\left|H_{pd}\right|^2 + RINI_{DC}^2 R_o\left|H_{pd}\right|^2\Big) \tag{7-47}$$

Distributing the $g_{RF}k_BT_s$ expression in the denominator and simplifying, the following is obtained,

$$F = 1 + \frac{g_{LO}}{g_{RF}} + \frac{1}{g_{RF}}\left(1 + \frac{2qI_{DC}R_o\left|H_{pd}\right|^2}{k_BT_s} + \frac{RINI_{DC}^2 R_o\left|H_{pd}\right|^2}{k_BT_s}\right). \tag{7-48}$$

The second term, corresponding to the LO input's thermal noise contribution, manifests as a ratio of the LO-referred gain to the RF-referred gain. An interesting conclusion from this is the slight advantage found in trading RF input power for increased LO input power. This is more directly observed by substituting in the expressions assuming both the RF and LO inputs are small signal, yielding the following result:

$$F = 1 + \frac{P_{in,RF}}{P_{in,LO}} + \frac{1}{g_{RF}}\left(1 + \frac{2qI_{DC}R_o\left|H_{pd}\right|^2}{k_BT_s} + \frac{RINI_{DC}^2R_o\left|H_{pd}\right|^2}{k_BT_s}\right) \qquad 7\text{-}49$$

Hence, increasing the $P_{in,LO}$ and reducing $P_{in,rf}$ lowers the system's noise factor, though this second term is typically small, since $P_{in,RF} < P_{in,LO}$, especially when the LO modulator's optimal drive condition is achieved. Note the above expression does not assume the optimal LO drive condition as the final gain expressions in previous sections have assumed. The gain expressions employed to achieve the above expression must assume small-signal inputs to *both* the LO and RF modulators. Under optimal LO drive conditions, the second term is more complex as many of the common terms of the g_{RF} and g_{LO} expressions do not cancel, leaving the second term as: $\frac{\pi^2 g_{opt}R_{i,LO}P_{in,rf}}{2*0.338V_{\pi.LO}^2}$. Nonetheless, this second term is typically small compared to other noise sources, even smaller than the input RF noise. Hence, neglecting the input noise contribution from the LO modulator and substituting in the RF-to-IF gain g_{IF} assuming optimal LO drive conditions results in:

$$F = 1 + \frac{64V_{\pi.rf}^2}{0.338\pi^2 R^2 l_{MZM}^2 P_0^2 R_{i,rf}} \left(\frac{1}{R_o \left| H_{pd} \right|^2} + \frac{2qI_{DC}}{k_B T_s} + \frac{RINI_{DC}^2}{k_B T_s} \right) \qquad 7\text{-}50$$

7.3.5 Accounting for Dual-Drive and Balanced Detection Cases

For the sake of brevity, the dual-drive and balanced detection cases are not derived explicitly here in detail. Instead, the methodology is illustrated sufficiently such that a detailed derivation can be completed by the reader, if desired.

The balanced detection case is easily derived with the single detection derivation on hand, beginning with the single detection photocurrents. Balanced detection subtracts the two single photodetector currents, resulting in theoretically zero DC photocurrent but double the current magnitudes for the IF currents. This selective behavior occurs because the DC terms output by both photodetectors share the name sign, but the IF terms have opposite signs. Hence, electrical subtraction eliminates the DC photocurrent while strengthening the IF currents. Nonetheless, for purposes of calculating the noise, the convention from [5] is adopted whereby the balanced detection I_{DC} is defined as the *sum* of the individual photodetector currents. While not reflecting the physical reality of balanced detection, this definition of the balanced detection photocurrent enables convenient calculation of noise terms, such as shot noise, using the previously derived F and N_{out} expressions. Hence, the balanced detection noise factor, assuming the LO input noise is small relative to the other noise sources, is:

$$F \approx 1 + \frac{1}{g_{IF,bal}}\left(1 + \frac{2qI_{dc,bal}R_o\left|H_{pd}\right|^2}{k_B T_s} + \frac{RINI_{dc,bal}^2 R_o\left|H_{pd}\right|^2}{k_B T_s}\right) \quad 7\text{-}51$$

where $I_{DC,bal}$ is the sum of the individual DC photocurrent, and $g_{IF,bal}$ is the gain of the photonic frequency converter with balanced detection.

Because the output IF photocurrent is doubled due to balanced detection, the output IF electrical powers of the IF and IMD3 terms are increased by a factor of four. This multiplicative factor thus impacts the system gain and $SFDR_3$, i.e. the gain is multiplied by four:

$$g_{IF,bal} = \frac{0.338\pi^2 R^2 g_{opt}^2 P_0^2 R_{i,RF} R_0\left|H_{pd}\right|^2}{16V_{\pi.RF}^2} cos^2(\Delta\phi_{int}) \quad 7\text{-}52$$

From the definitions of $OIP3$ and $SFDR_3$, this factor of four can be easily mapped to the new $SFDR$ in comparison to the single-drive, single detection expressions.

$$OIP3_{bal} = \left(\frac{P_{\Omega_{fund,bal}}^3}{P_{\Omega_{imd3,bal}}}\right)^{\left(\frac{1}{2}\right)} = \left(\frac{\left(4P_{\Omega_{fund}}\right)^3}{4P_{\Omega_{imd3}}}\right)^{\left(\frac{1}{2}\right)} = 4 \cdot OIP3 \quad 7\text{-}53$$

$$SFDR_{3,bal} = \left(\frac{4 \cdot OIP3}{N_{out}B}\right)^{2/3} = \left(\frac{0.3382R^2 l_{MZM}^2 P_0^2 R_0\left|H_{pd}\right|^2}{4N_{out}B} cos^2(\Delta\phi_{int})\right)^{\frac{2}{3}} \quad 7\text{-}54$$

Hence, balanced detection increases the $SFDR$ by a factor $4^{2/3}$ at first glance. However, note that the balanced detector N_{out} must be substituted, which although identical when

cast in terms of I_{DC}, is significantly lower in many cases due to balanced detection's suppression of the DC photocurrent and common mode noise sources like RIN.

Concerning dual-drive implementations, the derivation must return to the modulated electric fields E_{3a} and E_{3b} and include differential modulation of both phase shifters within the RF and LO MZMs. The new RF-modulated and LO-modulated electric fields are:

$$E_{3a,DD} = \frac{\gamma}{2\sqrt{2}} e^{j\omega t} \left(e^{\frac{j\phi_{DC}}{2}} \sum_{k=-\infty}^{\infty} J_k(A_{RF}) e^{jk\Omega_{RF}t} - e^{\frac{-j\phi_{DC}}{2}} \sum_{k=-\infty}^{\infty} J_k(A_{RF}) e^{-jk\Omega_{RF}t} \right) \quad 7\text{-}55$$

$$E_{3b,DD} = \frac{j\gamma}{2\sqrt{2}} e^{j\omega t} \left(e^{\frac{j\phi_{DC}}{2}} \sum_{k=-\infty}^{\infty} J_k(A_{LO}) e^{jk\Omega_{LO}t} - e^{\frac{-j\phi_{DC}}{2}} \sum_{k=-\infty}^{\infty} J_k(A_{LO}) e^{-jk\Omega_{LO}t} \right) \quad 7\text{-}56$$

The analysis continues as before to produce the dual-drive gain, $SFDR$, NF, and N_{out}.

7.3.6 Summary of Simplified Equations

In this section the equations describing the main metrics of interest for photonic frequency converters are summarized for architectures employing all combinations of single or dual drive and single or balanced detection schemes. Fortunately, the differences between the architectural variants are fully captured by mere multiplicative factors, except for the DC photocurrent. These multiplicative factors are introduced as X_G for the gain expression, X_{SFDR} for the $SFDR_3$, and $X_{I_{DC}}$ and $Y_{I_{DC}}$ parameters for the DC photocurrent. Note that F

expressions are cast in terms of g_{IF} and hence do not require an independent multiplicative factor. The values for these factors are given in Table 8.

$$g_{IF} = \frac{0.338 X_G \pi^2 R^2 g_{opt}^2 P_0^2 R_{i,RF} R_0 \left|H_{pd}\right|^2}{V_{\pi.RF}^2} cos^2(\Delta\phi_{int}) \tag{7-57}$$

$$F = 1 + \frac{P_{in,RF}}{P_{in,LO}} + \frac{1}{g_{IF}}\left(1 + \frac{2qI_{DC}R_o\left|H_{pd}\right|^2}{k_B T_s} + \frac{RINI_{DC}^2 R_o \left|H_{pd}\right|^2}{k_B T_s}\right) \tag{7-58}$$

$$SFDR_3 = \left(\frac{0.338 X_{SFDR} R^2 g_{opt}^2 P_0^2 R_0 \left|H_{pd}\right|^2}{N_{out} B} cos^2(\Delta\phi_{int})\right)^{\frac{2}{3}} \tag{7-59}$$

$$I_{DC} = X_{I_{DC}} R g_{opt} P_0 \left(Y_{I_{DC}} + \frac{\pi^2 P_{in,RF} R_{i,RF}}{V_{\pi.RF}^2}\right) \tag{7-60}$$

Note while only g_{IF} and $SFDR_3$ expressions above appear to be functions of the macro-interferometer phase $\Delta\phi_{int}$, the DC photocurrent I_{DC} and hence F are also functions of $\Delta\phi_{int}$; here the assumption that $\Delta\phi_{int} = 0$ was applied to I_{DC} and hence F since these equations would not simplify otherwise. The generalized expressions for I_{DC} are given in the next section. Likewise, I_{DC} and F are functions of the MZM bias ϕ_{DC}, though the assumption here is that $\phi_{DC} = 0$ corresponding to null bias, which is beneficial for noise reduction. Additionally, because I_{DC} determines N_{out}, the $SFDR_3$ (also dependent on N_{out}) is a more complex function of both $\Delta\phi_{int}$ and ϕ_{DC}; hence, the N_{out} using the generalized I_{DC} expressions of the next subsection should be used for assessing the $SFDR$ when $\Delta\phi_{int} \neq 0$ or $\phi_{DC} \neq 0$. Nonetheless, the most common bias condition will be when $\Delta\phi_{int} = 0$ and $\phi_{DC} = 0$ since these conditions typically maximize the gain of the system.

Per the g_{IF} expression above, the gain is always a function of the macro-interferometer bias point $\Delta\phi_{int}$, but is only a function of ϕ_{DC} for dual-drive implementations. In dual-drive (push-pull) implementations, the fundamental sidebands generated by each phase shifter in an MZM can interact when coupled, i.e. add vectorially; however, in single-drive (push-only) implementations (with the DC phase control on the unmodulated arm) the fundamental sidebands generated by the modulated phase shifter have no signals to add interferometrically with, since the unmodulated phase shifter simply passes an un-modulated carrier. Hence, only the dual-drive MZM's output optical carrier amplitudes are affected by the MZM bias point ϕ_{DC}. The single-drive MZM simply acts as a phase modulator with excess carrier power recombined at its output; hence the gain of single-drive MZM based frequency converters is independent of ϕ_{DC}. This feature means the MZM bias point for single-drive implementations should be determined solely by its impact on N_{out} and $SFDR$. See section 7.3.11 for more details on phase sensitivities.

Table 8– Summary of Frequency Converter Link Factors.

	Single Drive		Dual Drive	
Factor	Single Detection	Balanced Detection	Single Detection	Balanced Detection
X_G	$\frac{1}{64}$	$\frac{1}{16}$	$\frac{1}{4}cos^2(\phi_{DC})$	$cos^2(\phi_{DC})$
X_{SFDR}	$\frac{1}{16}$	$\frac{1}{4}$	$\frac{1}{4}cos^2(\phi_{DC})$	$cos^2(\phi_{DC})$
$X_{I_{DC}}$	$\frac{1}{16}$	$\frac{1}{8}$	$\frac{1}{4}$	$\frac{1}{2}$
$Y_{I_{DC}}$	1.146		0.677	

7.3.7 Generalized Equations

Here the generalized g_{IF}, F, $SFDR_3$, and I_{DC} expressions are given, without any assumptions on the RF or LO modulation strengths, nor on the $\Delta\phi_{int}$ and ϕ_{DC} biases. Where present, the multiplicative factors retain their values given in Table 8. The gain g_{IF} is:

$$g_{IF} = X_G \frac{\pi^2 R^2 g_{opt}^2 P_0^2 R_{i,RF} R_0 \left|H_{pd}\right|^2}{64 V_{\pi.RF}^2} J_1^2(A_{LO}) cos^2(\Delta\phi_{int}) \qquad 7\text{-}61$$

Note this result still assumes the RF input voltage is small signal, as this is necessary to obtain an explicit gain equation. For large signal RF inputs, 7-61 should be recast in terms of $P_{\Omega_{\mathrm{IF}}}$ and compared numerically to the input RF power.

The noise metrics are left generally unchanged from the previous subsection:

$$N_{out} = g_{RF} k_B T_s + g_{LO} k_B T_s + k_B T_s + 2qI_{dc} R_o \left|H_{pd}\right|^2 + RINI_{dc}^2 R_o \left|H_{pd}\right|^2 \qquad 7\text{-}62$$

$$F = 1 + \frac{g_{LO}}{g_{RF}} + \frac{1}{g_{RF}} \left(1 + \frac{2qI_{dc} R_o \left|H_{pd}\right|^2}{k_B T_s} + \frac{RINI_{dc}^2 R_o \left|H_{pd}\right|^2}{k_B T_s} \right) \qquad 7\text{-}63$$

The $SFDR_3$ expression is more complex, containing multiple Bessel functions (of the first kind) of order 0, 1, and 2, though these are easily evaluated numerically.

$$SFDR_3 = \left(\frac{X_{SFDR} R^2 g_{opt}^2 P_0^2 R_0 \left|H_{pd}\right|^2 J_0^3(\phi_{RF}) J_1^2(\phi_{RF}) J_1^2(\phi_{LO})}{2 N_{out} B J_2(\phi_{RF})} \right)^{\frac{2}{3}} \qquad 7\text{-}64$$

Lastly, the general photocurrent expressions contain the most terms, as these include both self-beat terms from RF and LO generated optical sidebands as well as the mixing terms contributing to the IF photocurrent. The single-drive photocurrents for single detection ($I_{DC,SD,SDet}$) and balanced detection ($I_{DC,SD,BDet}$) are:

$$\begin{aligned} I_{DC,SD,SDet} = \frac{1}{16} R g_{opt} P_0 \big[& 2 + J_0^2(A_{RF}) + J_0^2(A_{LO}) + 2J_1^2(A_{RF}) + 2J_1^2(A_{LO}) \\ & - 2cos(\Delta\phi_{int})(J_0(A_{RF})J_0(A_{LO}) + 1) \\ & + 2J_0(A_{RF})cos(\phi_{DC} + \Delta\phi_{int}) + 2J_0(A_{LO})cos(\phi_{DC} - \Delta\phi_{int}) \\ & - 2\big(J_0(A_{LO}) + J_0(A_{RF})\big)cos(\phi_{DC})\big] \end{aligned} \quad \text{7-65}$$

$$\begin{aligned} I_{DC,SD,BDet} = \frac{1}{8} R g_{opt} P_0 \big[& 2 + J_0^2(A_{RF}) + J_0^2(A_{LO}) + 2J_1^2(A_{RF}) + 2J_1^2(A_{LO}) \\ & - 2cos(\Delta\phi_{int})(J_0(A_{RF})J_0(A_{LO}) + 1) \\ & + 2J_0(A_{RF})cos(\phi_{DC} + \Delta\phi_{int}) + 2J_0(A_{LO})cos(\phi_{DC} - \Delta\phi_{int}) \\ & - 2\big(J_0(A_{LO}) + J_0(A_{RF})\big)cos(\phi_{DC})\big] \end{aligned} \quad \text{7-66}$$

The dual-drive photocurrents for single detection ($I_{DC,DD,SDet}$) and balanced detection ($I_{DC,DD,BDet}$) are:

$$\begin{aligned} I_{DC,DD,SDet} = \frac{1}{4} R\, g_{opt} P_0 \Big(& \big(J_0^2(A_{RF}) + J_0^2(A_{LO}) \\ & - 2cos(\Delta\phi_{int})J_0(A_{RF})J_0(A_{LO})\big)sin^2(\phi_{DC}) \\ & + 2\big(J_1^2(A_{RF}) + J_1^2(A_{LO})\big)cos^2(\phi_{DC})\Big) \end{aligned} \quad \text{7-67}$$

$$I_{DC,DD,BDet} = \frac{1}{2} R\, g_{opt} P_0 \Big(\big(J_0^2(A_{RF}) + J_0^2(A_{LO}) - 2cos(\Delta\phi_{int}) J_0(A_{RF}) J_0(A_{LO}) \big) sin^2(\phi_{DC}) + 2\big(J_1^2(A_{RF}) + J_1^2(A_{LO}) \big) cos^2(\phi_{DC}) \Big) \quad \text{7-68}$$

where subscripts for I_{DC} are defined as SD = single-drive, DD = dual-drive, SDet = single detection, and BDet = balanced detection. Substituting the appropriate I_{DC} equation above into the F and N_{out} expressions in the last subsection will yield the appropriate noise metrics (and hence $SFDR$) for cases in which previous assumptions are invalid; e.g. non-optimal LO drive conditions or $\Delta\phi_{int} \neq 0$ or $\phi_{DC} \neq 0$.

7.3.8 Performance Trends

Using the equations of section 7.3.6, the gain, $SFDR_3$, and noise metrics are calculated as a function of optical power for the four architectures in Figure 36 to compare performance trends. The following results reflect component metrics (Table 9) of the InP downconverter experimentally characterized in Ch. 9, which validates experimentally the calculations of this section. Additionally, the frequency converter architectures and the RF photonic link are simulated in Lumerical INTERCONNECT for three different optical powers to verify the trends of this section; however, only the simulated data points (in diamonds) for the RF photonic link and the single-drive, single detection architecture are shown here for clarity. All simulations are in close agreement with the results using the derived analytic equations.

First the RF power gain response vs. optical launch power is investigated, Figure 39(a), demonstrating the expected $g_{IF} \propto P_{opt}^2$ dependence, which manifests as a slope = 2 rise in

gain with optical power on a dB scale. The frequency converter gain retains the square dependence on optical power since a single laser supplies both RF and LO branches. While the RF photonic link demonstrates the best gain, the dual-drive, balanced detection frequency converter's gain is only 4.6 dB lower and is the best performing frequency converter architecture. The dual-drive, single detection frequency converter exhibits 6 dB less gain than its balanced detection counterpart. Likewise, the single-drive, balanced detection case exhibits 6 dB less gain than the previous. Finally, the single-drive, single detection case exhibits 6 dB less gain than its balanced detection counterpart. Hence, the frequency converter architectures exhibit gain performance benefits in increments of 6 dB.

Table 9– Summary of InP Frequency Converter Component Metrics and Parameters.

Metric	Value	Unit
Laser Power, P_0	13.5	dBm
Laser RIN	-150	dB/Hz
SOA Gain	9	dB
SOA NF	4	dB
MZM V_π	4	V
MZM Loss	5.4	dB
$R_{i,RF} = R_{i,LO} = R_o$	50	Ω
R	1	A/W
$\Delta\phi_{int}$	0	rad
ϕ_{DC}	0	rad
H_{pd}	1	

For all frequency converters and the RF photonic link, the DC photocurrent I_{DC} is a linear function of the optical power, Figure 39.

Unlike gain and I_{DC}, the noise power spectral density, N_{out}, (the "noise floor") exhibits a complex relationship with optical power, Figure 39(c). At low powers < 0 dBm, N_{out} is dominated by output thermal noise, which is not a function of the optical power. As the optical power increases above 0 dBm, the shot noise ($\propto P_{opt}$) and RIN ($\propto P_{opt}^2$) eventually

dominate the noise, depending on the architecture. Balanced detection removes common-mode noise which can often be described as a RIN term; hence, balanced detection architectures are commonly shot-noise limited even for high optical powers. The single-drive, single detection case of Figure 39(c) clearly illustrates the transition from output thermal to shot noise to RIN limited regimes for increasing optical power, while its balanced detection counterpart remains shot noise limited at high powers. In terms of the noise floor, the RF photonic link is outperformed for all optical powers (with the assumed component metrics of Table 9) by the balanced detection frequency converting links for two reasons: 1) the frequency converters employ null-biased MZMs that reduce shot noise at the detector, and 2) the balanced detection eliminates common-mode RIN, though the RF photonic link also assumes balanced detection. For single detection, the noise floor is only lower for low optical powers, i.e. when output thermal or shot noise limited.

Note, as mentioned in section 7.3.5, the balanced detection DC photocurrents here are understood to be the sum of the DC photocurrents generated by the individual photodetectors to enable convenient calculation of noise metrics. The I_{DC} of the RF photonic link is largest since quadrature bias is typically employed, while the frequency converter architectures employ null bias, which suppresses the optical carrier and hence a large fraction of the DC photocurrent. These results do not account for photodetector saturation nor nonlinear absorption in fibers or waveguides; hence, the photocurrents (and other metrics) may not scale as indicated for high optical powers. Particularly, integrated platforms, such as SiP and InP, struggle to support optical powers >20 dBm without significant nonlinear effects, though discrete implementations may handle optical powers approaching 30 dBm.

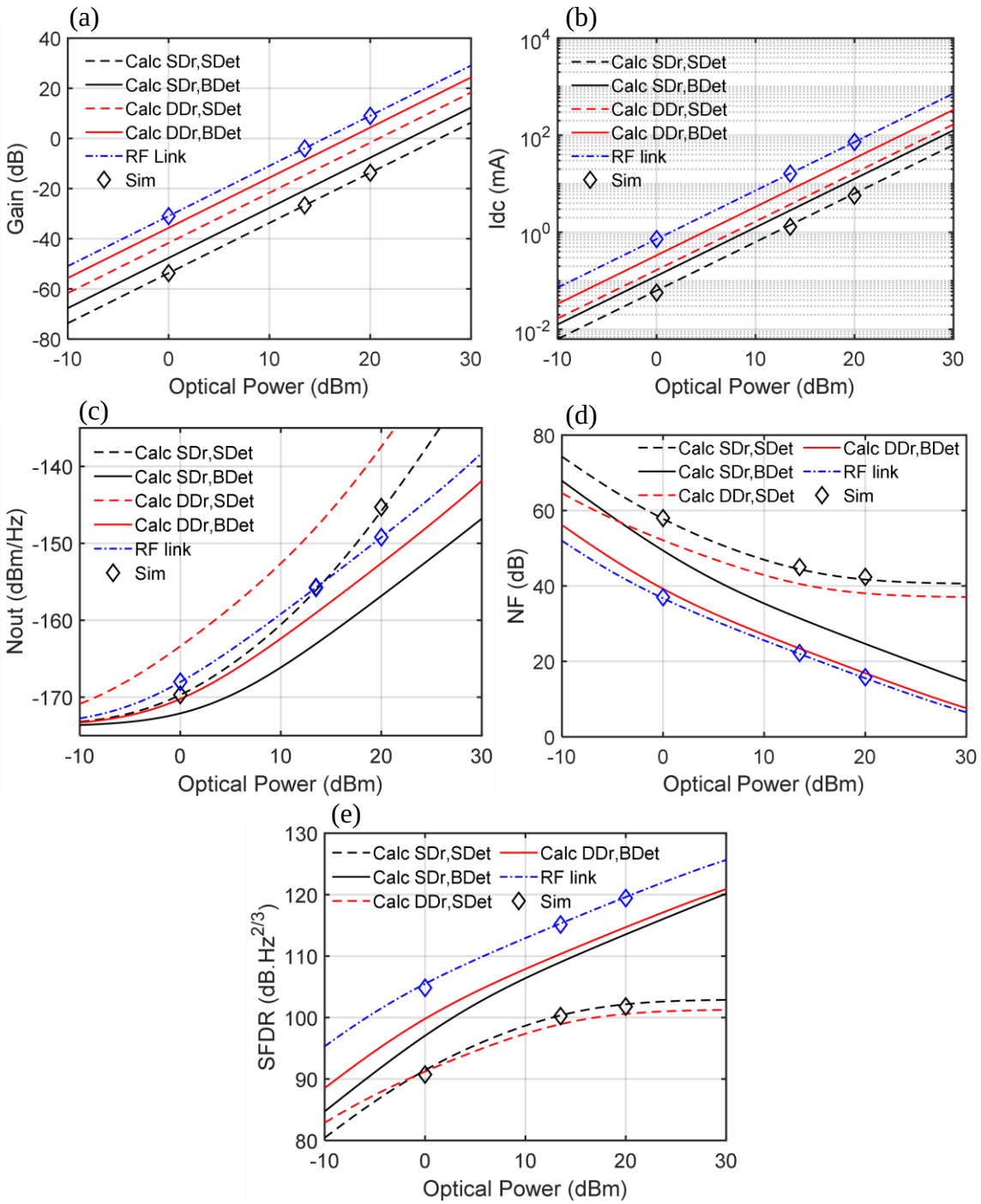

Figure 39 – Calculated (a) gain, (b) I_{DC}, (c) N_{out}, (d) NF, and (e) $SFDR$ versus optical launch power for the four frequency converter architectures and a RF photonic link, all assuming component performance consistent with an InP platform. Additionally, Lumerical-simulated points are indicated for the single drive, single detection, and the RF photonic link architectures, demonstrating fidelity with the calculated results. SDr = single drive, DDr = dual drive, SDet = single detection, BDet = balanced detection.

Likewise, the NF reflects similar dependence on the dominant noise source, Figure 39(d). When output thermally limited, the architecture and RF photonic link NFs drop quickly with increased optical power with slope = -2 on a decibel scale. The rate of NF improvement drops as the shot noise regime (slope = -1) is entered, and when RIN becomes dominant a floor in the NF is formed (slope = 0) as the noise power increases at the same rate as the signal power. Hence, avoiding the RIN limited regime is vital to scale performance via high optical power. Although the noise floor for the balanced RF photonic link was typically worse than for frequency converters employing balanced detection, the RF photonic link's NF is lower across all optical powers. The RF photonic link NF is overall superior despite a higher noise floor since its gain is higher. The dual-drive, balanced detection frequency converter architecture exhibits the best NF among the frequency converters, nearly as good as the standard RF photonic link for all optical powers. This architecture exhibits NFs < 20 dB for optical launch powers ~17 dBm (50 mW). Although the N_{out} of single-drive schemes outperformed dual-drive schemes, the latter exhibits significantly better NFs due to the effective halving of the MZM V_{π}, which improves gain.

Lastly, $SFDR$s exhibit similar limitations as the NF for RIN-dominant noise which forms a ceiling on achievable $SFDR$ for single detection architectures, Figure 39(e). Increased optical power benefits the $SFDR$ greatest in an output thermal noise limited regime, and to a lesser degree in the shot noise limited regime. Balanced detection architectures can achieve $SFDR$s greater than 110 dB·Hz$^{2/3}$ with launch powers greater than +13 dBm.

For the single detection results of Figure 39(e), the single-drive $SFDR$ exceeds the dual drive $SFDR$ for high optical powers. The dual drive implementation exhibits a larger I_{DC}, resulting in higher shot noise and RIN that lowers the ceiling on the RIN-limited $SFDR$. Hence, the single drive implementation achieves a higher $SFDR$ at high optical powers since it is less limited by RIN conveyed via the DC photocurrent.

For all metrics, the simulated Lumerical data points match exceedingly well with the analytic results. The frequency domain simulations used component parameters that match those assumed by the analytic responses, Table 9.

7.3.9 Idealized Results

Next, the analytic equations are employed again to predict future performance of photonic frequency converters for a generalized x-axis, where the total link optical power budget $P_0 + G_{opt}$ is introduced. Here, G_{opt} is $10\log_{10}(g_{opt})$ and is the dB scale version of the total link optical gain or loss from laser to detector. P_0 is the optical launch power in dBm; hence the total optical power budget $P_0 + G_{opt}$ has units of dBm. This metric is useful because it enables simple determination of the optical launch power, optical amplifier gain, and loss budget required for target performance, or conversely the expected performance given those optical parameters. The following results assume otherwise ideal conditions and parameters, namely negligible RIN and a modulator $V_\pi = 1$ V; however, the following results are not strict upper limits on performance. For example, lower V_π's may be available in the future. Also, perfectly linear modulator phase shifters are assumed here, which are suboptimal when using MZMs, since they do not counteract the cosine transfer function of the interferometer which generates performance-limiting nonlinearities. Ideally, these

phase shifter responses would be arccosine functions to yield an overall linear MZM response. Hence, modulator linearization schemes will violate the trends described shortly.

The idealized gain, NF, and $SFDR$ results are given in Figure 40 and generally exhibit the same trends as previously noted. However, the effects of RIN are not present, since the RIN is assumed small. The dual-drive, balanced detection architecture still maintains the best overall performance and achieves unity gain, a NF of 14 dB, and 109 dB·Hz$^{2/3}$ $SFDR$ for $P_0 + G_{opt} = 10$ dBm without any electrical amplification. This optical power budget is easily achieved in discrete implementations, and not out of reach of integrated platforms, particularly those with on-chip gain like InP. For example, if $P_0 = 13$ dBm, MZM insertion loss is -5 dB, excess splitter and waveguide loss is -3 dB, and the optical amplifier gain is +5 dB, then $G_{opt} = -3\ dB$ and hence $P_0 + G_{opt} = 10$ dBm. The most difficult component performance assumption for integrated platforms is the 1 V V_π assumed here. Such low V_π is not yet feasible on silicon nor InP platforms while maintaining low insertion loss, a function of modulator length and absorption per unit length α. Typical high-performance SiP and InP modulators exhibit $V_\pi L\alpha$ metrics of 20 V·dB [65]. Therefore, a SiP or InP with $V_\pi = 1\ V$ would exhibit a high insertion loss (αL) of 20 dB without further innovation in phase shifter design. On the other hand, the $LiNbO_3$ platform has demonstrated $V_\pi L\alpha$ metrics as low as 6 V·dB, enabling $V_\pi = 1$ V modulators with reasonable insertion losses of 6 dB [67]. Regardless, any reduction of V_π is typically of benefit to both RF photonic links and frequency converters by improving NF and gain.

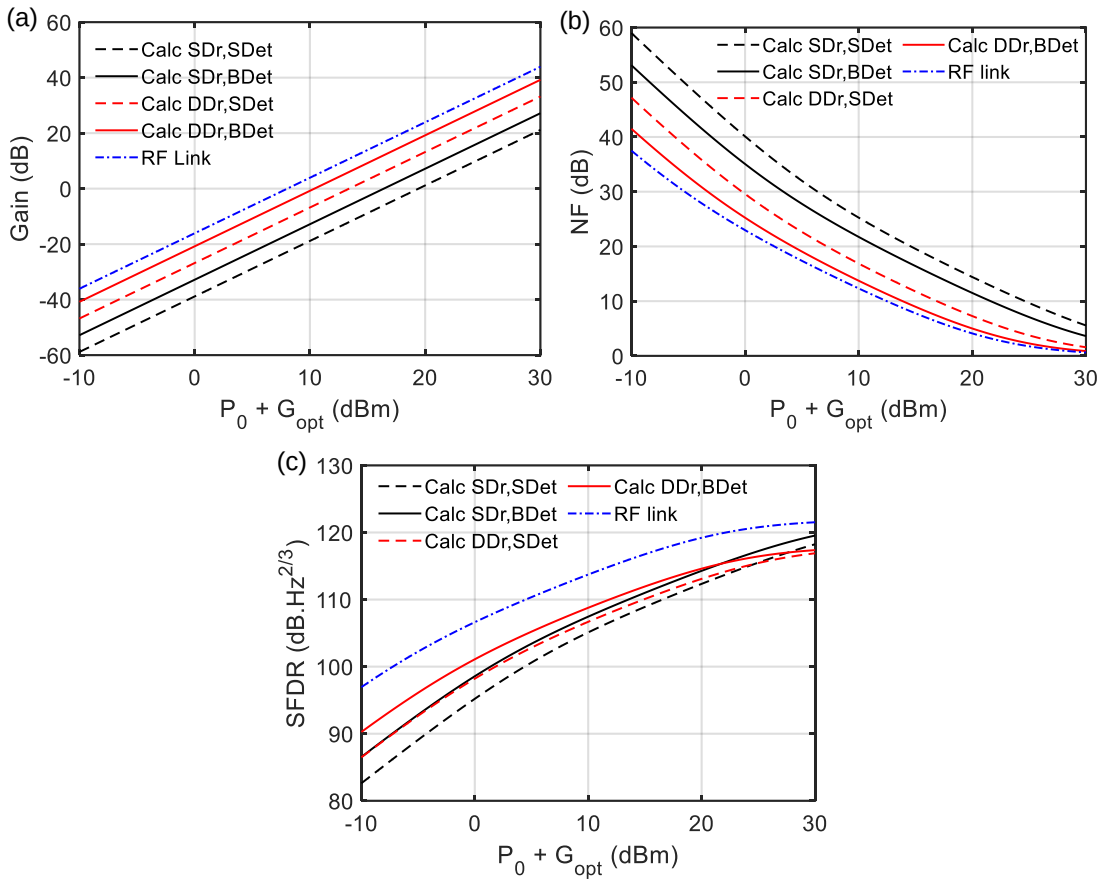

Figure 40 – Calculated (a) gain, (b) NF, and (c) $SFDR$ versus launch power (P_0) modified by optical link gain or loss (G_{opt}) for idealized implementations of the four frequency converter architectures of Figure 36 and a simple RF photonic link. Assumptions include no RIN, no optical loss (or gain), and a modulator $V_\pi = 1$ V. The x-axis enables a designer, knowing the optical power available to them along with an estimate of link loss, to estimate performance of an architecture of interest.

Lastly, mention of some apparent anomalies are explained. The single drive $SFDR$s of Figure 40 exceed the $SFDR$s of the dual drive cases for very high optical power budgets >25 dBm. Because there is no RIN, the explanation of a similar phenomenon in the previous subsection does not apply. Here, the higher gain of the dual drive architectures reaches a noise regime limited by *input* thermal noise, while the single drive architectures remain in the shot noise limited regime for the same optical power budget. Similar to RIN-limited effects, dominant input thermal noise will flatten the $SFDR$ and form a ceiling for

the system dynamic range. Fortunately, only links with exceedingly large gain (very low modulator V_π and high optical power) are likely to be input thermal noise limited.

A useful method for assessing MWP system performance is the $SFDR$ vs. NF design chart popularized by Urick *et al.* [85]. The $SFDR$ is calculated for contours of modulator V_π and link I_{DC} versus NF. However, in the case of frequency converting links employing null-biased MZMs, the $SFDR$ is calculated for varied optical power budget $P_0 + G_{opt}$ (in dBm) instead of I_{DC}.

The design charts for single-drive and dual-drive architectures using single detection are shown in Figure 41, giving a designer the ability to quickly assess linearity and noise performance for a given V_π and optical power budget. The possible $SFDR$s and NFs exist where V_π and $P_0 + G_{opt}$ contours intersect. When RIN dominates the noise, the $P_0 + G_{opt}$ contours will approach a ceiling, which thereby limits the achievable $SFDR$. Close observation of these design charts concludes that while reducing V_π indefinitely benefits NF, the system $SFDR$ is unchanged except for extremely low V_π's that can reduce $SFDR$.

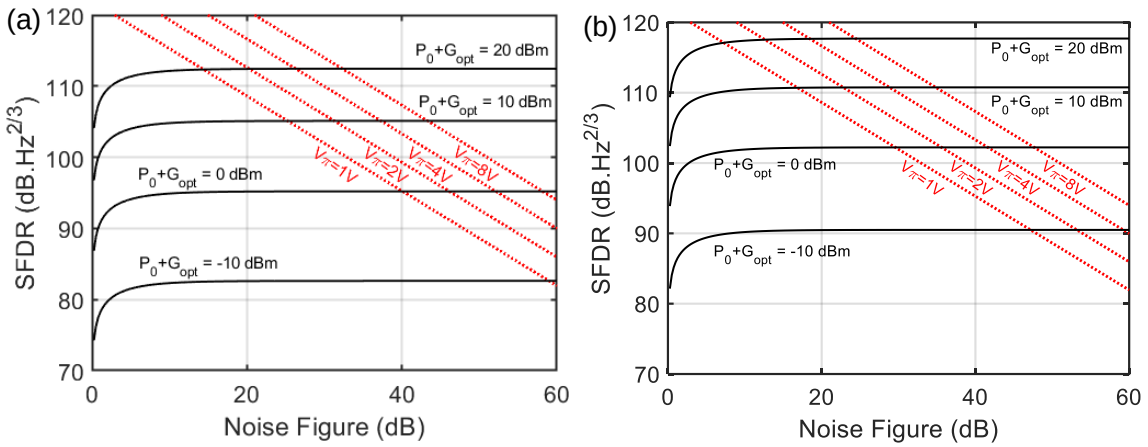

Figure 41 – Calculated trade space for the idealized (a) single drive, single detection and (b) dual drive, single detection architectures, illustrating the effects of increased optical power and V_π on achievable $SFDR$ and NF. Dashed lines indicate contours of constant V_π while solid lines indicate contours of constant optical power, in terms of launch power P_0 and the link's optical gain or loss, G_{opt}. Viable design points for explicitly shown V_π and $P_0 + G_{opt}$ combinations exist where dashed and solid lines intersect.

7.3.10 Comparison to RF Photonic Links

Generally, the main performance trends for RF photonic links also hold for frequency converting links, namely how gain, $SFDR$, and NF scale with optical power, loss, modulator V_π, and other component metrics. Nonetheless, RF photonic links generally outperform photonic frequency converting links for a given optical power, as evidenced by the results of Figure 40, where a dual-drive, balanced detection RF photonic link is compared with a dual-drive, balanced detection frequency converting link. Comparing the gain responses of Figure 40(a) indicates an inherent -4.6 dB gain penalty for frequency converting links. The frequency converter $SFDR$ incurs a -6.7 dB·Hz$^{2/3}$ penalty in the thermal noise limit (low optical power); however, this penalty decreases to -4.1 dB·Hz$^{2/3}$ in the shot noise limit (high optical power). These performance penalties largely originate

from the limited efficiency (gain) of the mixing process and limited optical LO magnitude due to the Bessel function dependence of modulation. After optimization of the LO input power, as was assumed for the derived results of subsection 7.3.6, achieving higher performance rests primarily on increasing optical power or reducing loss.

RF photonic links exhibit NFs no more than -5 dB better than comparable frequency converting links in the input thermal noise limited regime; however, the NFs converge in the shot noise limit. Because the RF photonic link exhibits higher N_{out} due its higher I_{DC} and hence shot noise, the benefits imparted by its superior gain on NF are largely mitigated.

7.3.11 Phase Sensitivities

The phase sensitivities of these frequency converters are important to assess, as such architectures may be implemented in phased arrays and links susceptible to temperature and mechanical drift or shock. The equations of subsections 7.3.6 and 7.3.7 along with Table 8 yield many of the insights into phase sensitivities of the architectures. From these equations, the macro-interferometer phase $\Delta\phi_{int}$ affects all metrics for all four architectures. The gain scales as $cos^2(\Delta\phi_{int})$ because of a phenomenon at the photodetector arising from dual-sideband modulation. The photocurrent generated by mixing the upper sidebands ($e^{j(\omega t+\Omega_{RF})}$ and $e^{j(\omega t+\Omega_{LO})}$) adds with phase $\Delta\phi_{int}$ with the photocurrent generated by the lower sidebands ($e^{j(\omega t-\Omega_{RF})}$ and $e^{j(\omega t-\Omega_{LO})}$). Likewise, this $\Delta\phi_{int}$ is also important for the I_{DC} generated, and hence the shot noise, RIN, and $SFDR$. Note that using single-sideband modulation would eliminate this effect and increase the architectures' immunity to phase-drift impairments.

Assuming RF and LO modulators are identical and identically biased, only the dual-drive architectures exhibit link gains dependent on ϕ_{DC}, the MZM bias point. The link gains g_{IF} of single-drive architectures may or may not be functions of ϕ_{DC} since single-drive MZMs are effectively phase modulators with excess carrier power routed and recombined around it. Hence, ϕ_{DC} only affects the output optical carrier power, not the optical sidebands that produce the output IF. Though not affecting the gain, the MZM bias point will impact noise metrics and hence $SFDR$ by somewhat complex functions, since the full I_{DC} expressions of section 7.3.7 are not simple functions of ϕ_{DC}.

If the RF and LO modulators are different, however, the single-drive gains may be functions of ϕ_{DC}. For example, if ϕ_{DC} is applied in the same arm as the RF signal in the RF MZM, but ϕ_{DC} is applied in the opposite arm as the LO in the LO MZM, the link gain will be tuned with ϕ_{DC}. This would occur because ϕ_{DC} will shift the optical phases of the RF generated optical sidebands, but not the LO generated optical sidebands, resulting in a phenomenon similar to that described for the impact of $\Delta\phi_{int}$. However, as long as ϕ_{DC} is applied in the same arm for *both* single-drive RF and LO MZMs, the gain will be agnostic to MZM bias point.

For dual-drive architectures, the MZM bias point ϕ_{DC} will affect the gain, no matter where the DC phase shift is applied in the MZM. This occurs because signal sidebands are generated in both arms of the MZMs; hence, these sidebands interact as a function of the relative phase when recombined, leading to $g_{IF} \propto cos^2(\phi_{DC})$. Likewise, ϕ_{DC} will affect all other metrics, including N_{out}, NF, and $SFDR$ according to $I_{DC}(\phi_{DC})$ in section 7.3.7.

7.4 Summary

In this chapter, the most comprehensive treatment of photonic frequency converters was presented. Here, an intuitive understanding of how frequency converters operate was given, followed by derivations of useful equations for the key MWP metrics of interest. These analytic equations serve to guide designers of both discrete and integrated photonic frequency converters and predict performance based on known component performance. The equations also yielded information on the scaling of performance with component performance metrics, parameters, and bias points for optimization of such architectures. Lastly, details on how frequency converters compare with intensity-modulated, direct-detect RF photonic links and the phase sensitivities of the photonic frequency converters were expounded. In Chapters 8 and 9, frequency converters built on SiP and InP platforms are experimentally characterized.

CHAPTER 8. SILICON PHOTONIC FREQUENCY CONVERTERS

In this chapter, two SiP frequency converters are simulated via Lumerical INTERCONNECT and experimentally characterized. The simulated and experimentally characterized performance metrics are then compared, validating the simulation tool's ability to accurately predict key photonic frequency converter metrics. The study of two architectures simultaneously instills greater confidence in the simulation methods as well as greater opportunity to assess distinct architectural advantages. Lastly, the two SiP architectures are modified and simulated to predict future performance capabilities of frequency converters on SiP platforms [23].

8.1 Characterization & Simulations

The two SiP architectures ("architecture I" and "architecture II") investigated here are summarized in Figure 42. Architecture I comprises an off-chip laser, integrated phase modulators (PMs) within a larger macro-interferometer, thermal phase shifters to set the bias point of the macro-interferometer, and a photodetector off-chip. While the laser is inevitably off-chip for all SiP implementations, this architecture may be called "partially integrated" since its detection is also off-chip. The phase modulators of architecture I were custom-designed in the AIM Photonics SiP process; a top-down image of the integrated portions of architecture I and a schematic of the custom-designed phase shifter cross-section are given in Figure 43 [3]. The 1 mm phase shifters employed PiN junctions shifted laterally such that P-dopants occupied 50% of the waveguide width compared to 40% for the N-dopants for greater phase-shifting efficiency and lower loss [42]. Further information on the performance of these phase shifters and the detector is given in [23].

Architecture II, Figure 42(b), is comprised of a single off-chip laser, two MZMs within a macro-interferometer, thermal phase shifters for setting the macro-interferometer bias point, and on-chip balanced detection. This architecture is considered “fully integrated” since all components able to be integrated on silicon were integrated. Though the balanced detectors were integrated in architecture II, the electrical subtraction through a balun was accomplished off-chip such that each detector could be independently tested. Though architecture II was also fabricated in the AIM Photonics process, the modulators and detectors are not identical between the two architectures (e.g. the modulators are different in design and performance); hence, direct comparison of these two architectures is not useful. Instead, these two distinct architectures with their unique components are characterized and simulated to prove the predictive capabilities of the simulation tools. Following, these validated simulations predict the performance for improved architectures, informed by the beneficial aspects and drawbacks of the two architectures of Figure 42.

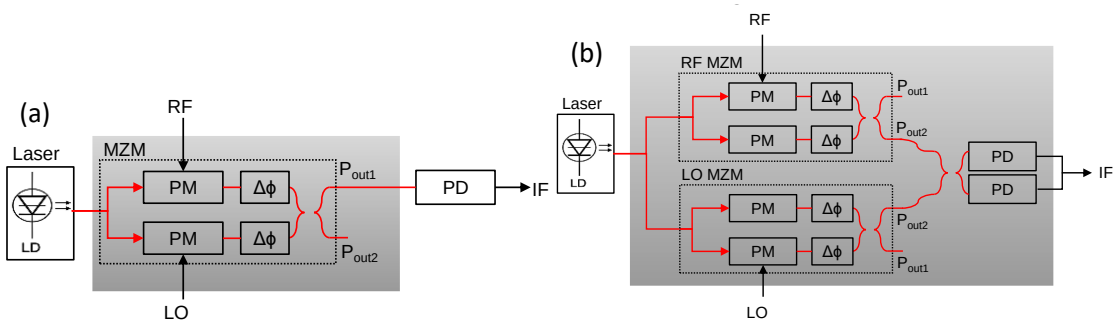

Figure 42 – Schematics of MWP mixer subsystems for (a) architecture I, consisting of a single MZM with separate LO and RF arms and off-chip single-ended detection, and (b) architecture II, consisting of nested MZMs, each single-driven and using on-chip balanced photodetection. PM = Phase modulator, $\Delta\phi$ = thermal phase shifter, PD = photodiode. Optimum bias of each MZM must be carefully considered.

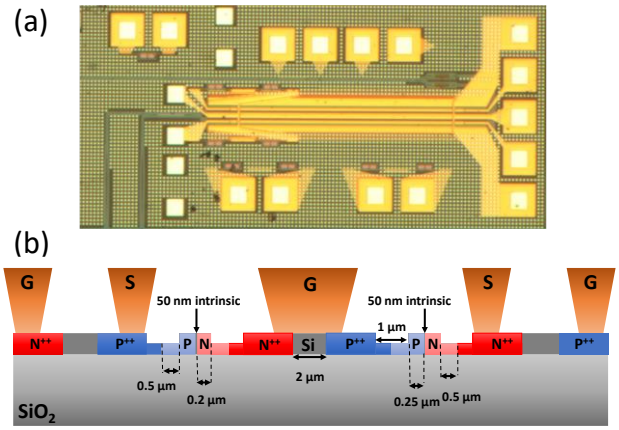

Figure 43 – (a) Top-down image of the fabricated custom-designed modulator using the AIM Photonics platform. (b) Schematic cross-section of the electrode and dopant structure of the designed modulator.

8.1.1 System-Level Simulations

Lumerical INTERCONNECT was used for system-level simulations to accomplish two main goals: 1) to validate the accuracy of simulations compared to experiment, and 2) to predict the performance of new architectures leveraging both architectural modifications and improved component-level performance. Throughout the next subsection, the simulation and experimental results are provided simultaneously. The Lumerical models of various components are informed by measured results, where possible, and otherwise defer to PDK specifications. For example, measured index responses were used to capture nonlinearities and imperfections of the plasma-dispersion based phase modulators. Additionally, the electrical parameters of the modulators were included in simulations, such as experimentally determined characteristic impedances and termination impedances. All electrical sources assume thermally limited noise floors of -174 dBm/Hz. The experimental laser used in both architectures exhibited +20 dBm optical output power, relative intensity noise (RIN) of -145 dBm/Hz, and linewidth of 100 kHz, all specifications included the Lumerical laser model. All other parameters included in the simulation match those experimental values specified throughout this chapter, which include receiver

responsivities and bandwidths, electrical filter and modulator bandwidths, fiber-to-chip optical losses, electrical and optical amplifier gains and noise figures, modulator reverse biases, etc.

8.1.2 Experimental and Simulation Results

The test setups for the characterization of architectures I and II are given in Figure 44. Both setups comprise a C-band laser tuned to 1550 nm, high output power EDFA (up to +30 dBm), variable optical attenuator (VOA) for linear optical power control, polarization controller (PC), two signal generators for RF and LO tone sources, 1 GHz low pass filters and 38 dB electrical amplifier on the detector output, and electrical spectrum analyzer. The average optical I/O loss in coupling to and from the silicon chip was 4.2±0.5 dB. The bias tees coupled -3.5V DC to reverse bias the modulator phase shifters to reduce absorption and junction capacitance. The largest difference between the two test setups is the use of a balun in Figure 44(b), since architecture II uses balanced detection that requires off-chip subtraction of the two detector outputs.

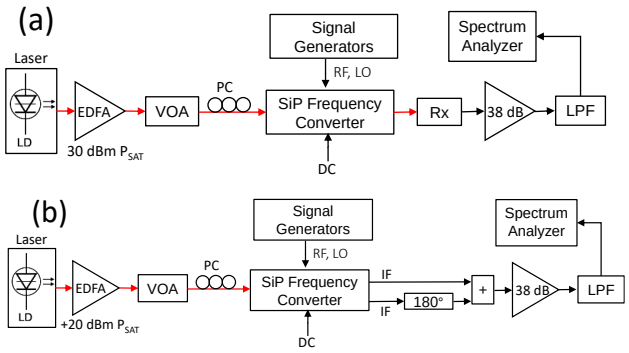

Figure 44 – Schematics of the test setups for (a) architecture I and (b) architecture II. The test setup for architecture II includes an external balun since the balanced detector outputs were not subtracted on-chip to enable characterization of each detector separately.

The basic functionalities of architectures I and II were verified by measurement of a 100 MHz IF, for RF and LO tones as indicated in Figure 45. Architecture I was tested using RF

and LO tones at 5.0 GHz and 5.1 GHz, respectively. Architecture II was tested using RF and LO tones at 10.0 GHz and 10.1 GHz, respectively. In both responses, the low-pass electrical filters (LPFs) significantly attenuate the RF fundamental, LO fundamental, high frequency noise, and other spurious signals. The results of Figure 45 are raw measurements, unadjusted for losses in cables, bias tees, electrical combiners, and RF probes; the precise RF-to-IF gain will be assessed shortly.

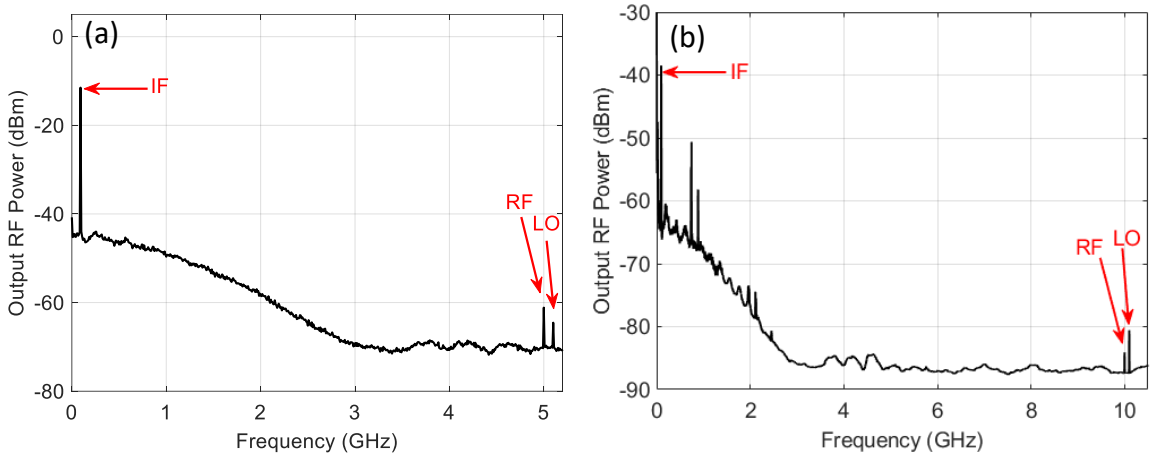

Figure 45 – Measured spectra demonstrating downconversion for (a) architecture I and for (b) architecture II. The 1 GHz lowpass filter strongly attenuates signals beyond 2 GHz. Relative comparison of IF power between (a) and (b) are not straightforward in these uncalibrated results. The calibrated RF-to-IF gains are -5.0 dB and -19.5 dB for (a) and (b), respectively.

Next, because each architecture contains interferometers, the bias point can be optimized experimentally in terms of the RF-to-IF gain metric. The thermal phase shifter of architecture I was swept while monitoring optical output power and again while measuring IF power from the photodetector. The calibrated responses of Figure 46 demonstrate maximal performance at both peak and null biases, with a maximum IF gain of -5.0 dB achieved at peak transmission. Here, the optical transmission response (red) was measured with no AC modulation. The measured range of gains between optimum and minimum points exceeded 40 dB; hence, the IF gain is very sensitive to the relative phases of the RF

and LO modulated sidebands, in agreement with the cos ($\Delta\phi_{int}$) dependence from section 7.3.11.

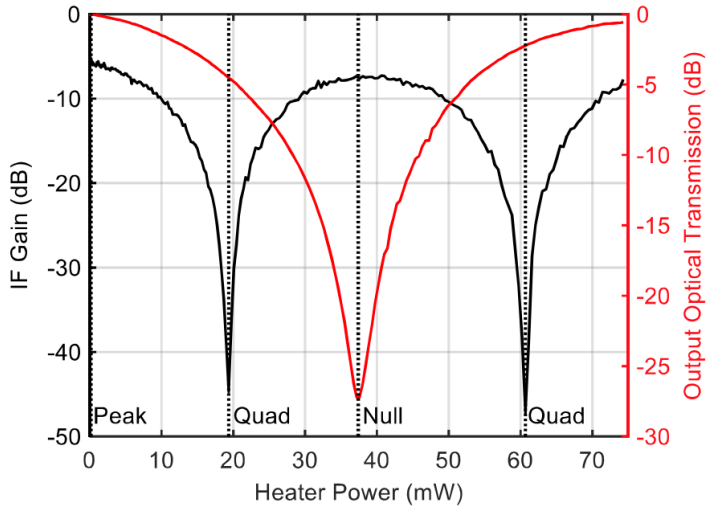

Figure 46 – Measured IF gain of architecture I as a function of thermal phase shifter heater power, which alters the macro-interferometer bias point. Useful bias points including peak, quadrature, and null bias are indicated. For this architecture, the IF gain is maximized at both peak and null modulator bias points.

The same measurement was performed for architecture II, with the added difficulty of optimizing over both the macro-interferometer bias and the two MZM biases. As explained thoroughly in the appendix of [23], the optimal bias scheme was one MZM fixed at quadrature bias while the second MZM was set to peak or null transmission, though peak transmission experimentally performed marginally better. This minor gain performance difference between the peak and null bias points is likely due to the nonlinear phase response of the plasma-dispersion phase shifters. Architecture II demonstrated a peak gain of -19.5 dB

Additionally, the IF gain was investigated for architecture I as a function of optical power, giving information both on optimal performance and the power handling capability of the photonic frequency converter. Sweeping the laser output power while measuring the IF gain yields the response of Figure 47. The discrete derivative $\Delta P_{IF}/\Delta P_{opt,in}$ (ratio of

change in IF power to change of optical power) indicates that two-photon absorption and free-carrier absorption onset near +10 dBm optical power in the waveguides of architecture I, similar to values found in Chapter 4. The gain response of Figure 47 implies that the frequency converter is still useful with two-photon absorption and free-carrier absorption present, although gain improvements come at a higher price in terms of power consumption.

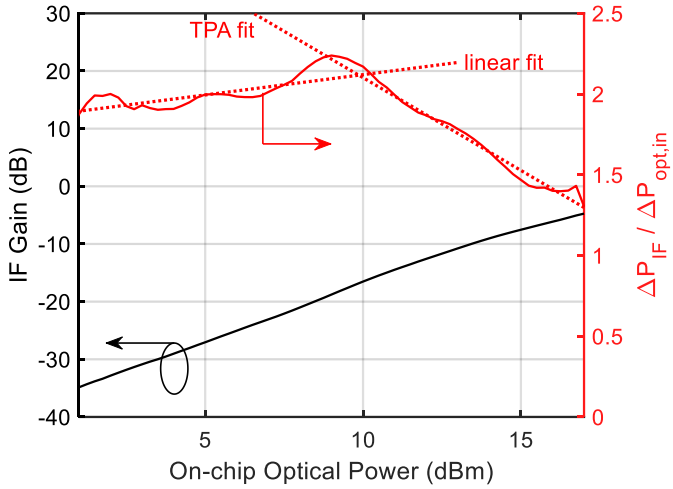

Figure 47 – IF gain response of architecture I and discrete derivative of the IF gain indicating nonlinear absorption at 9.9±0.25 dBm on-chip optical power at λ=1550 nm.

Next, the downconverting bandwidths of both architectures were measured. The bandwidth for frequency converters is defined here as the frequency range over which an RF signal can be downconverted to a fixed IF; hence, the 3 dB bandwidth is measured by sweeping RF and LO tones simultaneously for a fixed IF, in this case 100 MHz. The measured results, along with simulated frequency responses, are shown in Figure 48. Architecture I achieved 3 dB and 6 dB bandwidths of 5.1 GHz and 7.9 GHz, respectively. Simulations overestimated a 3 dB bandwidth of 8.8 GHz, likely due to the simple RC filter models of the simulation tool that fail to capture the complexity of the modulator's equivalent circuit. Better matches in bandwidth could be achieved by using the measured s_{21} responses of characterized modulators. Additionally, small differences in the RF characteristics between

high-speed phase shifters may cause further deviation of experiment from simulation. Although this work has primarily focused on downconversion applications, upconversion is also possible with these same architectures, as demonstrated for architecture I. The upconversion bandwidth was measured by fixing the RF tone at 100 MHz while sweeping the LO source from 600 MHz to 12.1 GHz such that the output IF sweeps from 500 MHz to 12.0 GHz. This result is shown alongside the downconversion frequency response in Figure 48(a), demonstrating a 6.4 GHz 3 dB bandwidth and a 9.1 GHz 6 dB bandwidth. In the upconversion experiment, only the LO path (cables and bias tees) frequency response was calibrated out, since the RF input was fixed at 100 MHz. Upconversion bandwidths are primarily determined by LO modulator and receiver bandwidths, since the RF input frequency is low-speed and fixed.

Architecture II's downconversion frequency response is given in Figure 48(b), exhibiting 3 dB and 6 dB bandwidths of 11.2 GHz and 26.5 GHz, respectively. The simulated 3 dB bandwidth agreed well at 10.7 GHz, but does not well capture the full frequency converter response due to the simplistic modulator RC filter model employed. Note that these bandwidths are electrical-to-electrical bandwidths. The significance of the 6 dB bandwidth is its equivalence to the 3 dB electrical-to-optical bandwidth, due to the square-law behavior of photodetectors. In all downconversion frequency response measurements of Figure 48, the cable and bias tee frequency responses were calibrated out. In downconversion, the modulators primarily limit the system bandwidth, since the IF is typically low-speed (< 1 GHz), rendering the photodetector's (and subsequent circuitry's) frequency response of little consequence.

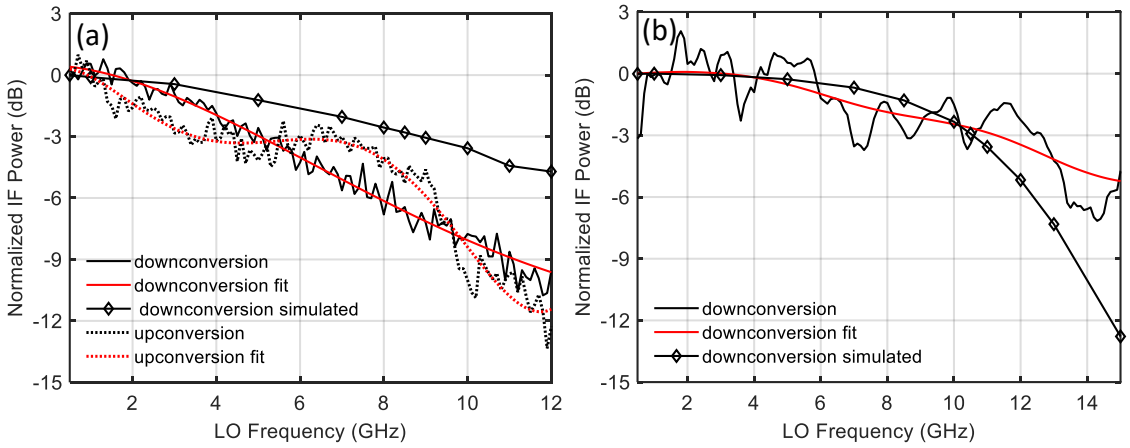

Figure 48 – (a) Measured and simulated frequency responses of architecture I. The measured and simulated 3 dB electrical-electrical downconversion bandwidths were 5.1 GHz and 8.8 GHz, respectively. The measured upconversion bandwidth was 6.4 GHz. (b) Measured and simulated downconversion frequency responses of architecture II. The measured and simulated electrical-electrical 3 dB bandwidths were 11.2 GHz and 10.7 GHz, respectively.

Finally, the linearity metrics of architectures I & II are quantified by an equal-amplitude, two-tone test with RF tones at 1.4 GHz and 1.5 GHz and the LO at 1.0 GHz. This generates fundamental IF tones at 400 MHz and 500 MHz and IMD3 tones at 300 MHz and 600 MHz. The RF input powers were swept while the IF fundamental and IMD3s were monitored via an electrical spectrum analyzer, Figure 49. The measured $SFDR$s of architectures I and II were 91±1 dB·Hz$^{2/3}$ and 92±1 dB·Hz$^{2/3}$, respectively. Similarly, the Lumerical-simulated results of 91.2 dB·Hz$^{2/3}$ and 90.1 dB·Hz$^{2/3}$ are shown alongside the measured results for comparison, demonstrating good agreement. Although the frequency converters differ both in architecture and component performance, tradeoffs in the system level metrics of gain and noise floor result in similar $SFDR$s for architectures I and II.

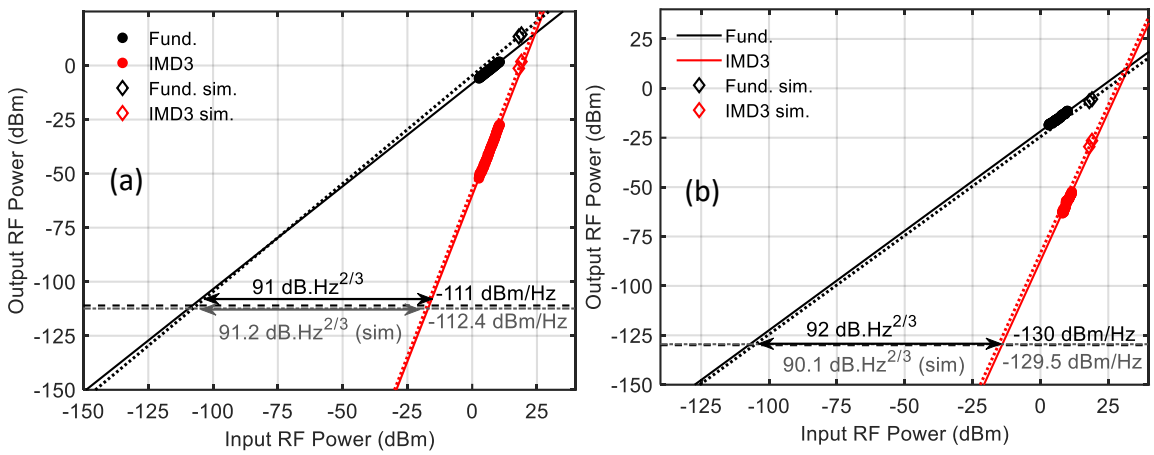

Figure 49 – Measured $SFDR$s by an equal-amplitude two-tone test for fundamental frequencies at 1.4 GHz and 1.5 GHz and a 1.0 GHz LO for (a) architecture I and (b) architecture II. The noise floors of -111 dBm/Hz in (a) and -130 dB/Hz in (b) are largely due to the post-photodetection electrical amplification of output thermal noise.

In terms of other linearity metrics, architecture II demonstrated greater linearity with a 32±0.2 dBm $IIP3$ compared to architecture I's 24.5±0.2 dBm $IIP3$. Interestingly, however, architecture II demonstrates a *lower* $OIP3$ than architecture I, 11±0.2 dBm vs. 15.0±0.2 dBm. This counterintuitive result occurs because the $OIP3$ metric combines information of the $IIP3$ and the system gain; hence, because architecture II exhibits a significantly lower gain despite its superior $IIP3$, its $OIP3$ is lower than the $OIP3$ of architecture I. Simulated $OIP3$ and $IIP3$ results are summarized in Table 10, along with all other simulated and measured metrics for these architectures. In conclusion, architecture II demonstrates better linearity via its higher $SFDR$ and $IIP3$ metrics. The photodetectors likely play only a marginal role in the photonic frequency converter system linearity, since the AIM Photonic detectors used here have been demonstrated in links with $SFDR$s exceeding 113 dB·Hz$^{2/3}$ [92]. Additionally, the photodetector and electrical amplifier were operated in linear regimes away from their saturation points, leaving the MZMs as the primary source of nonlinearities. Hence, linearizing the silicon modulators, as addressed in section 6.1, is a key method for improving frequency converter performance.

From the electrical spectrum analyzer, the noise power spectral densities (N_{out}, more colloquially called the "noise floor") are measured, yielding noise floors of -111±0.5 dBm/Hz for architecture I and -130±0.5 dBm/Hz for architecture II. The high noise floors are primarily due to electrical amplification of output thermal noise, ascertained through the Lumerical simulated noise floors of –112.4 dBm/Hz and -128.3 dBm/Hz for architectures I and II, respectively.

Here, the ability for Lumerical INTERCONNECT to accurately simulate frequency converter system performance has been demonstrated, paving the way for using these calibrated simulations to predict improved architectures.

8.2 Predictions for High Performance Architectures

From the results of the previous section and Chapter 7, several improvements to the original architectures I and II may be suggested: 1) implementing balanced detection for common-mode noise suppression, 2) using driver and TIA amplifiers for improved gain and output power, 3) increasing optical power, 4) using push-pull (dual-drive) modulation, and 5) using state-of-the-art integrated components. In this section, these modifications to the original architectures are assumed and simulated to identify reasonable future performance of silicon photonic frequency converters. These modified architectures are depicted schematically in Figure 50. The new architectures are hereon identified as "Modified Architecture I" and "Modified Architecture II". The difference between these two architectures is in their modulators: the former uses single phase modulators, while the latter uses MZMs.

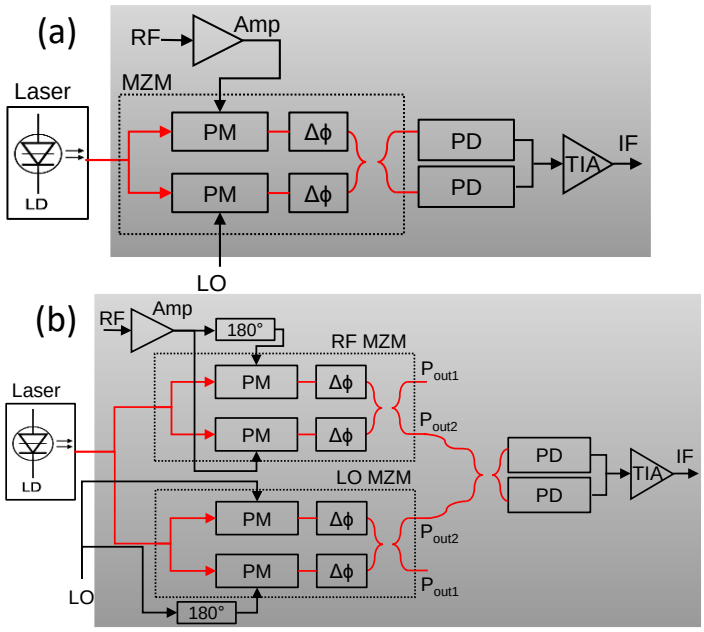

Figure 50 – Schematic of mixers for updated (a) architecture I and (b) architecture II; both architectures now implement on-chip balanced photodetection for noise suppression, an input RF amplifier, and a TIA post-photodetection. Architecture II now uses a dual-drive configuration for both LO and RF MZMs.

The modified architectures assume 35 GHz modulators with V_πs of 7 V, on par with modern foundry capabilities. Amplifiers include 40 GHz, +20 dB gain drivers with up to 2.0 V output amplitude swings on the RF inputs and 10 GHz, 215 V/A TIAs on the outputs of the balanced photodetectors. In fact, a reduced bandwidth on the TIA is advantageous for downconverters by reducing high frequency noise. Optical launch powers were assumed to be +20 dBm from a laser diode; the EDFA was eliminated. Edge coupling losses were assumed (conservatively) at 4 dB/facet. All component values assumed here are matched or beaten by values claimed by existing silicon foundries. The component metrics are summarized alongside all results in Table 10.

The predicted performance for modified architecture I includes a gain of +15.0 dB, a +34.9 dB NF, a 29.1 GHz 3 dB bandwidth, improved $SFDR$ of 98.5 dB·Hz$^{2/3}$, an $IIP3$ of +5.3 dBm, and an $OIP3$ of +23.5 dBm.

Simulations of modified architecture II predict a gain of +20.6 dB, an excellent 25.1 dB NF, 29.1 GHz 3 dB bandwidth, an $SFDR$ of 104 dB·Hz$^{2/3}$, +10.5 dBm $IIP3$, and +30.8 dBm $OIP3$. See Table 10 for summaries of all predicted and measured results. Note, the simulated $IIP3$s appear degraded in comparison to the previous architectures; nonetheless, this reduction in $IIP3$ is the result of using driver amplifiers at the RF inputs and does not indicate reduced linearity. Without considering noise effects, the addition of RF input amplifiers effectively shift the RF input power range over which the system maintains a specified linearity, e.g. an $SFDR$. Here, input amplifiers and TIAs were assumed perfectly linear, because the well-matched simulation and experimental results of the original architectures imply the amplifier nonlinearities are insignificant in comparison to the modulator nonlinearities.

This chapter has highlighted the performance achievable for frequency converters integrated in silicon using architectures and components readily fabricated in foundries as of this writing. SiP-based frequency converters, leveraging balanced detection, integrated drivers and TIAs, dual-drive modulation, and state-of-the-art foundry processes can achieve positive gains, > 100 dB·Hz$^{2/3}$ $SFDR$s, and low noise figures approaching 20 dB. Next, the performance of frequency converters in InP is investigated and compared to the results of this chapter and the broader literature.

Table 10– Summary of Experimental and Simulation Results for Architectures I & II.

	ARCHITECTURE I		MODIFIED ARCHITECTURE I	ARCHITECTURE II		MODIFIED ARCHITECTURE II
Metric	Experimental	Simulated	Simulated	Experimental	Simulated	Simulated
Launch Power (dBm)	20	20	20	20	20	20
Edge coupling loss (dB/facet)	4	4	4	4	4	4
Input RF Amp Gain (dB)	-	-	20	-	-	20
TIA Transimpedance (V/A)	215	215	215	-	-	215
Additional Output Amp. (dB)	38	38	-	38	38	-
MZM V_π (V)	7.0	7.0	7.0	10.5	10.5	7.0
MZM Operation Mode	single-drive	single-drive	single-drive	single-drive	single-drive	dual-drive
Bias Point(s)	Null	Null	Null	Quad, Null	Quad, Null	Null, Null + $\pi/2$
Photodetection Scheme	Single	Single	Balanced	Balanced	Balanced	Balanced
Integration Level	Passives +MZMs	Passives +MZMs	Passives +MZMs +PDs	Passives +MZMs +PDs	Passives +MZMs +PDs	Passives +MZMs +PDs
EE MZM Bandwidth (GHz)	7.5	7.5	35.0	12.1	12.1	35.0
PD Bandwidth (GHz)	30	30	35.0	30	30	35.0
IF Gain (dB)	-5.0	-5.1	+15.0	-19.5	-19.6	+20.6
NF (dB)	+68.0	+66.7	34.9	+62.5	+64.1	25.1
Noise floor (dBm/Hz)	-111	-112.4	-124.1	-130	-129.5	-128.3
Bandwidth (GHz)	5.1	8.8	29.1	11.2	10.7	29.1
SFDR ($dB \cdot Hz^{2/3}$)	91	91.2	98.5	92	90.1	104.0
IIP3 (dBm)	24.5	25.5	5.3*	32	29.4	10.5*
OIP3 (dBm)	15	20.6	23.5	11	5.1	30.8

*Apparent reduction in IIP3 is a result of input amplification and not an indication of decreased linearity.

CHAPTER 9. INDIUM PHOSPHIDE PHOTONIC FREQUENCY CONVERTERS

While the capabilities of photonic frequency converters in a SiP platform were investigated in the previous chapter, the second most popular integrated platform, InP, also shows great promise for IMWP technologies. The InP platform can leverage the semiconductor's direct bandgap to accomplish on-chip lasing and optical gain – a major advantage in the integrated photonics world where high losses are common. In this chapter, an InP photonic frequency converter is designed, fabricated, and characterized. Finally, the InP and SiP platforms are compared regarding their performance for IMWP functions.

9.1 Architecture and Fabrication

The photonic frequency converter architecture implemented here is similar to Architecture II of Chapter 8: a dual-parallel MZM architecture modified to take advantage of InP's inherent gain capabilities, Figure 51. An on-chip distributed feedback laser (DFB) with a monitor photodetector (PD) serves as the optical source, followed by a 2x2 directional coupler providing nominally equal power to both arms of the macro-interferometer. Each arm of the macro-interferometer contains an MZM with output monitor PD, semiconductor optical amplifier (SOA), and thermal phase shifter for adjusting the relative phase between the arms. Due to the quadratic scaling of the IF output power with on-chip optical power, the SOAs are placed behind the MZMs to mitigate modulator insertion losses. The interferometer is terminated by another 2x2 directional coupler, with the top output fed to the highspeed photodetector and the bottom output fed to a (slow) monitor PD. Hence, this

implementation enables real-time monitoring and control of laser output power, MZM bias points, macro-interferometer bias point, and output optical power through the various DC monitor PDs. This is particularly important, as it makes operating the photonic frequency converter unambiguous and enables the characterization of distinct components in the monolithic PIC, particularly the insertion losses throughout the architecture. The monolithic photonic frequency converter was fabricated as a system-on-chip (SoC) through a multi-project wafer offering under AIM Photonics through Infinera's InP foundry process. The InP PIC was attached and wirebonded to a carrier board with breakout DC and RF lines to enable convenient access to all electrical ports, courtesy of Infinera.

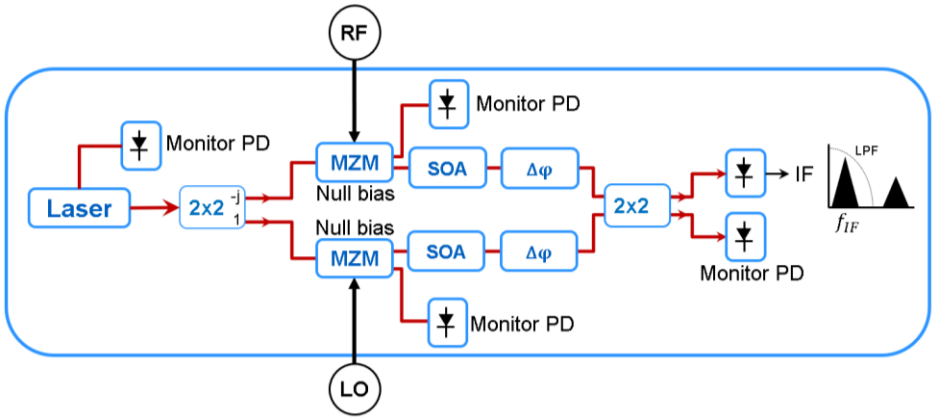

Figure 51 – Monolithically integrated system-on-chip photonic integrated circuit schematic of a downconverter architecture, comprised of on-die laser, two MZMs in parallel followed by SOAs and phase shifters, high-speed photodetector, and multiple low speed detectors for monitoring optical power and bias.

9.2 Experimental Results and Discussion

All measurements, such as gain, downconverting bandwidth, NF, $SFDR$, and other linearity metrics were measured by methods identical in methodology to those described in Chapter 8. Hence, the measurement methodologies are not repeated here, except where major differences occur.

Before measuring the key MWP metrics, the MZMs were null biased using the monitor PDs directly following both RF and LO MZMs. The SOA drive current during these initial measurements was 120 mA, which provides approximately 9 dB optical gain. To measure the gain, a 0 dBm, 1.1 GHz tone served as the input RF signal, while a +17.4 dBm, 1.0 GHz tone served as the LO. For the Infinera modulator with $V_\pi < 5\,V$, this input optical power maximizes the LO-generated optical sideband, which is described by a first-order Bessel function dependence on input voltage. This optimal drive condition is achieved with a driving voltage (peak amplitude) equal to $0.5875V_\pi$. The modulator efficiency's Bessel function dependence, described further in Chapter 7, has a global maximum which is easily achieved for devices with low to moderate V_π's. The 100 MHz IF output was measured via electrical spectrum analyzer and tracked as a function of macro-interferometer bias point to ascertain the optimal bias condition, Figure 52(a). The DC photocurrent from the RF PD was also monitored, as this gives direct information about the macro-interferometer bias point, which can then be compared to the measured IF gain. The results Figure 52(a), which have been calibrated for RF input cable loss, IF output cable loss, and excess electrical loss from bias tees, demonstrate a peak RF-to-IF gain of -26.8±0.2 dB at a quadrature-like bias macro-interferometer bias point, i.e. where the photodetected current and hence incident optical power was -3 dB below its maximum. No external electrical amplifiers were used in this measurement, but this result indicates that the InP frequency converter could easily achieve unity gain with driver amplifiers or a TIA on the photodetected output.

Next, the frequency response of the InP frequency converter was measured with all electrical cable, bias tee, and RF probe responses calibrated out. The frequency response, Figure 52(b), indicates a downconverting 3 dB bandwidth of 10.0 GHz, and a 6 dB

bandwidth of 13.6 GHz. Because this measurement sweeps the frequencies of both RF and LO tones simultaneously while keeping a fixed output IF of 100 MHz, the frequency response falls approximately twice as fast as the frequency response for a single modulator. Hence, this 6 dB point of 13.6 GHz is the approximate modulator bandwidth. From this, a useful rule-of-thumb is intuited: a frequency converter's 3 dB bandwidth will be roughly equal to the 6 dB bandwidth of the modulator used, assuming the LO and RF modulators are identical. Note also that the photodetector bandwidth plays practically no role in the response of Figure 52(b), since the output IF is both fixed and a low frequency (100 MHz). Higher frequency IF's will simply incur a fixed loss according to the photodetector's frequency response during this measurement.

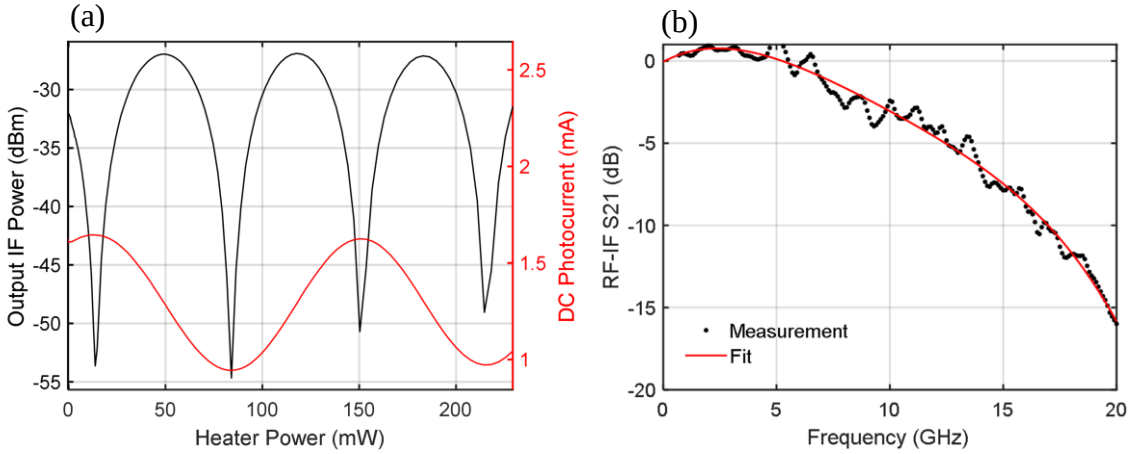

Figure 52 – (a) IF gain and DC photocurrent versus the macro interferometer bias point, controlled by heater power. (b) Downconversion RF bandwidth of 10.0 GHz, measured by sweeping RF and LO frequencies for a fixed 100 MHz IF. Note this downconversion bandwidth includes the responses of both RF and LO modulators; hence, the 6 dB point indicates the InP modulators exhibit 3 dB bandwidths of ~13.6 GHz.

Next, the noise metrics of the InP frequency converter are determined. However, it was found the noise floor was below the electrical spectrum analyzer's noise floor of -152 dBm/Hz, Hence, the true InP frequency converter's N_{out} was measured indirectly using

basic amplifier noise theory. By adding an amplifier to the photodetector output and measuring the new total system's noise factor, the InP PIC's (without amplifier) N_{out} can be estimated. From amplifier theory, the system noise factor F_{sys} is a simple function of the PIC's noise factor F_{PIC} and gain G_{PIC}, as well as the known electrical amplifier's noise factor F_{amp}:

$$F_{sys} = F_{PIC} + \frac{F_{amp} - 1}{G_{PIC}} \qquad 9\text{-}1$$

Recall that $F = 10^{NF/10}$. Hence, knowing F_{amp}, G_{PIC}, and F_{sys}, the term of interest, F_{PIC}, is easily solved for:

$$F_{PIC} = F_{sys} - \frac{F_{amp} - 1}{G_{PIC}}. \qquad 9\text{-}2$$

Then, this F_{PIC} (and its NF_{PIC}) can be used to calculate the PIC's N_{out} via the RF photonic link equation relating N_{out}, NF, and G from Chapter 2:

$$N_{out}\left(\frac{dBm}{Hz}\right) = NF(dB) - 174\left(\frac{dBm}{Hz}\right) + G\,(dB) \qquad 9\text{-}3$$

Hence, the noise metrics are estimated using these equations in conjunction with measurements of the InP PIC with and without an external electrical amplifier on the photodetector output. The N_{out} was estimated at -159.4 dBm/Hz for SOA drive currents of 120 mA. This method of measuring a noise floor below the electrical spectrum analyzer noise floor works as long as the amplified system's noise floor rises above the spectrum analyzer's inherent noise floor limit; otherwise, a larger gain amplifier will be needed.

Next, the $SFDR$ was measured for the InP frequency converter by methods identical to those described in Chapter 8. The two-tone inputs were at 1.4 GHz and 1.5 GHz, and the LO was at 1.0 GHz to produce fundamental tones at 400 MHz and 500 MHz and IMD3 tones at 300 MHz and 600 MHz. The measured $SFDR$ was 99 dB·Hz$^{2/3}$ over an RF input power range between -15 dBm and 0 dBm, Figure 53(a). The resultant $IIP3$ and $OIP3$ were 12 dBm and -18.1 dBm, respectively. The $SFDR$ was then reassessed near 10 GHz, for RF input tones at 10.4 GHz and 10.5 GHz and an LO tone at 10.0 GHz to produce the same IF fundamentals and IMD3s as previously. The 10 GHz experiment yielded a 98±1 dB·Hz$^{2/3}$ $SFDR$ (Figure 53(b)), demonstrating negligible degradation of $SFDR$ over the system's 3 dB bandwidth. The 10 GHz $SFDR$ is valid over a narrower range of RF input power, -8 dBm to 0 dBm, because the IMD3s are closer to the noise floor and hence more difficult to measure. At 10 GHz, the $IIP3$ and $OIP3$ were 19 dBm and -20.2 dBm, respectively. Note that while the $IIP3$ at 10 GHz appears larger than the $IIP3$ at 1 GHz, the $IIP3$ and $OIP3$ measurements are prone to large error bars due to the fitting and extrapolation of limited data.

Next, efforts were directed toward optimizing the system performance, first by increasing the SOA drive current from 120 mA to 150 mA, after which higher drive current no longer benefits performance. The gain, noise metrics, and linearity metrics were remeasured, yielding -26.8 dB gain, N_{out} = -158.9 dBm/Hz, 42.1 dB NF, $SFDR$ of 104±1 dB·Hz$^{2/3}$, $IIP3$ = 12.5 dBm, and $OIP3$ = -17.0 dBm, Figure 54(a).

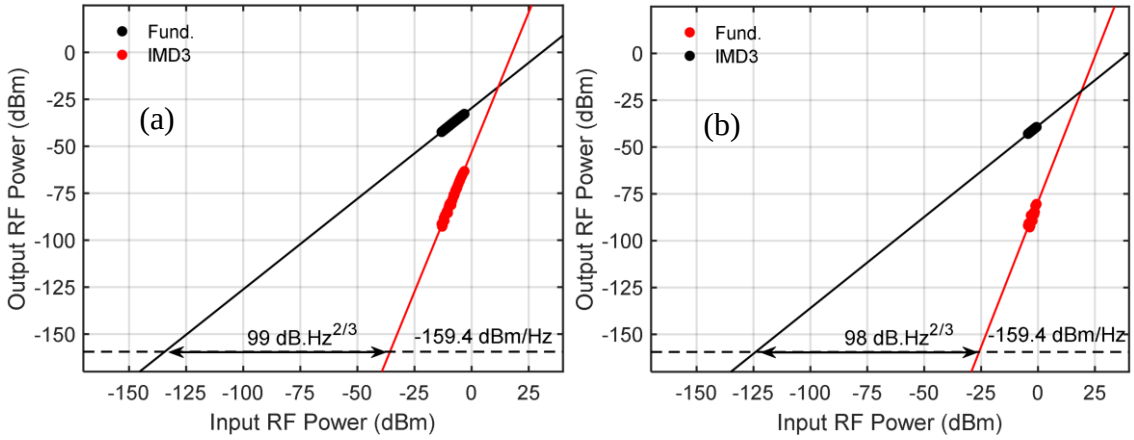

Figure 53 – Two-tone experiments near (a) 1 GHz and (b) 10 GHz. In (a) RF tones at 1.4 GHz and 1.5 GHz and an LO tone at 1.0 GHz demonstrated a 99 dB·Hz$^{2/3}$ $SFDR$ over an RF input power range of roughly -15 dBm to 0 dBm. In (b) RF tones at 10.4 GHz and 10.5 GHz and an LO tone at 10.0 GHz demonstrated a 98 dB·Hz$^{2/3}$ $SFDR$ over an RF input power range of roughly -8 dBm to 0 dBm, a smaller range than in (a) since the IMD3 tones are more difficult to measure due to their proximity to the noise floor. Both experiments yielded fundamental IFs at 400 MHz and 500 MHz, and IMD3 tones at 300 MHz and 600 MHz. Both used SOA drive currents of 120 mA. The $SFDR$ degraded very little over the 10 GHz 3 dB bandwidth.

Lastly, the system performance was characterized with the addition of a 26 dB amplifier on the IF output (SOA current = 120 mA). The InP frequency converter with RF amplifier on the output achieved near unity gain of -0.8 dB, N_{out}= -133 dBm/Hz, a 42 dB NF, an $SFDR$ of 100 dB·Hz$^{2/3}$, a 14 dBm $IIP3$, and a 10.3 dBm $OIP3$, Figure 54(b). With the RF amplifier, the system maintains a high $SFDR$ while achieving near-unity gain, for overall good system performance. The performance metrics of the InP frequency converter under these various operating conditions are summarized in Table 11.

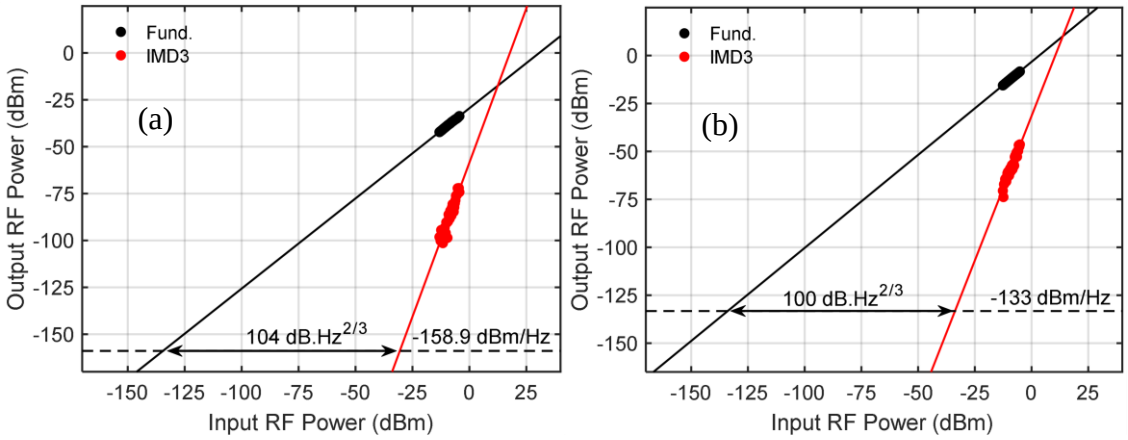

Figure 54 – Two-tone experiments with RF tones at 1.4 GHz and 1.5 GHz and LO tone at 1.0 GHz, yielding fundamental IFs at 400 MHz and 500 MHz, and IMD3 tones at 300 MHz and 600 MHz. (a) The downconverter achieved a 104 dB·Hz$^{2/3}$ $SFDR$ with SOAs driven with 150 mA. (b) The downconverter achieved a -0.8 dB gain and maintained a 100 dB·Hz$^{2/3}$ $SFDR$ when a 26 dB RF amp was added to the detector output.

Table 11– Summary of InP Downconverter Performance for Different Operating Conditions.

	SOA@120mA @ 1 GHz No RF amp	SOA@120mA @ 10 GHz No RF amp	SOA@120mA @ 1 GHz w/ RF amp	SOA@150mA @ 1 GHz No RF amp
Gain (dB)	-26.8	-29.8	-0.8	-26.8
NF (dB)	41.6	44.4	42	42.1
N_{out} (dBm/Hz)	-159.4	-159.4	-133	-158.9
SFDR (dB•Hz$^{2/3}$)	99	98	100	104
RF bandwidth	10.0	10.0	10.0	10.0
IIP3 (dBm)	12	19	14	12.5
OIP3 (dBm)	-18.1	-20.2	10.3	-17.0

9.3 Comparing Experiment to Theory

Here, the analytic equations for the single-drive, single detection architecture from Chapter 7 are employed to compare the experimental results to theory and commercial simulation results. This section validates the accuracy of the analytic equations while simultaneously

identifying the performance trends for the InP frequency converter with increasing optical power.

Using the single-drive, single detection equations of section 7.3.6, the gain and I_{DC} responses versus optical launch power were calculated, Figure 55. Also shown in the figure are results from Lumerical INTERCONNECT simulations for a system matching the experimental frequency converter in terms of component performance and operating points. These simulations (diamonds in figure) were performed at three different laser powers to compare performance over a wide range of power and noise regimes and matched the analytic results closely for both gain and I_{DC}. Also shown are the experimental results described in the previous section 9.2, matching superbly with both the analytic result and the Lumerical simulated points at +13.5 dBm laser power (the experimental laser power).

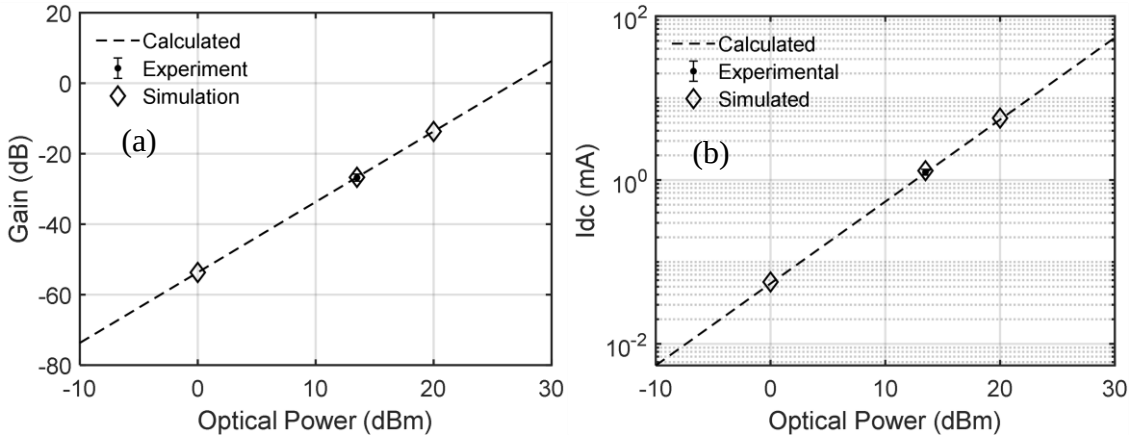

Figure 55 – Calculated, simulated (via Lumerical), and experimental (a) gain and (b) DC photocurrent I_{DC} versus laser launch power for the InP downconverter.

Next, the noise power spectral density N_{out} analytic, simulation, and experimental results are shown in Figure 56. While the results agree well, the analytic results at $P_0 = +13.5$ dBm were overestimated slightly, yielding N_{out} = -156.1 dBm/Hz compared to the

experimentally measured -158.8 dBm/Hz. Likewise, the Lumerical INTERCONNECT simulation also slightly overestimated N_{out}, yielding a value of -155.7 dBm/Hz. Lumerical INTERCONNECT consistently estimated slightly higher NFs compared to the analytic equations across all simulated laser powers, likely due to limited simulation times. Nonetheless, this discrepancy between analytic and simulated results is within 0.5 dBm/Hz. The analytic result was within 3 dBm/Hz of the experimentally measured result.

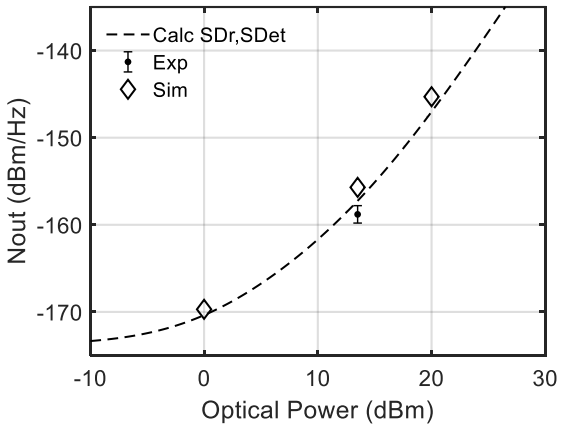

Figure 56 – Calculated, simulated (via Lumerical), and experimental noise floor N_{out} versus laser launch power for the InP downconverter.

Lastly, the NF and $SFDR$ metrics were calculated via the analytic equations and compared with the Lumerical simulations and experimental data, Figure 57. The small discrepancy between analytic and experimental N_{out} also causes further discrepancy in the NF, with the analytic result predicting NF = 44.4 dB compared to the experimentally measured 41.6 dB. The Lumerical NF (45.0 dB at +13.5 dBm laser power) was slightly higher than the analytic result across the simulated laser powers , as anticipated.

The experimentally measured 99.0 dB·Hz$^{2/3}$ $SFDR$ compares well to the predicted 100.3 dB·Hz$^{2/3}$ per the analytic equation. The Lumerical simulations yielded very good

agreement with the analytic equations, with a simulated $SFDR$ of 100.2 dB·Hz$^{2/3}$ for +13.5 dBm input power.

Hence, this section's results demonstrate the accuracy of the analytic expressions derived previously, as all metrics were found to agree well with both commercial simulation results and experimental data.

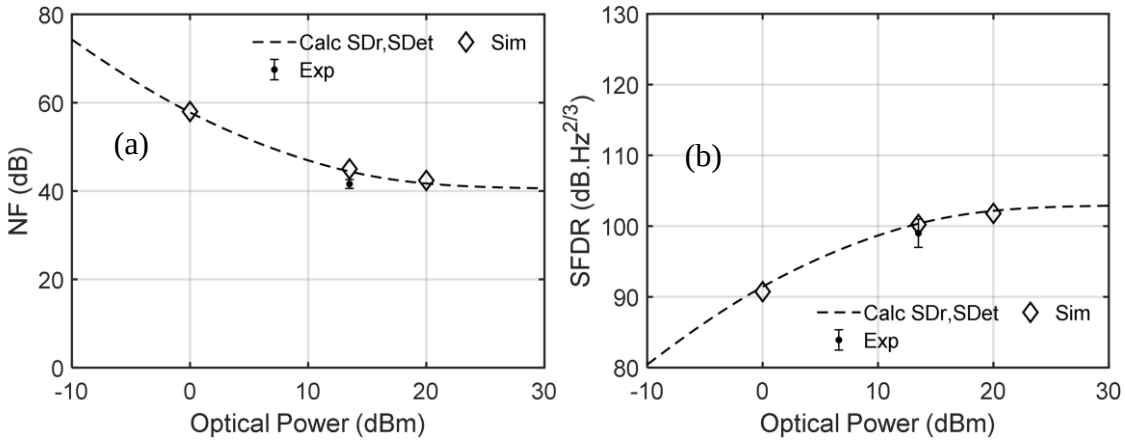

Figure 57 – Calculated, simulated (via Lumerical), and experimental (a) noise figure and (b) $SFDR$ versus laser launch power for the InP downconverter.

9.4 Improving Performance

Despite the strong performance of the characterized InP frequency converter, relatively simple improvements can be made to dramatically improve performance. Taking the measured InP results of section 9.2 as a starting point, the analytic equations of section 7.3.6 can predict how performance will improve through relatively simple architectural changes, such as moving to dual-drive and balanced detection implementations.

As apparent from the NF and $SFDR$ results of Figure 58, the experimentally measured frequency converter was performance-limited due to RIN-dominant noise since the NF and $SFDR$ calculated responses (dashed black) show significant flattening at the experimental

laser output power P_0 = 13.5 dBm. This RIN prevents significant improvement in NF and $SFDR$ for increased optical power >13.5 dBm. Hence, eliminating RIN is key to unlocking the benefits of operating such frequency converters at high optical powers.

Balanced detection is a common solution for eliminating common-mode RIN, such as that originating from the laser. Recalculating the responses with balanced detection assumed (solid black) yields dramatic improvements: a 13 dB reduction in NF and 9 dB·Hz$^{2/3}$ increase in $SFDR$ for the same operating conditions, Figure 58. Additionally, with RIN largely eliminated, performance can continue scaling in the shot noise limit for increased optical power, enabling NFs< 20 dB and $SFDR$s approaching 120 dB·Hz$^{2/3}$.

Furthermore, implementing dual-drive modulation schemes can further improve the NF by reducing the effective MZM V_π. A dual-drive scheme can further reduce the NF, as indicated in Figure 58(a), by another 8 dB for the same operating conditions. This simultaneously increases the $SFDR$ modestly by another 1 dB·Hz$^{2/3}$.

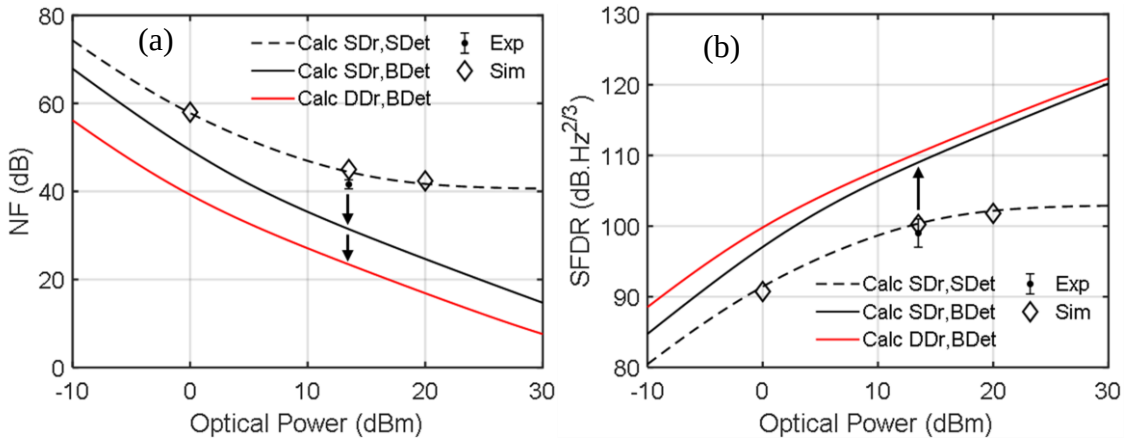

Figure 58 – Calculated, simulated (via Lumerical), and experimental (a) noise figure and (b) $SFDR$ versus laser launch power for single-drive with single detection (dashed black), single-drive with balanced detection (solid black), and dual-drive with balanced detection implementations (solid red).

To conclude, increased performance relies most significantly on eliminating RIN through balanced detection to enable performance to scale with optical power in the shot noise limited regime. Additionally, moving to dual-drive implementations will be necessary for reducing the NF as much as possible. Hence, dual-drive, balanced detection implementations with high powered optical sources could achieve NFs approaching 10 dB and $SFDR$s of 120 dB·Hz$^{2/3}$ without any complex noise reduction or linearization schemes. However, optical power handling of platforms, especially in integrated photonics, must be optimized to achieve aggressive NF and $SFDR$ target metrics.

9.5 Comparing InP and Silicon for Photonic Frequency Converters

Now that both silicon and InP based photonic frequency converters have been investigated, a side-by-side comparison of the two platforms for IMWP applications is useful. Neither platform provides an obvious upper hand; rather the two platforms excel in disparate areas, and choosing between the two will depend on the designer's specific requirements, larger system parameters, cost, and availability.

Because (as Chapters 4 and 7-9 firmly established) optical power is the key metric to achieving high performance, the optical power handling is perhaps the most important point of comparison. Though not the only contribution to nonlinear absorption, the two-photon absorption (TPA) is the primary material property describing inherent optical power handling capabilities. The TPA for silicon of 0.5 cm/GW is significantly lower than that of InP, 25 cm/GW, which lends an inherent superiority for optical power handling to the SiP platform. However, the SiP waveguiding index contrast is significantly larger than the index contrast for InP waveguides, leading to smaller SiP waveguide cross-sections, typically ~500 nm x 200 nm. This is an advantage for compact waveguide routing, but

results in higher optical power density for the same input optical power compared to larger InP waveguides, typically 2000 nm x 200 nm. Hence, to first order, InP platforms have greater cross-sectional area by a factor of four, which aids in increasing optical power handling by spreading the power of the mode over the waveguide area. Thus, the inherently lower optical power handling of the InP platform is at least partially buoyed by the use of larger waveguides.

Continuing features relevant to achieving high optical power, the InP platform offers on-chip lasing and gain, which both eliminates the need for lossy (1-3 dB) off-chip coupling and offers an ability to mitigate insertion losses with on-chip SOAs. Hence, while InP waveguides may not handle quite as much average optical power as SiP waveguides, the optical link budget is more manageable with InP.

One drawback of InP is relatively poor electrical isolation between components which requires further engineering to increase and prevent crosstalk between nearby electrical components. This also makes engineering the RF properties of high-speed electrodes more flexible in SiP. Another benefit inherent to the high-quality oxides available in SiP is better thermal control and isolation, which helps reduce the required electrical power for thermal tuning. As complex PICs can have dozens or even hundreds of thermal tuning elements, the ~10% better efficiency of SiP thermal tuners has a major impact on the scalability of large systems. Furthermore, novel undercut structures have been developed by Globalfoundries in their 90 nm process that further boost the efficiency of SiP thermal tuners, requiring < 3 mW of electrical power for a π phase shift [93].

Lastly, the modulation bandwidths are compared. Thus far, SiP modulators have generally demonstrated larger 3 dB electro-optic bandwidths (> 35 GHz) while InP modulators have demonstrated bandwidths up to approximately 15 GHz, from the experience and observation of several PDKs by the author. Note this does not mean a well-engineered InP

phase shifter cannot exceed this bandwidth and compete with SiP bandwidths; rather, amongst open foundry PDKs, this is merely a typical bandwidth encountered. Proprietary InP modulators likely exceed this quoted bandwidth, but are not currently found in open multi-project wafer PDKs.

A summary of the InP and SiP platform comparison is given in Table 12.

Table 12– Summary Comparing SiP and InP Platforms

SiP	InP	Takeaway
TPA coefficient, β: ~0.5 cm/GW	TPA coefficient, β: ~25 cm/GW	SiP waveguides likely handle higher optical power densities.
Waveguide cross-sectional area~ 200 nm x 500 nm	Waveguide cross-sectional area ~ 200 nm x 2000 nm	InP waveguides cross-sectional areas are roughly 4 times larger, and mitigate InP's power handling penalty due to its TPA coefficient.
No gain on die	SOAs on die offering ~ 10 dB gain, outputs of >10 dBm	SOAs on die greatly benefit the power budget, boosting gain, SFDR, and NF. Regains optical power lost to insertion loss.
Requires optical coupling	Laser on die	Lasers on die avoid 1- 3 dB optical power penalty incurred by coupling losses, further benefiting performance.
Strong oxide insulator	Poor insulators available	SiP has superior electrical isolation. SiP may have increased flexibility in engineering RF and optical group velocities.
Relatively more power efficient thermal tuning (e.g. heater π phase shift requires 40-50 mW)	Relatively less power efficient thermal tuning (e.g. heater π phase shift requires ~50-60 mW)	SiPs may use less power at cost of needing external components (e.g. lasers). InP likely consumes more power, but is monolithic.
Commercial MZM bandwidths > 35 GHZ	Commercial MZM bandwidths ~ 15 GHz	Thus far, SiP MZMs in foundry processes have demonstrated better high-speed performance.

CHAPTER 10. PUBLICATIONS & SUMMARY OF CONTRIBUTIONS TO THE FIELD

10.1 First-Authored Publications

Design Guide for Photonic Frequency Converters
Christian G. Bottenfield, Varghese A. Thomas, Richard DeSalvo, Stephen E. Ralph, *IPC* 2021

Analytic Equations for Photonic Frequency Converter Design
Christian G. Bottenfield, Varghese A. Thomas, Stephen E. Ralph, *JLT* 2021

High Performance Microwave Photonic Downconversion in a Commercial InP Platform
Christian G. Bottenfield, Michael Hoff, Varghese A Thomas, Ardy Winoto, Yuchun Zhou, Ashish Bhardwaj, Gloria E. Hoefler, Richard DeSalvo, Stephen E. Ralph, *OFC* 2021

Synthetic Pockels Modulators in Silicon
Christian G. Bottenfield, Richard DeSalvo, and Stephen E. Ralph, *CLEO* 2021

High-Performance Fully Integrated Silicon Photonic Microwave Mixer Subsystems
Christian G. Bottenfield, Stephen E. Ralph, *JLT* 2020.

A Silicon Photonic Down-converter
Christian G. Bottenfield, Varghese A. Thomas, Gareeyasee Saha, Richard DeSalvo, Stephen E. Ralph, *ECOC* 2019

DC Kerr Effect and Limits for Silicon Photonic Modulators
Christian G. Bottenfield, Varghese A. Thomas, and Stephen E. Ralph, *CLEO* 2019.

Silicon Photonic Modulator Linearity and Optimization for Microwave Photonic Links
Christian G. Bottenfield, Varghese A. Thomas, and Stephen E. Ralph, *JSTQE* 2019.

Microwave Photonic Links: Optimization of SiP Modulator Design and Operation
Christian G. Bottenfield, Varghese A. Thomas, and Stephen E. Ralph, *OFC* 2019.

10.2 Other Publications

Self-Homodyne Photonic Transmitter Conceptual Proof in a Commercial Monolithic InP Platform
Michael T. Hoff, Christian G. Bottenfield, Varghese A. Thomas, Ardy Winoto, Yuchun Zhou, Ashish Bhardwaj, Gloria E. Hoefler, Stephen E. Ralph, *OFC* 2021

Photonic Integrated Circuits for Simultaneous Channelization and Downconversion
Benjamin B. Yang, Brandon Lovelace, Brian Wier, Jacob Campbell, Mark Bolding, Cheong-Wo Chan, J. Glen Vinson, Tarun Muthuchamy, Rajib Bhattacharjea, T. Robert Harris, Kyle Davis, Andrew Stark, Christopher Ward, Christian G. Bottenfield, Stephen E. Ralph, Michael Gehl, Anthony Lentine, *GOMAC* 2021

Multichip Module Development for Radio Frequency Photonic Channelization and Downconversion

Benjamin B. Yang, Brandon Lovelace, Brian Wier, Mark Bolding, J. Glen Vinson, Rajib Bhattacharjea, Tarun Muthuchamy, T. Robert Harris, Kyle Davis, Andrew Stark, Christopher Ward, Christian G. Bottenfield, Stephen E. Ralph, Michael Gehl, Anthony Lentine, *GOMAC* 2020.

CMOS Foundry DRC-Conforming Extended Cladding Modulated Integrated Bragg Grating Filters

Gareeyasee Saha, Christian G. Bottenfield, Patrick S. Goley, John D. Cressler, Stephen E. Ralph, *CLEO* 2019.

A Co-integrated Silicon-Based Electronic-Photonic Wideband, High-Power Signal Source

Saeed Zeinolabedinzadeh, Patrick Goley, Milad Frounchi, Sunil Rao, Christian G. Bottenfield, Stephen E. Ralph, M. Kaynak, Lars Zimmermann, Stefan Lischke, Christian Mai, and John D. Cressler, *OFC* 2020.

Gain, SFDR and NF for Analog Links with with Arbitary Transfer Functions

Stephen E. Ralph, Varghese A. Thomas, Christian G. Bottenfield, Stephen M. Hurst, Gareeyasee Saha, *AVFOP* 2018.

Simulation of Integrated Transmitter with Enhanced Power for Analog RF Links

Varghese A. Thomas, Christian G. Bottenfield, Gareeyasee Saha, Siddharth Varughese, and Stephen E. Ralph, *IPC* 2018.

Photonic Integrated Circuits for RF Electronic Systems

A. Stark, C. Ward, K. Davis, B. Yang, T. Brothers, J. Langston, C. Bottenfield, G. Saha, J. Lavrencik, S.E. Ralph, A. Paollela, C. Middleton, R. DeSalvo, M. Gehl, C. DeRose, A. Lentine, *GOMACTEC* 2018.

10.3 Prior Publications

Investigation of Printing-Based Graded Bulk Heterojunction Organic Solar Cells

Christian G. Bottenfield, Fanan Wei, Hui Joon Park, Jay Guo, and Guangyong Li, Energy Technology, Wiley VCH; 10.1002/ente.201402152, published March 12th, 2015

Lithium Niobate Electro-Optic Racetrack Modulator Etched in Y-Cut LNOI Platform

M. Mahmoud, L. Cai, C. Bottenfield and G. Piazza, *IEEE Photonics Journal*, vol. 10, no. 1, pp. 1-10, Feb. 2018

Fully integrated lithium niobate electro-optic modulator based on asymmetric Mach-Zehnder interferometer etched in LNOI platform

M. Mahmoud, C. Bottenfield, L. Cai and G. Piazza, 2017 *IEEE Photonics Conference* (IPC), Orlando, FL, 2017, pp. 223-224.

Effects of Se Vapor Annealing on Water-based Solution-Processed Cu2ZnSn(S,Se)4 Thin-Film Solar Cells

Minlin Jiang, Quan Tao, Fei Lan, Christian G. Bottenfield, Xingzhong Yan, Guangyong Li**,** *J. Photon. Energy*, 5(1), 053096. 10.1117/1.JPE.5.053096, published February, 27th, 2015.

10.4 Contributions to the Field

The goal of this research is to advance the field of IMWP in achieving spectrally agile systems for next gen fronthaul networks, defense communications, space-based communications, and modern warfighter support. The sum of completed work constitutes significant contributions to the field:

1. Pioneered the linearization of SiP modulator transfer functions by DC Kerr effects, leading to enhanced performance in MWP applications. This work included *a)* Advancing the understanding of nonlinearities generated by SiP modulators. *b)* Advancing the understanding of SiP modulators under large reverse bias conditions; and *c)* Developing rigorous methods of simulating the DC Kerr effect through a combination of commercial software and custom code.
2. Demonstrated analog fiber links using SiP transmitters with >100 dB.Hz$^{2/3}$ $SFDR$ through linearization by DC Kerr effect.
3. Demonstrated a pure DC Kerr effect modulator, acting as a "synthetic" Pockels effect in silicon. Such high linearity, pure phase modulators may be useful for applications including microwave photonics, modulators optimized for higher order modulation formats, and use in quantum gates.
4. Quantified optical power handling in commercial SiP platforms and their limitation of IMWP subsystem performance.
5. Demonstrated the first electrical-in, electrical-out MWP frequency converter on a SiP platform. Additionally, demonstrated the ability of modern simulation tools (e.g. Lumerical) to accurately predict IMWP mixer analog system performance.
6. Developed intuitive expressions for describing the performance and trade space for MWP frequency converting links and verified them by commercial simulations and characterization of an InP based photonic frequency converter.
7. Demonstrated optical edge filters based on TPA-generated free carrier plasma-dispersion effects, exhibiting record-setting filter roll-offs exceeding 10^3 dB/GHz. Concentric ring filter variants also demonstrated few- and sub-GHz optical bandwidths.

REFERENCES

[1] G. T. Reed, W. R. Headley and C. E. J. Png, "Silicon Photonics: the early years," *Proceedings SPIE, Optoelectronics Integration on Silicon II,* vol. 5730, 2005.

[2] "Globalfoundries," [Online]. Available: https://www.globalfoundries.com/.

[3] "AIM Photonics," [Online]. Available: https://aimphotonics.com/.

[4] "IHP Microelectronics," [Online]. Available: https://ihp-microelectronics.com/en/start.html.

[5] V. J. Urick, J. D. McKinney and K. J. Williams, "Applications and Trends," in *Fundamentals of Microwave Photonics*, Hoboken, NJ, USA, Wiley, 2015, p. 423.

[6] A. J. Seeds, "Microwave Photonics," *IEEE Transactions on Microwave Theory and Techniques,* vol. 50, no. 3, 2002.

[7] T. Berceli and P. R. Herczfeld, "Microwave Photonics - a historical perspective," *IEEE Transaction on Microwave Theory and Techniques,* vol. 58, no. 11, pp. 2992-3000, 2010.

[8] J. A. Chiddix, H. Laor, D. M. Pangrac, L. D. Williamson and R. W. Wolfe, "AIM video on fiber in CATV systems need and implementation," *IEEE Journal on Selected Areas in Communications,* vol. 8, no. 7, pp. 1229-1239, 1990.

[9] J. Capmany and D. Novak, "Microwave photonics combines two worlds," *Nature Photonics,* vol. 1, pp. 310-330, 2007.

[10] S. Jin, A. Bhardwaj and P. Herczfled, "RF/Photonic Link-On-Chip PIC," *IEEE Photonic Technology Letters,* vol. 24, no. 13, pp. 1139-1141, 2012.

[11] S. Jin, L. Xu and Y. Li, "A Photonic RF Front-end with Optically Distributed LO and ACP-OPLL," *International Topical Meeting on MWP,* pp. 233-236, 2013.

[12] D. Marpaung and J. C. J. Yao, "Integrated microwave photonics," *Nature Photonics,* vol. 13, pp. 80-90, 2019.

[13] M. Kahn, H. Shen, Y. Xuan, L. Zhao, S. Xiao, D. Leaird, A. Weiner and M. Qi, "Ultrabroad-bandwidth arbitrary radiofrequency waveform generation with a silicon photonic chip-based spectral shaper," *Nature Photonics,* vol. 4, pp. 117-122, 2009.

[14] S. Ristic, A. Bhardwaj, M. J. Rodwell, L. A. Coldren and L. A. Johansson, "An optical phase-locked loop photonic integrated circuit," *IEEE Journal of Lightwave Technology,* vol. 28, no. 4, pp. 526-538, 2010.

[15] K. Balakier, M. J. Fice, L. Ponnampalam, A. J. Seeds and C. C. Renaud, "Monolithically integrated optical phase lock loop microwave photonics," *IEEE Journal of Lightwave Technology,* 2014.

[16] L. Maleki, "The optoelectronic oscillator," *Nature Photonics,* vol. 5, no. 12, pp. 728-730, 2011.

[17] M. Burla, D. Marpaung, L. Zhuang, C. Roeloffzen, M. R. Khan, A. Leinse, M. Hoekman and R. Heideman, "On-chip CMOS compatible reconfigurable optical delay line with separate carrier tuning for microwave photonic signal processing," *Optics Express,* vol. 19, pp. 21475-21484, 2011.

[18] Q. Zhou, A. S. Cross, A. Beling, Y. Fu, Z. Lu and J. C. Campbell, "Highpower V-band InGaAs/InP photodiodes," *IEEE Photonic Technology Letters,* vol. 25, no. 10, pp. 907-909, 2013.

[19] Analog Photonics, "Silicon Photonics," [Online]. Available: https://www.analogphotonics.com/technology/. [Accessed November 2019].

[20] R. Claps, V. Raghunathan and D. Dimitropoulos, "Influence of nonlinear absorption on Raman amplification in silicon waveguides," *Optics Express,* vol. 12, pp. 2774-2780, 2004.

[21] A. Turner-Foster, M. Foster and J. Levy, "Ultrashort free-carrier lifetime in low-loss silicon nanowaveguides," *Optics Express,* vol. 18, pp. 3582-3591, 2010.

[22] A. D. Bristow, N. Rotenburg and H. M. van Driel, "Two-photon absorption and Kerr coefficients of silicon for 850-2200 nm," *Applied Physics Letters,* vol. 90, no. 19, p. 191104, 2007.

[23] C. G. Bottenfield and S. E. Ralph, "High-Performance Fully Integrated Silicon Photonic Microwave Mixer Subsystems," *IEEE Journal of Lightwave Technology,* vol. 38, no. 19, pp. 5536-5545, 2020.

[24] T. Tzu, K. Sun and R. Costanzo, "Foundry-enabled high-power photodetectors for microwave photonics," *IEEE Journal on Selected Topics in Quantum Electronics,* vol. 25, no. 5, pp. 1-11, 2019.

[25] G. P. Agrawal, "Nonlinaer Silicon Photonics," 2012. [Online]. Available: http://ieee-photonics.fr/NonlinearSP.pdf. [Accessed 26 July 2021].

[26] Q. Lin, O. J. Painter and G. P. Agrawal, "Nonlinear optical phenomena in silicon waveguides: Modeling and applications," *Optics Express,* vol. 15, no. 25, pp. 16604-16644, 2007.

[27] C. Ma and S. Mookherjea, "Prospects for photon-pair generation using silicon microring resonators with two photon absorption and free carrier absorption," *OSA Continuum,* vol. 3, no. 5, pp. 1138-1153, 2020.

[28] J. Leuthold, C. Koos and W. Freude, "Nonlinear silicon photonics," *Nature Photonics,* vol. 4, pp. 535-544, 2010.

[29] A. Ghadi and S. Mirzanejhad, "Two-photon absorption effect on semiconductor microring resonators," *Optik,* vol. 126, pp. 1645-1649, 2015.

[30] P. Sah and K. Das, "Integrated Optical Rectangular-Edge Filter Devices in SOI," *Journal of Lightwave Technology,* vol. 35, no. 2, pp. 128-135, 2017.

[31] R. Sumi, N. D. Gupta and B. K. Das, "Integrated Optical Linear Edge Filters Using Apodized Sub-Wavelength Grating Waveguides in SOI," *IEEE Photonics Technology Letters,* vol. 31, no. 17, pp. 1449-1452, 2019.

[32] G. Serafino, C. Porzi, P. Velha, N. Andriolli, P. Ghelfi and A. Bogoni, "40 dB Rejection Sharp-Edge Integrated SOI Phase-Shifted Bragg Grating Filter for Microwave Photonics," in *European Conference and Exhibition on Optical Communications*, Dusseldorf, 2016.

[33] T. Ling, S. Chen and L. J. Guo, "Fabrication and characterization of high Q polymer micro-ring resonator and its application as a sensitive ultrasonic detector," *Optics Express,* vol. 19, no. 2, pp. 861-869, 2011.

[34] C. Xiang, W. Jin, J. Guo, C. Williams, A. Netherton, L. Chang, P. Morton and J. E. Bowers, "Effects of nonlinear loss in high-Q Si ring resonators for narrow-linewidth III-V/Si heterogeneously integrated tunable lasers," *Optics Express,* vol. 28, no. 14, pp. 19926-19936, 2020.

[35] C. Manolatou and M. Lipson, "All-Optical Silicon Modulators Based on Carrier Injection by Two-Photon Absorption," *Journal of Lightwave Technology,* vol. 24, no. 3, pp. 1433-1439, 2006.

[36] Q. Xu and M. Lipson, "Carrier-induced optical bistability in silicon ring resonators," *Optics Letters,* vol. 31, no. 3, pp. 341-343, 2006.

[37] K. Malmir, H. Habibiyan and H. Ghafoorifard, "An ultrasensitive optical label-free polymeric biosensor based on concentric triple microring resonators with a central microdisk resonator," *Optics Communications,* vol. 365, pp. 150-156, 2016.

[38] Z. Zhang, M. Dainese, L. Wosinski and M. Qiu, "Resonance-splitting and enhanced notch depth in SOI ring resonators with mutual mode coupling," *Optics Express*, vol. 16, no. 7, pp. 4621-4630, 2008.

[39] S. K. Korotky, "Dual parallel modulation schemes for low-distortion analog optical transmission," *IEEE Journal of Selected Areas in Communications*, vol. 8, no. 7, pp. 1377-1381, 1990.

[40] W. B. Bridges, "Distortion in linearized electrooptic modulators," *IEEE Transactions on Microwave Theory and Techniques*, vol. 43, no. 9, pp. 2184-2197, 1995.

[41] E. I. Ackerman, "Broad-band linearization of a Mach-Zehnder electrooptic modulator," *IEEE Transactions on Microwave Theory and Techniques*, vol. 47, no. 12, pp. 2271-2279, 1999.

[42] R. Soref, "Electrooptical effects in silicon," *IEEE Journal of Selected Topics in Quantum Electronics*, vol. 23, no. 1, pp. 123-129, 1987.

[43] C. Sorace, "Broadband Linear Silicon Mach-Zehnder Modulators," *IPR Si and Nanophotonics and Photonics in Switching, OSA Tech. Digest*, vol. IWA4, 2010.

[44] J. Ding, "Method to improve the linearity of the silicon Mach-Zehnder optical modulator by doping control," *Optics Express*, vol. 24, pp. 24641-24648, 2016.

[45] S. Yu, "Highly linear silicon Mach-Zehnder modulators with optimized phase-shifter," *2017 International Topical Meeting MWP*, pp. 1-3, 2017.

[46] C. M. Sorace-Agaskar, "Analog Integrated Photonics," *Ph.D. Dissertation, Dept. Electrical Engineering, MIT, Cambridge, MA*, 2015.

[47] X. Xie, "Linearized Mach-Zehnder intensity modulator," *IEEE Photonic Technology Letters*, vol. 15, no. 4, pp. 531-533, 2003.

[48] J. Cardenas, "Linearized silicon modulator based on a ring assisted Mach Zehnder interferometer," *Optics Express,* vol. 21, no. 19, pp. 22549-22557, 2013.

[49] A. Samani, "A Silicon Photonic PAM-4 Modulator Based on Dual-Parallel Mach-Zehnder Interferometers," *IEEE Photonics Journal,* vol. 8, no. 1, pp. 1-10, 2016.

[50] Y. Zhou, "Linearity Characterization of a Dual-Parallel Silicon Mach-Zehnder Modulator," *IEEE Photonics Journal,* vol. 8, no. 6, pp. 1-8, 2016.

[51] Y. Zhou, "Linearity Measurement and Pulse Amplitude Modulation in a Silicon Single-Drive Push-Pull Mach-Zehnder Modulator," *IEEE Journal of Lightwave Technology,* vol. 34, no. 14, pp. 3323-3329, 2016.

[52] M. Streshinsky, "Highly linear silicon traveling wave Mach-Zehnder carrier depletion modulator based on differential drive," *Optics Express,* vol. 21, no. 3, pp. 3818-3825, 2013.

[53] A. M. Gutierrez, "Analytical Model for Calculating the Nonlinear Distortion in Silicon-Based Electro-Optic Mach-Zehnder Modulators," *IEEE Journal of Lightwave Technology,* vol. 31, no. 23, pp. 3603-3613, 2013.

[54] F. Vacondio, "A silicon modulator enabling RF over fiber for 802.11 OFDM signals," *IEEE Journal on Selected Topics in Quantum Electronics,* vol. 16, no. 1, pp. 141-148, 2010.

[55] A. Jain, "Forward bias optimization of a silicon photonic modulator for analog application," in *IEEE AVFOP*, New Orleans, LA, USA, 2017.

[56] A. Khilo, "Broadband linearized silicon modulator," *Optics Express,* vol. 19, pp. 4485-4500, 2011.

[57] E. Dulkeith, "Self-phase modulation in submicron silicon-on-insulator photonic wires," *Optics Express,* vol. 14, pp. 5524-5534, 2006.

[58] O. Boyraz, "Nonlinaer Optics in Silicon," in *Handbook of Silicon Photonics*, Boca Raton, LA, USA, Taylor & Francis, 2013.

[59] E. Timurdogan, "Electric field-induced second-order nonlinear optical effects in silicon waveguides," *Nature Photonics*, vol. 11, pp. 200-206, 2017.

[60] Lumerical Solutions, [Online]. Available: https://www.lumerical.com/. [Accessed January 2021].

[61] N. Hosseinzadeh, "Sources of RF Intermodulation Distortion in Silicon Photonic Modulators," *IEEE AVFOP*, 2018.

[62] C. G. Bottenfield, V. A. Thomas and S. E. Ralph, "Silicon photonic modulator linearity and optimization for microwave photonic links," *IEEE Journal on Selected Topics in Quantum Electronics*, vol. 25, no. 5, pp. 1-10, 2019.

[63] C. G. Bottenfield, V. A. Thomas and S. E. Ralph, "DC Kerr Effect and Limits for Silicon Photonic Modulators," in *Conference on Laseres and Lasers and Electro-Optics*, 2019.

[64] B. Chmielak, M. Waldow, C. Matheisen, C. Ripperda, J. Bolten, T. Wahlbrink, M. Nagel, F. Merget and H. Kurz, "Pockels effect based fully integrated straigned silicon electro-optic modulator," *Optics Express*, vol. 19, pp. 17212-17219, 2011.

[65] X. Tu, T. Liow, J. Song, Y. Mingbin and G. Q. Lo, "Fabrication of low loss and high speed silicon optical modulator using doping compensation method," *Optics Express*, vol. 19, p. 2011, 18029-18035.

[66] M. R. Watts, A. Zortman, D. C. Trotter, R. W. Young and A. L. Lentine, "Low-Voltage, Compact Depletion Mode Silicon Mach-Zehnder Modulator," *IEEE JSTQE*, vol. 16, no. 1, pp. 159-164, 2010.

[67] C. Wang, M. Zhang, X. Chen and e. al., "Integrated lithium niobate electro-optic modulators operating at CMOS-compatible voltages," *Nature,* vol. 562, pp. 101-104, 2018.

[68] H. Tazawa and W. H. Steier, "Analysis of ring resonator-based traveling wave modulators," *IEEE Photonics Technology Letters,* vol. 18, no. 1, pp. 211-213, 2006.

[69] I. Gheorma and R. M. Osgood, "Fundamental limitations of optical resonator based high-speed EO modulators," *IEEE Photonics Technology Letters,* vol. 14, no. 6, pp. 795-797, 2002.

[70] W. Bogaerts, P. De Heyn, T. Van Vaerenbergh, K. De Vos, S. Kumar Selvaraia, T. Claes, P. Dumon, P. Bienstman, D. Van Throughout and R. Baets, "Silicon microring resonators," *Laser and Photonics Review,* vol. 6, pp. 47-73, 2012.

[71] U. Chakraborty, J. Carolan, G. Clark, D. Bunandar, G. Gilbert, J. Notaros, M. R. Watts and D. R. Englund, "Cryogenic operation of silicon photonic modulators based on the DC Kerr effect," *Optica,* vol. 7, no. 10, pp. 1385-1390, 2020.

[72] M. Hossein-Zadeh and K. J. Vahala, "Photonic RF Down-Converter Based on Optomechanical Oscillation," *IEEE Photonic Technology Letters,* vol. 20, no. 4, pp. 234-236, 2008.

[73] C. MIddleton, S. Meredith and R. DeSalvo, "Photonic-based Low Phase Noise Frequency Synthesis for RF-to-Millimeter Wave Carriers and Wideband IF Down-Conversion," in *MILCOMM Conference*, Baltimore, MD, USA, 2011.

[74] E. Chan and R. Minasian, "Microwave Photonic Down-converter with High Conversion Efficiency," *IEEE Journal of Lightwave Technology,* vol. 30, no. 23, pp. 3580-3585, 2012.

[75] Y. Wang, J. Li and T. Zhou, "All-Optical Microwave Photonic Downconverter with Tunable Phase Shift," *IEEE Photonics Journal,* vol. 9, no. 6, pp. 1-8, 2017.

[76] A. Karim and J. Davenport, "High dynamic range microwave photonic links for RF signal transport and RF-IF conversion," *IEEE Journal of Lightwave Technology*, vol. 26, no. 15, pp. 2718-2724, 2008.

[77] T. R. Clark, O. S. R and M. L. Dennis, "A Phase-Modulation I/Q-Demodulation Microwave-to-Digital Photonic Link," *IEEE Transactions on Microwave Theory and Techniques*, vol. 58, no. 11, pp. 3039-3059, 2010.

[78] C. K. Sun, R. J. Orazi and S. A. Pappert, "Efficient microwave frequency conversion using photonic link signal mixing," *IEEE Photonic Technology Letters*, vol. 8, no. 1, pp. 154-156, 1996.

[79] R. Montgomery and R. DeSalvo, "A novel technique for double sideband suppressed carrier modulation of optical fields," *IEEE Photonic Technology Letters*, vol. 7, no. 4, pp. 434-436, 1995.

[80] C. Middleton and R. DeSalvo, "Balanced coherent heterodyne detection with double sideband suppressed carrier modulation for high performance microwave photonic links," *IEEE AVFOP*, pp. 15-16, 2009.

[81] R. DeSalvo and C. Middleton, "System Implementation of coherent analog optical links," *IEEE AVFOP*, pp. 21-22, 2010.

[82] J. Menders, E. Miles, E. Friesema and N. Vallestero, "20 Hz linewidth mm-wave generation by optical sideband filtering," *Proceedings SPIE*, vol. 4112, pp. 91-100, 2000.

[83] M. Poulin, "Ultra-narrowband fiber Bragg gratings for laser linewidth reduction and RF filtering," *Proceedings SPIE*, vol. 7579, 2010.

[84] E. H. W. Chan and A. Minasian, "Microwave Photonic Downconversion Using Phase Modulators in a Sagnac Loop Interferometer," *IEEE Journal on Selected Topics in Quantum Electronics*, vol. 19, no. 6, pp. 211-218, 2013.

[85] V. J. Urick, "Long-haul analog photonics principles with applications," *Doctoral Dissertation, UMI,* vol. 3255815, 2007.

[86] Y. Zhong, L. Zhou and Y. Zhou, "Microwave frequency upconversion employing a coupling-modulated ring resonator," *Photonics Research,* vol. 5, pp. 689-694, 2017.

[87] K. Van Gasse, J. Verbist, H. Li, G. Torfs, J. Bauwelinck and G. Roelkens, "Silicon Photonics Radio-Over-Fiber Transmitter Using GeSi EAMs for Frequency Up-Conversion," *IEEE Photonics Technology Letters,* vol. 31, no. 2, pp. 181-184, 2019.

[88] K. Y. Tu, M. S. Rasras and D. M. Gill, "Silicon RF-Photonic Filter and Down-Converter," *IEEE Journal of Lightwave Technology,* vol. 28, no. 20, pp. 3019-3028, 2010.

[89] S. Jin, L. Xu and V. Rosborough, "RF Frequency Mixer Photonic Integrated Circuit," *IEEE Photonics Technology Letters,* vol. 28, no. 16, pp. 1771-1773, 2016.

[90] C. G. Bottenfield, V. A. Thomas, G. Saha, R. DeSalvo and S. E. Ralph, "A silicon microwave photonic down-converter," in *ECOC,* Dublin, Ireland, 2019.

[91] C. G. Bottenfield, M. Hoff, V. A. Thomas, A. Winoto, Y. Zhou, A. Bhardwaj, G. E. Hoefler, R. DeSalvo and S. E. Ralph, "High Performance Microwave Photonic Downconversion in a Commercial InP Platform," in *OFC,* USA, 2021.

[92] "Silicon Photonics Process Design Kit (APSUNY PDK v3.0," AIM Photonics, [Online]. Available: http://www.aimphotonics.com/pdk/. [Accessed 20 October 2019].

[93] K. Giewont, K. Nummy, F. A. Anderson, J. Ayala, T. Barwicz, Y. Bian, K. K. Dezfulian, D. M. Gill, T. Houghton, S. Hu, B. Peng, M. Rakowsky, S. Rauch, J. C. Rosenberg, A. Sahin, I. Stobert and A. Stricker, "300-mm Monolithic Silicon Photonics Foundry Technology," *Journal of Selected Topics in Quantum Electronics,* vol. 25, no. 5, pp. 1-11, 2019.

[94] A. M. Gutierrez, A. Brimont and J. Herrera, "Silicon slow-light-based photonic mixer for microwave-frequency conversion applications," *Optics Letters,* vol. 37, pp. 1721-1723, 2012.

[95] M. Rakowski, C. Meagher, K. Nummy and etal, "45nm CMOS - Silicon Photonics Monolithic Technology (45CLO) for next-generation, low power and high speed optical interconnects," in *OFC,* San Diego, USA, 2020.